Scuola di dottorato
Università degli studi di Milano-Bicocca

Department of Physics G. Occhialini
PhD program in Physics and Astronomy XXXVIII cycle

Development of Time, Energy, and Spatially Resolved Compact Diagnostics for Tokamak Radiation Studies

Agostino Celora
Matriculation number 827567

Tutor: Prof. **Marco Tardocchi**
Supervisor: Prof. **Gabriele Croci**

Coordinator: Prof. **Laura D'Alfonso**

Academic year 2025/2026

"Everything that humans can imagine is a possibility in reality."

Willie Gallon

Contents

Abstract

Tokamak devices exploit strong magnetic fields to confine high-temperature plasmas and achieve controlled thermonuclear fusion, aiming for sustainable energy production. During operation, the plasma emits a broad spectrum of electromagnetic and particle radiation, which provides crucial information on its behavior and key parameters.
This PhD thesis focuses on the development and exploitation of radiation diagnostics for the study of neutron and Soft X-Ray (SXR) emission in tokamak plasmas. Two systems are investigated: a Gas Electron Multiplier (GEM)-based SXR camera implemented and operated on the MAST-U tokamak, and a Single crystal Diamond Detector (SDD)-based neutron camera designed for the SPARC tokamak. These diagnostics measure plasma radiation with time, energy, and spatial resolution, supporting detailed analysis of plasma behavior and parameters.
To support their design and exploitation, Revolt, a geometric Monte Carlo radiation-transport code, has been developed and upgraded during this work. The current version, Revolt-U, includes energy-resolved SXR analysis, allowing the modelling of radiation transport from the plasma to the detectors and supporting both diagnostic design choices and spatial analysis.
The first part of the thesis addresses the optimization of the SPARC Neutron Camera (NCAM) for ion temperature profile reconstruction across the wide neutron-flux range expected during deuterium-tritium operation. The study evaluates the optimal number and size of diamond detector pixels at the line-of-sight (LOS) endpoints, targeting robust inter-shot analysis. Synthetic neutron data from the SPARC reference plasma scenario are generated, heuristically perturbed, and processed using a dedicated inversion algorithm to evaluate the performance of various NCAM configurations.
The second part of the thesis focuses on the GEM-based SXR diagnostic operated on MAST-U. GEM detectors offer robustness in harsh fusion environments and the capability to deliver coarse energy-resolved SXR imaging with centimeter-scale spatial resolution and sub-millisecond temporal resolution. The system installed on MAST-U demonstrates the ability to complement existing SXR camera arrays by adding a spectral dimension to spatially and temporally resolved measurements. These results highlight the potential of GEM-based diagnostics for advancing the understanding of plasma dynamics, as well as the associated challenges posed by operation in intense neutron environments.

Riassunto

I tokamak sono macchine che utilizzano campi magnetici intensi per confinare plasmi ad alta temperatura per il raggiungimento della fusione termonucleare controllata, con lo scopo finale di produrre energia in modo sostenibile e sicuro. Durante il loro funzionamento, il plasma emette un ampio spettro di radiazione elettromagnetica e di particelle, che fornisce informazioni cruciali sul comportamento del plasma e sui suoi parametri chiave.

Questa tesi di dottorato si concentra sullo sviluppo e utilizzo di diagnostiche per lo studio delle emissioni di neutroni e di raggi X soffici (Soft X-Ray, SXR) nei plasmi fusionistici. Due diagnostiche sono state studiate in questa tesi: un rivelatore per SXR basato sulla tecnologia Gas Electron Multiplier (GEM) utilizzata sul tokamak MAST-U, e una camera per neutroni basata su rivelatore a diamante monocristallino (Single-Crystal Diamond Detector, SDD) progettata per il tokamak SPARC. Queste diagnostiche permettono di combinare misure spettrali, spaziali e temporali della radiazione, consentendo uno studio dei parametri del plasma e del suo comportamento.

Per supportarne la progettazione e l'utilizzo, è stato sviluppato e aggiornato nel corso di questo lavoro Revolt: un codice Monte Carlo per il trasporto della radiazione basato sulla modellizzazione geometrica. La versione aggiornata, Revolt-U, introduce funzionalità dedicate agli studi SXR risolti in energia, permettendo la modellizzazione del trasporto della radiazione dal plasma ai rivelatori e supportando sia le scelte progettuali delle diagnostiche sia l'analisi spaziale.

La prima parte della tesi riguarda l'ottimizzazione della Neutron Camera (NCAM) del tokamak SPARC, per la ricostruzione del profilo di temperatura degli ioni su un ampio intervallo di flussi di neutroni previsto durante le operazioni in deuterio-trizio. Lo studio valuta il numero e le dimensioni ottimali dei pixel del rivelatore a diamante agli estremi delle linee di vista (LOS) della camera. Sono stati generati dati sintetici di neutroni a partire dallo scenario di plasma di riferimento perturbato in modo euristico, I dati sono poi stati processati mediante un algoritmo di inversione dedicato, per valutare le prestazioni delle diverse configurazioni della NCAM.

La seconda parte della tesi si concentra sulla diagnostica SXR basata su GEM operativa su MAST-U. I rivelatori GEM offrono resistenza alla radiazione in ambienti di fusione estremi e la capacità di fornire immagini SXR risolte in energia con risoluzione spaziale su scala centimetrica e risoluzione temporale sub-millisecondo. Il sistema installato su MAST-U dimostra la capacità di integrare le camere SXR esistenti aggiungendo

la dimensione spettrale alle misure già risolte spazialmente e temporalmente. I risultati evidenziano il potenziale della diagnostica GEM per migliorare la comprensione della dinamica del plasma, nonché le sfide associate al suo funzionamento in ambienti con intensa radiazione neutronica.

Chapter 1

Fusion energy and tokamak devices

The global demand for energy continues to rise, driven by population growth, the rapid industrialization of developing countries, and the rising of new energy-intensive technologies posing significant challenges to the energy production system, which currently relies largely on fossil fuels. The Intergovernmental Panel on Climate Change (IPCC) [1] identifies the combustion of fossil fuels as the primary cause of global warming due to the emission of greenhouse gases. Therefore, a rapid reduction in greenhouse gas emissions, aiming for net-zero by mid-century, is crucial to mitigate the impact of the climate crisis. Renewable energy sources such as solar, wind, and hydroelectric power are essential for transitioning to low-emitting energy production. However, their inherent intermittency limits their ability to provide continuous base-load power, and large-scale, cost-effective energy storage technologies remain technologically and economically constrained. Nuclear fission offers high energy density and low carbon emissions but remains constrained by issues of safety, radioactive waste management, proliferation risk and public acceptance.

Nuclear fusion, the process powering stellar energy production, represents a promising alternative for base-load power generation. Fusion of light isotopes such as deuterium and tritium releases energy without producing long-lived radioactive waste or greenhouse gases. Although significant technological challenges persist, advances in plasma confinement physics, materials science, and reactor engineering have brought the realization of controlled fusion energy powerplants increasingly within reach. This offers a reliable, scalable, and sustainable energy source for the future.

1.1 Nuclear fusion principles

Energy generation through nuclear processes, both fusion or fission, is tied to the concept of binding energy, a measure of the energy required to hold a nucleus together, operatively defined as the the mass difference between a nucleus and the sum of its constituent nucleons. This difference, known as the mass defect, is a direct consequence of Einstein's equation $E = mc^2$. In nuclear reactions, energy is released if the total binding energy

of the products is greater than that of the reactants, as the excess binding energy is converted into kinetic energy or radiation. Binding energy per nucleon, which represents the average energy binding each nucleon within a nucleus, provides crucial insights into the stability of atomic nuclei. Experimentally deduced data for the binding energy per nucleon as a function of atomic mass number reveal a distinct trend, as shown in Figure 1.1. The curve peaks at atomic mass numbers of 60, corresponding to iron and nickel, which are the most tightly bound elements. This peak indicates that energy can be released by either combining lighter nuclei (fusion) or splitting heavier ones (fission). This work is a small contribution to the goal of successfully exploiting nuclear fusion for energy generation.

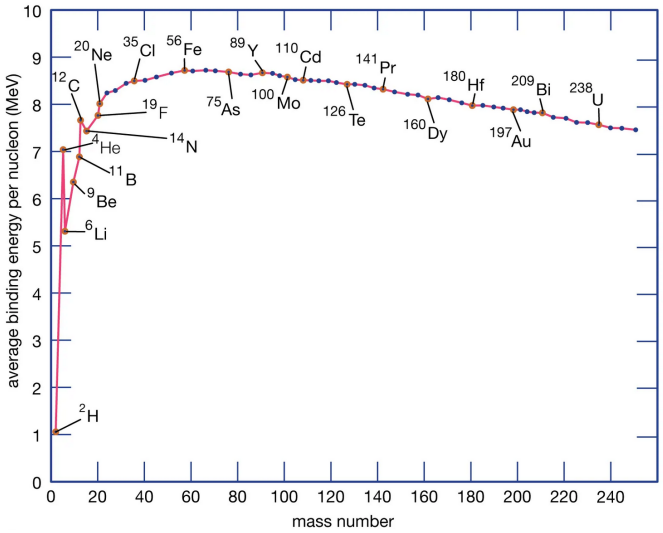

Figure 1.1: Nuclear binding energies, shown as a function of atomic mass number [2].

The driving force behind fusion is the strong nuclear force. This force acts over very short ranges, attracting nucleons (protons and neutrons) to each other with a dependence on distance approximately proportional to $F_s \propto 1/r^3$. Nonetheless, achieving fusion is not straightforward due to the repulsive Coulomb force between the positively charged nuclei, which acts over longer ranges with a dependence proportional to $F_C \propto 1/r^2$. To overcome this Coulomb barrier, nuclei must collide with sufficient energy to bring them within the range of the strong nuclear force.

The classical physics requirement for overcoming the Coulomb barrier is typically achieved through high thermal energies, on the order of several hundred keV [3]. However, at the scale of nuclear interactions, quantum mechanics plays a pivotal role in lowering the energy threshold for fusion reactions. The most important mechanism is quantum tunneling, which allows nuclei to penetrate the Coulomb barrier despite having insufficient kinetic energy, a phenomenon forbidden in classical physics. In addition to tunneling, nuclear resonance effects further enhance fusion probabilities at specific energies. These

resonances occur when the colliding nuclei form an intermediate compound nucleus with an energy state corresponding to that of the interacting system, increasing the likelihood of fusion.
The combination of the quantum phenomena shifts the peak of the fusion interaction cross section to lower energies, as illustrated in the following cross-section plot for the most relevant fusion reactions:

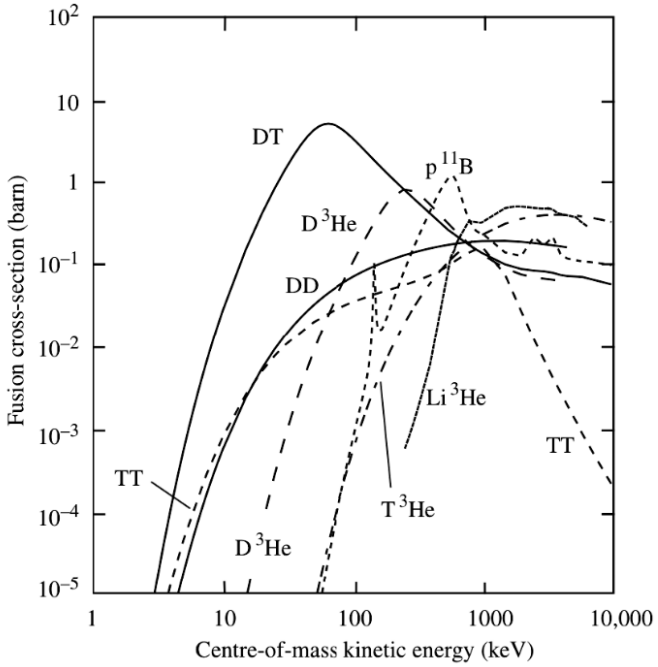

Figure 1.2: Experimental cross sections for the most relevant fusion reactions. [4]

Among the various fusion reactions, those involving isotopes of hydrogen: Deuterium (${}^2_1D$), Tritium (${}^3_1T$) and Helium-3 (${}^3_2He$) are of primary interest due to their relatively high reaction cross-sections and significant energy outputs. The most relevant fusion reactions are:

$$\mathrm{D} + \mathrm{T} \rightarrow {}^4\mathrm{He}\,(3.5\,\mathrm{Mev}) + \mathrm{n}(14.1\,\mathrm{MeV}) \tag{1.1}$$

$$\mathrm{D} + \mathrm{D} \rightarrow {}^3\mathrm{He}\,(0.82\,\mathrm{MeV}) + \mathrm{n}(2.45\,\mathrm{MeV}) \tag{1.2}$$

$$\mathrm{D} + {}^3\mathrm{He} \rightarrow {}^4\mathrm{He}\,(3.6\,\mathrm{MeV})^{+}\,\mathrm{p}(14.7\,\mathrm{MeV}) \tag{1.3}$$

While Deuterium is abundant in nature, comprising approximately 0.015% [5] of natural water, Tritium must be continuously artificially produced, because of its half-life of 12.3 year. This can be achieved by the interaction of Lithium-7, abundant in nature, with neutrons generated in the D-T reaction, hence the possibility of self-sustained Tritium cycles in future fusion power plans. On the other hand, the scarcity of Helium-3 on Earth makes D−^{3}He reactions less feasible for near-term applications. Among these reactions, the D−T reaction emerges as the most practical choice for current fusion research and

development. Its superior reaction cross-section at the relatively low energy of tens of keV, and significant energy yield, coupled with relatively manageable fuel requirements, make it the primary focus of most experimental fusion projects. While the D + ^{3}He reaction produces slightly more energy, its low cross-section and limited fuel availability constrain its use. Future advancements, however, may shift the focus to alternative reactions such as D–^{3}He or even D–D, as technology progresses. It is paramount to mention that the vast majority of fusion experiments in the past and nowadays have been based on Deuterium only fuels, given the current limited availability, and handling complexity of Tritium.

1.2 Plasma for fusion machines

At the high temperatures required for fusion, matter transitions into the plasma state, an ionized gas that remains electrically neutral overall but exhibits complex collective behaviors.

Without confinement, the high-energy particles in the plasma would quickly escape and dissipate. A crucial aspect of plasma physics is the fact that solid confinement is not feasible at fusion temperatures, which far exceed the limits of any known material's thermal tolerance. Plasma confinement can be achieved through various methods. One approach is inertial confinement, where intense lasers or ion beams compress the fuel to extreme densities for a brief moment, creating the conditions needed for fusion [6]. The second approach, and the most extensively investigated strategy for achieving sustained fusion, is magnetic confinement, which constitutes the focus of this work. The basic principle of magnetic confinement relies on the Lorentz force acting on charged particles in a magnetic field. This force keeps the particles on spiral trajectories along the magnetic field lines, effectively confining them in directions orthogonal to the field. The Lorentz force is given by:

$$\vec{F} = q(\vec{E} + \vec{v} \times \vec{B}) \tag{1.4}$$

Here, $\vec{F}$ is the force on a particle with charge q, $\vec{E}$ is the electric field, B is the magnetic field, and $\vec{v}$ is the particle velocity. The cross product $\vec{v} \times \vec{B}$ indicates that the force is always perpendicular to both the particle velocity and the magnetic field, causing a circular motion in the plane orthogonal to $\vec{B}$. Since particles are confined in the direction orthogonal to the magnetic field but not in the parallel direction, a suitable geometry for magnetic confinement ensures that field lines form closed loops within the machine, without colliding the particles to the walls. The simplest and most practical geometry to achieve this is a toroidal magnetic field, where the field lines are wrapped in a donut-like structure, as used in experimental devices such as tokamaks and stellarators.

As a first approximation, the plasma is confined within a toroidal chamber by external magnetic coils that generate a strong toroidal magnetic field. However, a more detailed analysis shows that such a configuration is not sufficient to ensure stable confinement. The toroidal geometry introduces two important effects: (i) the curvature of the magnetic field lines and (ii) the radial gradient of the magnetic field strength, which is higher on the inner side of the torus and lower on the outer side. These effects give rise to curvature

and ∇B drifts that act in opposite directions for ions and electrons, leading to charge separation. The resulting electric field then induces an $\mathrm{E} \times \mathrm{B}$ drift, which is directed radially outward and can compromise plasma confinement.

1.3 Tokamak

A solution to mitigate these effects is the Tokamak concept. In a tokamak, a strong toroidal current is induced in the plasma. By Ampere's law, this current generates a poloidal magnetic field (a field that wraps around the minor circumference of the torus). The combination of the toroidal and poloidal fields results in helicoidal magnetic field lines that continuously move the particles between the inner and outer sides of the torus, subjecting them alternately to centrifugal and centripetal forces. This alternating motion stabilizes the orbits and improves confinement [7].
The toroidal plasma current is induced through transformer action. A poloidal field coil located in the central solenoid of the tokamak acts as the primary circuit, while the plasma behaves as the secondary circuit. A time-varying current in the primary produces a loop voltage that drives the plasma current, which can be maintained approximately constant for as long as the primary current ramp is sustained. Because the available transformer flux swing is finite, the current drive cannot be continuous, and tokamaks therefore operate in pulsed regimes rather than steady state. A schematic of this configuration is shown in figure 1.3.

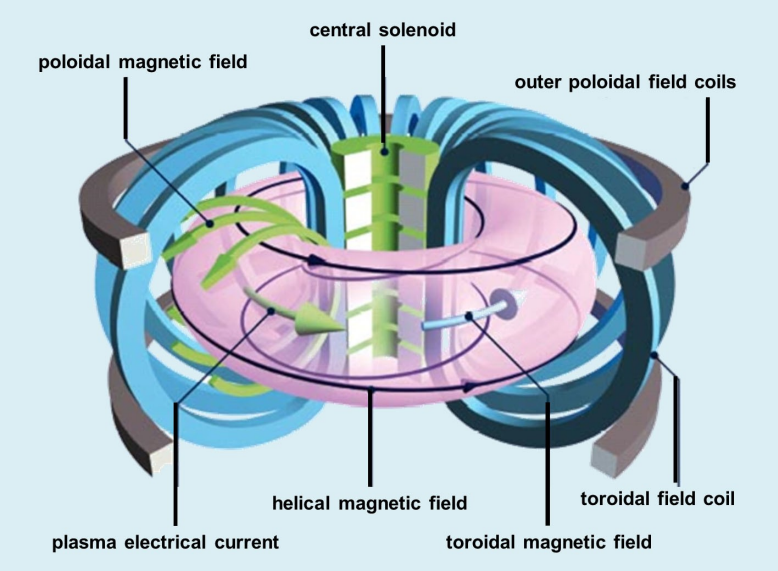

Figure 1.3: Schematic of the main components of a tokamak [8].

The plasma is confined within a toroidal vacuum vessel. The hot core plasma remains well separated from the vessel walls by closed magnetic flux surfaces. Outside the last closed magnetic surface lies the scrape-off layer (SOL), where magnetic field lines intersect

the plasma-facing components (PFCs), allowing particles and heat to flow continuously toward the divertor targets. Particles are considered lost from the confined plasma once they cross the last closed magnetic surface due to collisional transport and drifts, after which they stream along open field lines to the PFCs.
Two of the major challenges that affect the efficiency and integrity of the reactor are:

1. Impurities, introduced by plasma-wall interaction that lead to the erosion of plasma-facing materials. Following this, sputtered atoms can accumulate in the plasma core, radiating energy and potentially causing a sudden disruption of confinement, which may damage the reactor.

2. Magneto-hydro-dynamic (MHD) instabilities, which can disrupt the plasma confinement.

1.3.1 Magnetic confinement: equilibrium and instabilities

In a tokamak, the balance between the outward plasma pressure and the inward magnetic pressure is crucial for confinement. The plasma pressure can be expressed using the ideal gas law:

$$p = nk_BT \tag{1.5}$$

where n is the particle density (in particles/m^3), T is the plasma temperature (in keV) and k_B is the Boltzmann's constant. The magnetic pressure p_B is given by:

$$p_B = \frac{B^2}{2\mu_0} \tag{1.6}$$

where B is the magnetic field strength (in Tesla) and $\mu_0 = 4\pi \times 10^{-7}$H/m is the permeability in vacuum. The plasma beta β is defined as the ratio of plasma pressure to magnetic pressure and is a parameter frequently used to define the efficiency of a magnetic field to confine a plasma:

$$\beta = \frac{p}{p_B} = \frac{2\mu_0 nT}{B^2} \tag{1.7}$$

In fusion research, maximizing β is critical because a higher plasma pressure for a given magnetic field strength improves reactor efficiency. While a high β is desirable, it is limited by magnetohydrodynamic (MHD) instabilities. These instabilities can disrupt the plasma if β exceeds a critical value, known as the beta limit. The beta limit depends on the configuration of the magnetic field and the plasma geometry. For tokamaks, the empirical normalized beta β_N is often written as:

$$\beta_N = \frac{\beta}{I/aB} \tag{1.8}$$

where I is the plasma current (in MA), a is the torus minor radius (in m), B is the magnetic field (in T). In practice β_N must remain below a critical threshold to avoid MHD instabilities such as ballooning modes or kink modes. If β_N exceeds this limit, MHD

instabilities can lead to a loss of confinement, reducing performance or even disrupting the plasma.

1.3.2 Plasma heating mechanisms

Achieving temperatures of about 10^8 K ~ 10keV is essential for sustaining fusion reactions in a tokamak. Plasma heating is a multi-stage process: it begins with ohmic heating, which is then followed by auxiliary methods such as neutral beam injection (NBI) and radio-frequency (RF) heating, ultimately leading to the plasma becoming largely self-heated: the burning plasma regime.
Ohmic heating relies on the plasma current and is effective at low temperatures. However, two limitations restrict the use of ohmic heating. The first is the behavior of the plasma resistivity, which decreases as the plasma temperature rises, thus reducing the heating power. The second is that excessive plasma current triggers instabilities, which can disrupts the plasma. Since ohmic heating becomes ineffective at high temperatures, auxiliary heating methods must be introduced.
The basic principle of NBI is accelerating external ions to high energies and then neutralizing them so they can penetrate the plasma's magnetic field. Once inside the plasma, these neutral particles are ionized through collisions with plasma particles. The newly created fast ions transfer their energy to the bulk plasma through subsequent collisions, thereby raising the plasma temperature.
Radio-frequency wave heating consists in injecting electromagnetic waves into the plasma at carefully chosen frequencies that resonate with the plasma ions and/or electrons. By matching the wave frequency with a natural frequency of the plasma particles, energy can be transferred effectively, leading to significant heating.
These auxiliary heating techniques play a vital role in bridging the gap between the initial ohmic heating phase and the conditions required for the burning plasma.

Burning plasma regime

A burning plasma is a state in which most of the plasma heating is generated internally by the fusion reactions themselves, rather than relying on external heating sources. This regime has not yet been achieved and represents a critical milestone in the quest for controlled nuclear fusion. In the DT reaction (Equation 1.1), the neutron carries most of the released energy (14.1 MeV) and escapes the magnetically confined plasma, while the α-particle remains confined by the magnetic field. The α-particles transfer their kinetic energy to the plasma through Coulomb collisions, thereby heating the bulk ions and electrons. The escaping neutrons, instead, deposit their energy in the surrounding blanket through thermalization processes, where the generated heat can be extracted to produce electricity. The ignition condition is reached when the α-particle heating power P_α balances the total energy losses, such that external heating can, in principle, be switched off.

The figure of merit used to quantify the fusion power compared to the external heating power applied is the energy gain factor Q, defined as the ratio between the fusion power produced (P_{fusion}) and the external heating power (P_{heating}):

$$Q = \frac{P_{\text{fusion}}}{P_{\text{heating}}} \tag{1.9}$$

In the pure burning plasma regime the power provided by fusion α-particles is sufficient to replace external heating sources, resulting in $Q \to \infty$. However, practical fusion reactors aim for a balance: a sufficiently high Q (e.g. $Q \geq 50$) without necessarily reaching full ignition. This balance ensures stable, continuous operation while minimizing the complexity of full self-sustaining plasma. In fusion research, the condition $Q = 1$ is referred to as scientific breakeven, corresponding to the point where the fusion power equals the external heating power.
The current record for highest Q in a tokamak (as recorded during actual D-T fusion) was set by JET at $Q = 0.67$ in 1997, producing 16 MW of fusion power while injecting 24 MW of thermal power to heat the fuel. [9].
Several ongoing projects aim to achieve and surpass breakeven, paving the way toward practical fusion energy. ITER (International Thermonuclear Experimental Reactor) is expected to reach $Q = 10$ with first plasma in the 2030s and deuterium-tritium operations in the late 2030s [10]. BEST, a chinese experiment focused on exploring burning plasma physics and achieve advanced steady-state plasma performance, plans to achieve breakeven and beyond in the late 2020s [11]. SPARC: a compact, high-field tokamak under development by the Commonwealth Fusion Systems (CFS), aims to demonstrate $Q > 2$ and beyond by the late 2020s [12].
The power produced by a tokamak depends on several machine parameters, notably the main parameters are the major radius R and the magnetic field B at the plasma center. In fact fusion power output $\mathrm{P_{FUS}}$ can be expressed as proportional to these quantities [13]:

$$P_{FUS} \propto \beta_N^2 R^3 B^4 \tag{1.10}$$

Figure 1.4 shows the Fusion Energy Gain for the most relevant tokamaks, organized as their R, B parameters.

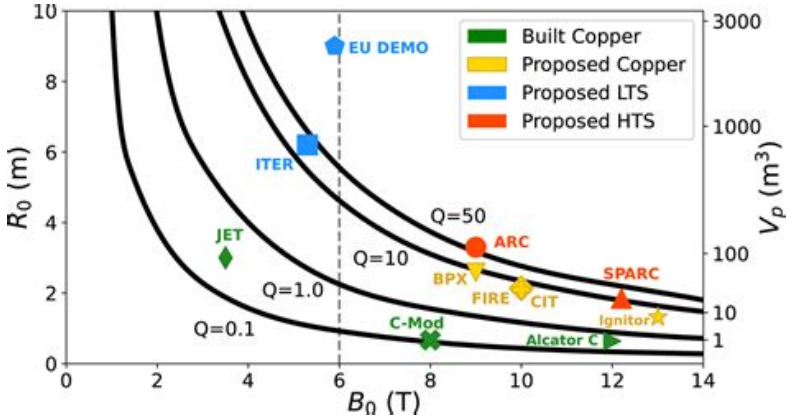

Figure 1.4: Plot of the dependence of Fusion Energy Gain (Q) on Major Radius (R_0) and on-axis Magnetic field (B_0). With examples of few major tokamak machines. From [14].

This plot highlights the two important strategies for improving fusion performance. The first approach is increasing the tokamak size allows for more plasma volume, which enhances the fusion reaction rate. This is the approach of ITER, which has a large major radius of $R \sim 6.2$m. The second approach is focusing on higher magnetic field: a stronger magnetic field improves plasma confinement and allows for a more compact design. This is the approach of SPARC, which aims to achieve high fusion performance with a compact, high-field tokamak ($R \sim 1.85$m). Both approaches have trade-offs: ITER prioritizes stability and scalability for a large-scale reactor, while SPARC focuses on leveraging modern High-Temperature Superconductors (HTS [15]) to achieve higher magnetic fields and smaller device size.

1.4 SPARC

SPARC is a compact, high-field tokamak currently under development by Commonwealth Fusion Systems (CFS). Its design represents a significant departure from traditional tokamaks like ITER by adopting a smaller device with stronger magnetic fields to achieve high fusion performance. Specifically, SPARC aims to demonstrate $Q > 2$ and beyond through the use of advanced HTS magnets based on rare-earth barium copper oxide (REBCO) superconductors.
These HTS magnets enable much higher magnetic fields compared to conventional low-temperature superconductors (such as niobium-tin used in ITER). This innovative approach has been made possible by advances in materials science and engineering. In contrast to ITER's large size and long construction timeline, SPARC adopts a faster, more agile development approach, aiming for first plasma by 2026 and fusion experiments soon after. The key parameters of SPARC are grouped in Table 1.1 and Figure 1.5 illustrates the SPARC section schematic.

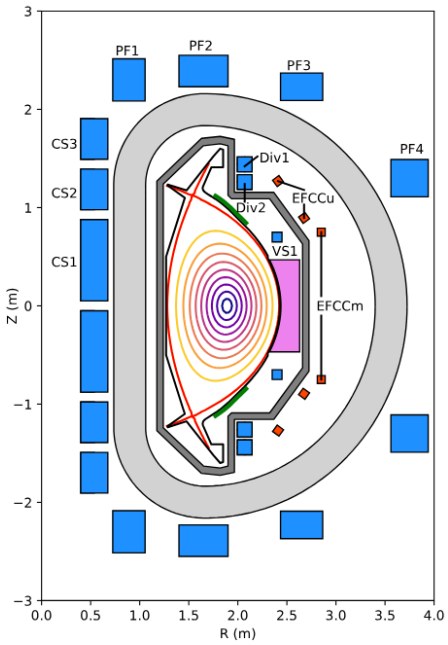

Figure 1.5: SPARC V2 poloidal cross-section. The toroidal field coil is light grey. The central solenoid and poloidal field coils are blue. Error-field correction coils are orange-red. The vacuum vessel is dark grey. The ICRH antenna is pink. The divertor and first limiting surfaces are black. Vertical stability plates are green. The plasma separatrix is red. From [14].

Table 1.1: Main Parameters of SPARC Tokamak. From [14]

Parameter	**Value**
Major Radius R (m)	1.85
Minor Radius a (m)	0.57
Plasma Current I_p (MA)	8.7
Magnetic Field on Axis B_0 (T)	12.2
Elongation κ	1.97
Triangularity δ	0.54
Plasma Volume V_p (m^3)	22.7
Fusion Power P_{fusion} (MW)	140
External Heating Power $P_{heating}$ (MW)	25
Max. Fusion Gain Q	11
Energy Confinement Time τ_E (s)	0.3
Ion Temperature T_i (keV)	14-20
Density n (10^{20} m^{-3})	2-3

1.5 MAST-U

MAST-Upgrade (Mega Amp Spherical Tokamak Upgrade) is a compact tokamak developed at the Culham Centre for Fusion Energy (CCFE) in the UK. The device adopts the spherical tokamak (ST) approach, characterized by a low aspect ratio, which provides several advantages in terms of plasma stability, confinement, and cost-effectiveness. Spherical tokamaks like MAST-Upgrade aim to achieve high plasma β values, crucial for increasing the efficiency of confinement and improving overall reactor performance [16]. MAST-Upgrade was designed to investigate the physics and engineering challenges of compact tokamaks while contributing to key areas such as plasma exhaust, stability, and confinement. A key challenge addressed by MAST-U is heat exhaust, which is critical for future fusion reactors. To address this issue, the device includes a Super-X divertor system [17], a novel solution designed to reduce thermal loads on plasma-facing components.
Figure 1.6 shows the poloidal cross-section of MAST-U, while Table 1.2 summarizes the key tokamak parameters. These parameters are essential for understanding the design and capabilities of MAST-Upgrade, a compact spherical tokamak that represents an important step forward in fusion research.

Parameter	**Value**
Major Radius (R)	0.85 m
Minor Radius (a)	0.65 m
Aspect Ratio ($A = R/a$)	1.3
Toroidal Magnetic Field (B_T)	0.8 T
Plasma Current (I_p)	Up to 2 MA
Pulse Duration	Typical 1-2 s
Heating Power	3.8 MW (NBI)
Electron Temperature (T_e)	Up to 2 keV
Normalised Beta (β_N)	3 to 6

Table 1.2: Main parameters of MAST-Upgrade. [18]

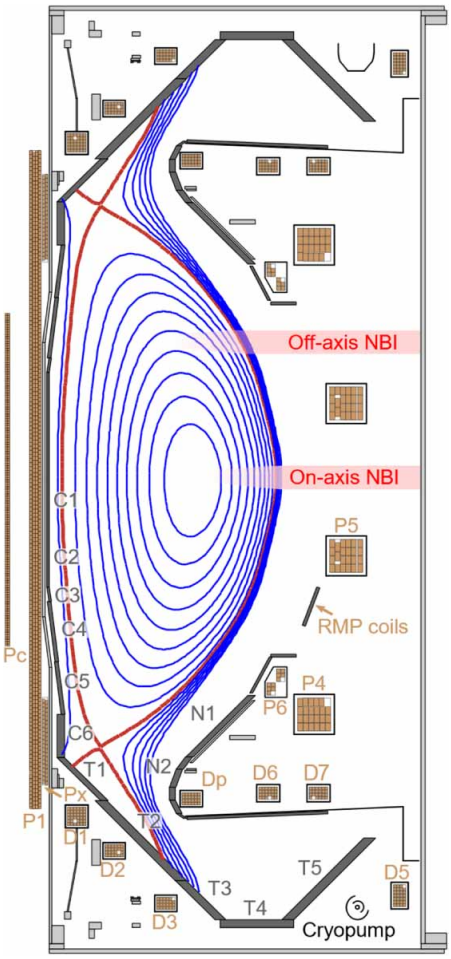

Figure 1.6: Poloidal cross-section of MAST upgrade. [18]

1.6 Radiation in Tokamak Plasmas

Plasma radiation in tokamaks has both detrimental and beneficial aspects. While it dissipates energy, its emission patterns also provide valuable information about plasma behavior, aiding our understanding of the confinement device. In addition real-time diagnostics can be used for controlling operations and maintaining stable performance, underscoring their importance in advancing fusion research. The principal types of plasma emissions include:

- **Electromagnetic radiation** across a wide spectrum:
  - Radio-frequency (RF) and microwave emission (electron cyclotron radiation, synchrotron emission)
  - Visible and ultraviolet light (line radiation from impurities, bremsstrahlung continuum)

  - Soft X-rays (SXR, ~1–20 keV) typically associated with thermal radiation from the hot plasma core, and Hard X-rays (HXR, at higgher energies), predominantly produced by non-thermal processes
  - Gamma rays, from nuclear reactions, neutron interactions with surrounding materials, and bremsstrahlung of runaway electrons

- **Neutrons**, mostly produced by fusion reactions (D-D or D-T)
- **Charged particles** escaping confinement (e.g., fast ions, alpha particles)

The scope of this thesis is the development of diagnostics for two types of plasma emission: neutrons and Soft X-rays (SXR). The latter refers to X-ray radiation in the energy range of approximately 1–20 keV.

1.7 Soft X-Ray Emission in Tokamaks

Fusion plasmas emit SXR mainly through three processes: free-free interactions (Bremsstrahlung radiation), free-bound interactions (radiative recombination), and bound-bound interactions (line radiation). These emissions are highly valuable for plasma diagnostics, since their intensity and spectral distribution strongly depend on the electron temperature, density, and impurity content.

Bremsstrahlung

In tokamak plasmas, Bremsstrahlung originates from the acceleration of free electrons during collisions with ions. Its spectral range is very broad, extending from the microwave to the SXR region, thereby offering several diagnostic possibilities. The Bremsstrahlung energy spectrum shows a strong exponential dependence on the electron temperature T_e, as well as a quadratic dependence on the electron density n_e^2, and on the impurity concentration, typically described by the effective ion charge:

$$Z_{eff} = \frac{\sum_i n_i Z_i^2}{\sum_i n_e}.$$

The local emissivity is given by [19]:

$$\epsilon_{Brem}(E, \bar{x}, t) \propto E \cdot n_e(\bar{x}, t)^2 \cdot Z_{eff} \cdot T_e(\bar{x}, t)^{-1/2} \exp\left[\frac{-E}{k_B T_e(\bar{x}, t)}\right] \tag{1.11}$$

Most of the Bremsstrahlung power is radiated by photons with energies comparable to the electron temperature, $hc/\lambda \sim T_e$. For hot plasmas, this typically falls in the SXR region, making this spectral window particularly suitable for rapid, time-resolved measurements of plasma parameters and position.

Radiative recombination

Radiative recombination occurs when a free electron is captured by an ion, corresponding to a free-bound interaction. The resulting photon emission has a semi-continuous spectrum:

$$h\nu = E_{kin} + \Delta E_{\infty j}^{(z)}, \tag{1.12}$$

where E_{kin} is the initial kinetic energy of the free electron and $\Delta E_{\infty j}^{(z)}$ is the difference between the ionization threshold and the bound energy level j of the captured electron. Since the photon energy is the sum of a continuous term (E_{kin}) and a discrete term ($\Delta E_{\infty j}^{(z)}$), the spectrum shows both continuous and edge-like features. The relative contribution of recombination becomes progressively weaker compared to Bremsstrahlung as the electron temperature increases.

Line emission

Line emission arises from radiative transitions of bound electrons between discrete atomic levels. In tokamak plasmas, excited states are primarily populated by collisions with free electrons. Since hydrogenic fuel ions are fully ionized in the hot core, line emission in this region mainly originates from medium and high-Z impurities. For this reason, line radiation is a key diagnostic tool for studying impurity behavior. The emitted spectrum consists of discrete lines associated with transitions between upper (j) and lower (i) levels:

$$h\nu_{ji} = E(j) - E(i). \tag{1.13}$$

1.7.1 State of the Art in Soft X-Ray Diagnostics

Soft X-ray (SXR) diagnostics are powerful tools for studying high-temperature plasmas, offering insights into their spatial and temporal behavior. The emission originates primarily from bremsstrahlung and line radiation processes, which are sensitive to local plasma parameters like temperature, density, and impurity content. However, determining absolute plasma parameters directly from measured SXR intensities is challenging due to the non-linear relationship between emissivity and these quantities.
In tokamaks, the optically thin nature of the plasma in the SXR range enables the reconstruction of two-dimensional emissivity maps. This is achieved through a measurement system consisting of collimated detectors observing the plasma along distinct lines of sight (Figure 1.7) and applying inversion techniques to retrieve spatial emission profiles and the estimation of local plasma parameters. Since parallel transport greatly exceeds cross-field transport in most magnetic-confinement regimes, plasma state variables such as electron temperature and density can, to a good approximation, be considered invariant over individual magnetic flux surfaces. Consequently, emissivity patterns align with the magnetic topology, providing valuable insights into plasma equilibrium, impurity transport, and magneto-hydrodynamic instability evolution through SXR tomography [20].

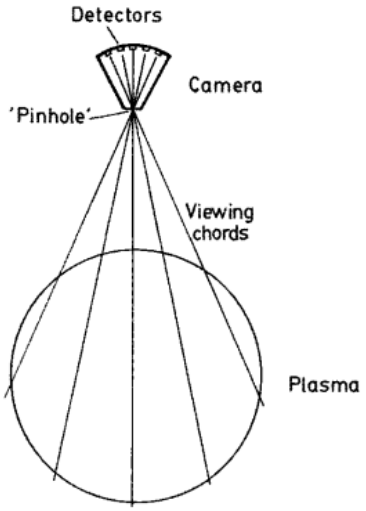

Figure 1.7: Schematic illustration of a pinhole camera system used for soft X-ray imaging. From [20].

Traditional SXR diagnostics on tokamaks employ solid-state semiconductor photo-diodes, which measure the energy deposited in the detector by incident photons above a given threshold. The collected charge is proportional to the energy deposited, enabling reliable time-resolved measurements of plasma emission. To obtain information on the energy distribution of the emitted SXR, foil filters of different thicknesses (typically beryllium) are placed in front of the detectors. The thickness determines the energy cutoff of transmitted SXR photons, making the system sensitive to different energy ranges.
Photo-diodes have a major limitation: they are prone to radiation damage under intense neutron fluxes, a concern exacerbated in next-generation devices with significantly higher neutron output. This has stimulated the search for new alternatives, including scintillator-based detectors [21], diamond detectors [22] and Gas Electron Multiplier (GEM) detectors [23] [24] [25], the focus of this thesis. A brief overviews of photo-diodes, scintillator-based and diamond detectors are provided here, while an in-depth overview of GEM detectors is presented in the next chapter.

Semiconductor photo-diode detectors

Semiconductor photo-diodes (typically based on silicon p-n junctions) are the most widely used SXR detectors in tokamaks. When a photon with energy above the material band gap is absorbed, it generates an electron-hole pair. Under an applied voltage difference, these charge carriers drifts, producing a current pulse proportional to the deposited energy. Arrays of such diodes are compact, robust, and allow for high temporal resolution (down to sub-nanoseconds scale), which makes them ideally suited for SXR tomography and monitoring of fast plasma instabilities [20].

Scintillator-based detectors

Scintillator detectors operate by converting incident X-ray photons into visible light through scintillation processes in a crystal (such as CsI(Tl) or YAP:Ce). The light is then detected by a photomultiplier tube (PMT) or a photo-diode. These systems are attractive because the choice of scintillator material can be tuned to achieve high detection efficiency in a given energy range, and they can provide both spatial and spectral information. In addition, scintillator-based systems can withstand higher radiation environments than semiconductor diodes. However, their temporal resolution is typically limited by the scintillation decay time (tens to hundreds of nanoseconds) [21].

Diamond detectors

Diamond detectors exploit the unique electronic properties of synthetic single-crystal diamond, grown by chemical vapor deposition (CVD) [26]. Their structure typically follows a p-type/intrinsic/metal (PIM) configuration: a thin boron-doped layer forms the p-type contact, deposited on a high-purity intrinsic diamond substrate, which acts as the active region. A thin metallic layer (e.g., Pt or Al) completes the device. This geometry naturally establishes a built-in potential across the intrinsic region, so that incident photons can generate electron–hole pairs which are promptly collected without requiring an external bias. The signal is therefore proportional to the energy deposited by the incoming photons.
Diamond detectors present several advantages for tokamak applications. Due to their large bandgap ($\sim$ 5.5 eV), they exhibit extremely low leakage currents and are nearly insensitive to visible radiation, making them naturally selective for VUV and soft X-ray photons. They also feature very fast response times (up to $\sim$ 200 kHz) and exceptional radiation hardness compared with conventional silicon detectors, an essential requirement for operation in the extreme conditions of future fusion reactors. These properties make diamond detectors particularly well-suited for long-term, reliable operation in fusion environments, where conventional photodiodes often degrade. Their successful use has already been demonstrated in devices such as JET for soft X-ray and impurity monitoring [22].

1.8 Neutron emission in Tokamaks

The emission of neutrons in the current tokamak is produced by the fusion reactions, which in the present-day experiments are DT and DD reactions (Equation 1.1 and 1.2). The resulting neutrons carry respectively $\sim$ 14.1MeV and $\sim$ 2.5MeV, with the exact value determined by the reaction kinematics and the initial velocities of the reactants. Here follows an analysis of the neutron energy focused on the DT reaction, but the same analysis can be applied to the DD reaction. It is important to remark that in a DT plasma the cross-section of the DD reaction is not negligible, therefore 2.5 MeV neutrons will be ever-present in any DT plasma.

In the laboratory frame, the neutron energy E_n can be expressed in non-relativistic form as [20]:

$$E_n = \frac{m_\alpha}{m_n + m_\alpha}(Q + K) + \frac{1}{2}m_n V_{\mathrm{CM}}^2 + V_{\mathrm{CM}} \cos\theta \left[\frac{2m_n m_\alpha}{m_n + m_\alpha}(Q + K)\right]^{1/2}, \tag{1.14}$$

where m_n and m_α are the neutron and alpha masses, K is the relative kinetic energy of the reactants in the center-of-mass (CM) frame, Q the fusion reaction released energy, V_{CM} is the CM velocity, and θ is the angle between the emitted neutron and the CM velocity vector.

The CM velocity and relative kinetic energy are defined as:

$$V_{\mathrm{CM}} = \frac{m_d v_d + m_t v_t}{m_d + m_t}, \quad K = \frac{1}{2}\mu |v_d - v_t|^2, \tag{1.15}$$

with m_d, m_t, v_d, and v_t the masses and velocities of the deuteron and triton, and μ the reduced mass. The projection term $V_{\mathrm{CM}} \cos\theta$ leads to Doppler broadening of the neutron spectrum. For a thermalized plasma, the isotropic velocity distribution of the ions produces a Gaussian broadening proportional to $T_i^{1/2}$, where T_i is the ion temperature.

The average neutron energy may deviate from the nominal reaction value due to both thermal motion and plasma flows:

$$\Delta E_S = \langle E_n \rangle - E_0, \tag{1.16}$$

where $\langle E_n \rangle$ accounts for the ion velocity distribution and $E_0 = \langle E_n(T_i = 0) \rangle$ corresponds to the zero-temperature case. For example, at $T_i = 10$ keV, the shift is about $\Delta E_S \sim 35$ keV.

In addition, bulk plasma rotation introduces another shift in the mean neutron energy. For a toroidal rotation velocity V_r along the observation direction, the expected shift is:

$$\Delta E_V \approx 0.542\, V_r \ [\mathrm{keV}], \tag{1.17}$$

with V_r in km/s. Even modest flows of 1 km/s lead to a measurable displacement of about 0.54 keV, underlining the sensitivity required in neutron emission spectroscopy (NES).

The neutron emission spectrum, $S(E_n)$, directly reflects the velocity distributions of the reacting deuterium and tritium ions, $f_d(v)$ and $f_t(v)$. For Maxwellian distributions at ion temperature T_i, the spectrum takes the approximate Gaussian form:

$$S(E_n) \sim \exp\left[-\frac{(E_n - \langle E_n \rangle)^2}{2\Gamma_i^2}\right], \tag{1.18}$$

with a thermal width

$$\Gamma_i = \gamma(T_i)\, T_i^{1/2}, \tag{1.19}$$

where $\gamma(T_i)$ is a factor obtained from the reaction kinematics. Measuring both the centroid and the width of $S(E_n)$ enables the determination of T_i and of bulk plasma rotation V_r. Once T_i is known, the ion energy density $w_{d,t} = \frac{3}{2} n_{d,t} T_i$ can be derived, provided the deuterium and tritium densities $n_{d,t}$ are supplied by complementary diagnostics.

When the ion distribution is non-thermal or anisotropic, as in the presence of auxiliary heating methods such as neutral beam injection (NBI) or ion cyclotron resonance heating (ICRH), the neutron spectrum exhibits additional structures [27]. High-energy or epithermal components emerge, carrying the imprint of the fast-ion population and heating scheme.

Neutron emission spectroscopy is therefore a powerful tool to investigate both thermal and fast-ion behavior in tokamak plasmas. The analysis of Doppler broadening and spectral shifts allows extraction of fundamental parameters such as ion temperature, rotation velocity, and fast-ion distributions with high accuracy.

1.8.1 State of the Art in Neutron Diagnostics

Neutron measurements play a central role in fusion research due to their direct relation to fusion power and ability to provide insights into plasma behavior. The total neutron yield is proportional to fusion power, making it a key parameter for real-time monitoring of plasma performance. Neutrons also offer information on ion temperature, fuel ratio and velocity distribution, essential for assessing thermal and fast-ion populations.
Additionally, neutron diagnostics are crucial for reactor engineering, as they determine shielding and tritium-breeding blanket requirements. They can be integrated into feedback systems to support plasma control and stability optimization, and are indispensable for assessing radiation damage in candidate structural materials. Commonly employed techniques for neutron diagnostic include:

- **Neutron Flux Monitors:** Detect the overall neutron rate, providing a direct measure of fusion reactivity [28].
- **Activation Systems:** Materials placed in the neutron field become activated and emit gamma radiation, which can be analyzed to quantify neutron fluence [28].
- **Neutron Spectrometers:** Devices such as time-of-flight spectrometers [29], magnetic-proton-recoil spectrometers [30], scintillators [31], and diamond detectors [32] resolve the neutron energy spectrum, yielding detailed information on plasma conditions. A brief overview of the main neutron spectrometer diagnostics is presented below, while a more detailed analysis of diamond detectors is provided in the next chapter, as they constitute one of the central topics of this thesis.

Time-of-Flight Neutron Spectrometer (TOFOR)

The TOFOR (Time-of-Flight Optimized for Rate) neutron spectrometer is a detector developed specifically for use on tokamaks to measure the energy spectrum of fusion neutrons with high precision. Operating on the time-of-flight principle, the device detects neutrons produced in the plasma after they have traversed a known flight path. The arrival times are then converted into energy information. TOFOR employs two planes of plastic scintillators: the first defines the start time, while the second provides the stop signal. Neutrons must be detected in temporal coincidence between both planes to contribute to the measurement, which significantly reduces background from scattered neutrons and gamma radiation.
The spectrometer is optimized for high count rates typical of DD fusion experiments, achieving a balance between good energy resolution and high efficiency. TOFOR's measurements provide crucial information on ion temperature, fast-ion distributions generated by auxiliary heating, and potential non-thermal features in the plasma. The technique has been successfully applied in JET to study, for instance, ion heating and redistribution under ICRH and NBI. As one of the reference approaches for neutron emission spectroscopy in tokamaks, TOFOR constitutes a valuable tool for plasma diagnostics [29].

Magnetic Proton Recoil

The Magnetic Proton Recoil (MPR) spectrometer is a high-resolution diagnostic designed to measure the energy spectrum of fusion neutrons, which has been extensively used at JET. Its working principle relies on the nuclear reaction between incident neutrons and a thin hydrogen-rich foil, where neutrons undergo elastic scattering with protons. The momentum of the recoiling protons, directly related to that of the incoming neutrons, is analyzed by a magnetic spectrometer. By detecting the spatial distribution of the protons after deflection in a magnetic field, the original neutron energy spectrum can be reconstructed.
The MPR spectrometer offers excellent energy resolution and is particularly well-suited for studying DT neutrons. This makes it a reference diagnostic for measuring ion temperature and fast-ion dynamics in fusion plasmas. Although its efficiency is relatively low compared to other techniques, the MPR has provided some of the most accurate neutron emission spectroscopy data in tokamaks to date. The system's limitations, including large and complex installations, are outweighed by its contributions to detailed studies of plasma heating and transport phenomena.

Scintillator-based Detectors

Scintillator detectors are widely used in fusion experiments for neutron spectroscopy due to their unique advantages. Their operation relies on the conversion of incident neutron energy into scintillation light through elastic scattering with hydrogen nuclei in the scintillator medium. The resulting recoil protons generate light pulses, which are collected

by a photomultiplier tube. The amplitude of these pulses is related to the energy of the incoming neutrons, while pulse shape discrimination techniques enable the separation of neutron and gamma contributions.
Compact scintillators have been successfully deployed in tokamak environments, including JET, providing high-quality neutron spectrometry over a broad energy range (1.5–20 MeV). Their performance is characterized by an energy resolution of approximately 4% at 2.5 MeV and 2% at 14 MeV [31]. The main advantages of scintillator detectors are their high detection efficiency, compactness, and relatively low cost, making them suitable for both real-time monitoring and time-resolved studies of different plasma heating scenarios. However, the energy resolution of scintillator detectors remains lower than that of magnetic spectrometers. To extract quantitative information, accurate response-function unfolding is required, which can be a challenging task.

Chapter 2

Gas Electron Multiplier Detectors and Diamond Detectors

The previous chapter introduced tokamak experiments and highlighted the two radiation channels central to this work: Soft X-Ray and neutron emission. This chapter outlines the characteristics and operating principles of the detectors that are the focus of this thesis. A Gas Electron Multiplier (GEM) detector is employed as SXR detector on the MAST-U tokamak; a Single crystal Diamond Detector (SDD) is chosen as the detector unit for spectroscopic measurements of DT neutrons in the SPARC neutron camera.

2.1 X-Ray Matter Interaction

The interaction between X-rays and matter depends strongly on both the photon energy and the elemental composition of the medium. Importantly, the energy transfer does not occur as a continuous process, but rather as discrete localized events in which photons are absorbed (and in some cases re-emitted). The absorption probability is described by:

$$I = I_0 e^{-\sigma N X} = I_0 e^{-\mu x}, \tag{2.1}$$

where I is the transmitted photon intensity, I_0 the incident photon intensity, σ the absorption cross-section, N the number of atoms per unit volume, and X the traversed thickness. The parameter μ is the linear attenuation coefficient, and $x = \rho X$ is the mass thickness, with ρ the material density.
Several types of interactions are possible, three main processes dominate depending on the photon energy. At low energies (up to tens keV), the *photoelectric effect* is the most relevant; at intermediate energies, *Compton scattering* becomes predominant; and at higher photon energies (above ~10 MeV), *electron–positron pair production* dominates. Figure 2.1 illustrates the photon interaction cross-sections as a function of energy for carbon.

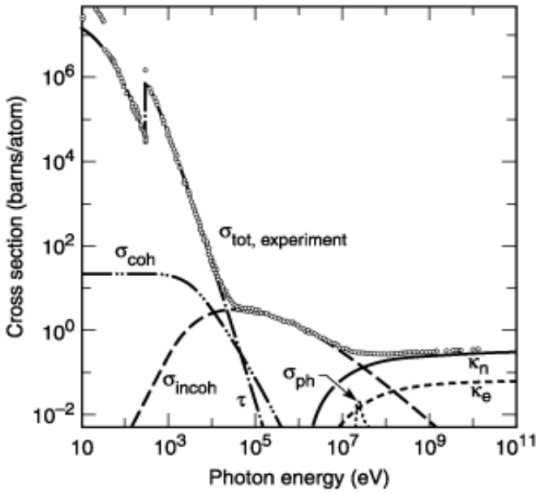

Figure 2.1: Photon interaction cross-sections in carbon as a function of photon energy, showing the relative contributions of the main processes: photoelectric effect τ, coherent (Rayleigh) scattering σ_{coh}, incoherent (Compton) scattering σ_{incoh}, electron–positron pair production in nuclear k_n and electron fields k_e, and photonuclear absorption σ_{ph}. Adapted from [33].

The dominant process for SXR energies is **photoelectric absorption**: a photon interacts with an atom and disappears, transferring its energy to an electron from a bound shell. The emitted photoelectron has an energy given by

$$E_{e^-} = h\nu - E_b, \tag{2.2}$$

where $h\nu$ is the photon energy and E_b the binding energy of the electron. This process leaves the atom ionized, with a vacancy in one of its shells. The vacancy can be filled either by capture of a free electron or by rearrangement of bound electrons, resulting in the emission of one or more characteristic X-rays. These photons may be reabsorbed locally via further photoelectric interactions, or they may escape the medium.

Compton scattering involves the interaction of an incoming photon with a bound electron (assumed at rest). The photon is deflected, losing part of its energy, which is transferred to the recoil electron. The scattered photon energy depends on the scattering angle θ according to:

$$h\nu' = \frac{h\nu}{1 + \frac{h\nu}{m_e c^2}(1 - \cos\theta)}. \tag{2.3}$$

The energy loss ranges from zero (forward scattering) to a significant fraction of the initial photon energy (maximized in back scattering).
Pair production occurs when the photon energy exceeds twice the electron rest mass ($2m_e c^2$ = 1.022 MeV). The photon interact with a nucleus producing an electron-positron pair. The kinetic energy of the pair corresponds to the photon energy exceeding 1.022 MeV.

After slowing down, the positron annihilates with an electron, generating secondary annihilation photons.

2.2 Gaseous Detectors

A gas-based detector relies on the interaction of incoming radiation with gas molecules, resulting in ionization and the creation of a primary cluster of electron-ion pairs. An electric field is usually applied through the gas volume, driving the charged particles to electrodes. The movement of the charges induce a signal collected by the readout electronics. While moving in the gas medium the free charges can undergo additional processes when interacting with neutral molecules, the most relevant being:

1. **Charge transfer**, where an electron is exchanged between a neutral atom or molecule and an ion, effectively swapping their charge states.

2. **Electron capture**, in which a free electron is captured by a neutral species, producing a negative ion.

3. **Recombination**, where a free electron combines with a positive ion, creating a neutral atom or molecule.

4. **Secondary ionization**, occurring when a free electron has sufficient energy to ionize a neutral molecule, producing an additional electron-ion pair and thus multiply the moving charge.

The operational mode of a gaseous detector is determined by the applied electric field that determines the extent of charge multiplication through secondary ionization. The three mostly used regimes are: the ionization mode, where the collected charge is proportional to the number of primary ionizations; the proportional mode, where charge multiplication enhances the signal but keeps a proportionality to the deposited energy; and the Geiger-Müller mode, when the high charge multiplication leads to discharges that produce nearly saturated pulse amplitudes, independent of the primary ionization.

The simplest gas detector consists of a gas volume between two electrodes, where an applied potential difference ΔV creates an electric field. This field drives electrons to the anode and ions to the cathode, generating a measurable signal proportional to the deposited energy. Such detectors excel for highly ionizing particles, such as α particles or heavy ions, which produce signals robustly above electronic noise. When the voltage is sufficiently high, primary electrons gain enough energy to initiate secondary ionizations, triggering an avalanche process known as the Townsend effect, that can be described by the following equation [34].

$$dn = n\alpha dx \quad \Rightarrow \quad n(x) = n(0)e^{\alpha x}. \tag{2.4}$$

Where n is the number of electrons, dx is the traversed length and α the first Townsend coefficient, a gas-dependent parameter that grows with the applied electric field. In a uniform field, α is constant and the growth is exponential. In this proportional regime, the signal is amplified and remains proportional to the deposited energy, making it especially suitable for X-rays, which generate relatively few primary pairs. A main challenge of proportional gaseous detectors is the onset of discharges in the multiplication region: higher voltages increase electron multiplication and signal amplitude but also raise the risk of damaging discharges.
At even higher voltages secondary avalanches can be triggered at different sites by ultraviolet photons emitted during avalanches. This process, called Geiger discharge, quickly escalates into an exponentially increasing number of avalanches. The discharge continues until space charge effects reduce the field below the multiplication threshold. Since the termination condition depends only on the total number of ion pairs rather than the initial ionization, all pulses have the same amplitude. As a result, energy information from the incident radiation is lost in this regime.

2.3 The GEM detector

Gas Electron Multiplier (GEM) detectors are a type of proportional gas detector that belong to the family of Micro-Pattern Gaseous Detectors (MPGD) [35] and were invented and developed by Fabio Sauli at CERN in 1997 [36]. A GEM consists of a thin (usually 50 μm) insulating Kapton foil, coated on both sides with a thin copper layer (5 μm). The foil is perforated with a dense array of bi-conical holes (about 70 μm in diameter with a pitch of 140 μm) arranged in a hexagonal pattern.
When a voltage difference (typically 200–500 V) is applied across the copper layers, a strong electric field is generated inside the holes. The Kapton acts as an insulator, concentrating the field lines within the holes. The bi-conical hole shape reduces the probability of electrical breakdowns by preventing direct metal-to-metal contact. A microscope image of GEM holes and a schematic representation are shown in Figure 2.2.

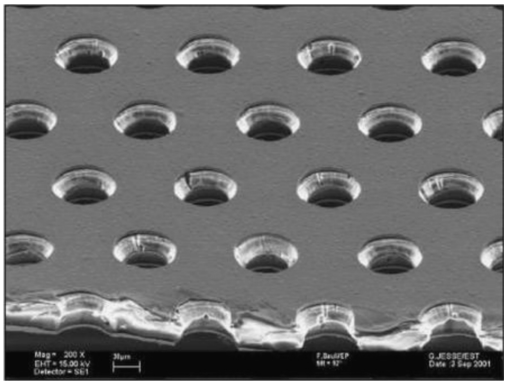

(a) Microscope image of a GEM foil (from [37]).

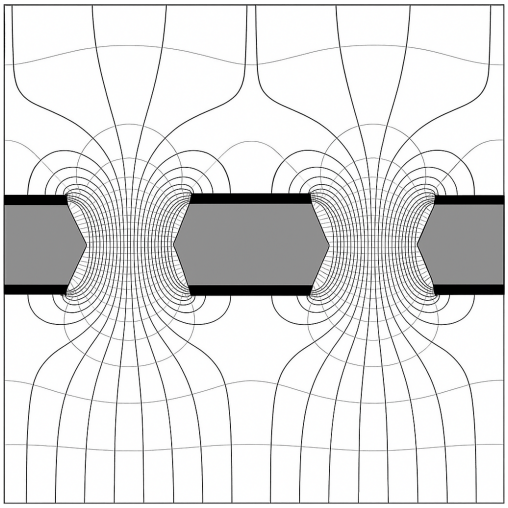

(b) Schematic of a GEM foil cross-section, showing the Kapton foil (grey), copper layers (dark grey), and electric field/equipotential lines (adapted from [37]).

Figure 2.2: Gas Electron Multiplier (GEM) foil.

In the simplest GEM-based detector configuration, the foil is placed in a gas volume between two electrodes. A ionizing radiation produces the primary electrons, which drift through the *drift region* toward the GEM foil. The electron follows the field lines inside the holes, then the strong electric field accelerates them, initiating a Townsend avalanche, the holes can therefore be defined as *multiplication region*. The resulting electron cloud exits the opposite side into the *induction region*, where the charges drift toward the readout electrode and induce a detectable signal. Figure 2.3 shows an example of an avalanche in a single GEM foil simulated with Garfield++ [38], a CERN toolkit for the simulation of gaseous detectors.

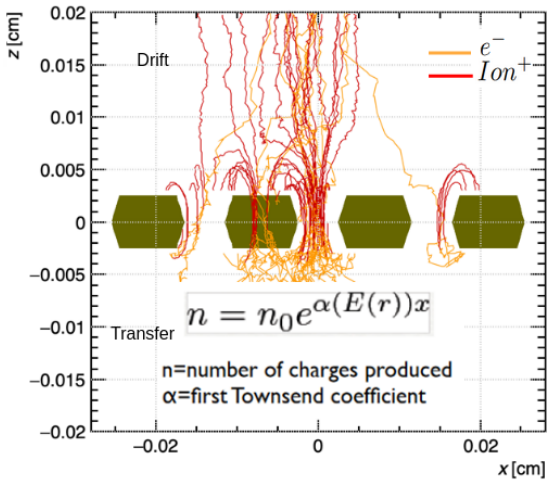

Figure 2.3: Simulation of an avalanche in a single GEM foil with Garfield++.

The main advantages of GEM technology arise from the separation of ionization, multiplication, and induction regions. This configuration yields several benefits:

- Fast time response, since the signal originates solely from electrons reaching the anode.
- High-rate capability and excellent spatial resolution, as multiplication occurs in a large number of microscopic holes.
- Localized damage in case of discharges, which generally do not propagate to the anode and therefore to the sensitive readout electronics.

2.3.1 Triple GEM detector structure and functioning

The multiplication gain of a gaseous detector is defined as the ratio between the number of electrons collected at the readout electrode and the number of primary electrons produced in the gas by the incident radiation. A multiplication gain can be also defined for a single GEM foil with the similar principle: the ratio between the number of electrons before the foil, and after it. The definition is simple:

$$G_{tot} = \frac{N_{\text{out}}}{N_{\text{in}}}, \tag{2.5}$$

where N_{in} is the number of primary electrons (or entering electrons) and N_{out} is the total number of electrons after avalanche multiplication. The effective gain of a GEM detector (or single foil) is determined not only by the intrinsic avalanche multiplication, but also by the fraction of electrons successfully entering and exiting the holes. In the case of a

GEM detector, the gain depends on the electric field inside the holes, the foil geometry, and the gas mixture.
To reach higher overall gains while ensuring stable operation, multiple GEM foils can be cascaded. In such a configuration, the electron cloud produced in the first GEM is transferred to the next, where further multiplication occurs. This scheme allows gains of 10^4–10^5 while keeping the voltage across each individual foil moderate (around 350-400 V), thereby reducing the risk of discharges. The total gain G_{tot} is given by the product of the gains of the individual foils:

$$G_{\text{tot}} = \prod_i G_i, \tag{2.6}$$

where G_i is the gain of the i-th GEM foil, defined as the number of electrons that reach the transfer zone after the GEM i (without falling back on the bottom of the foil) and the number of electrons before the foil.
The most common arrangement of GEM-based detectors is the triple-GEM configuration, consisting of three GEM foils separated by transfer regions, placed between a drift region (where primary ionization occurs) and an induction region (leading to the readout electrode). A schematic of this configuration is shown in Figure 2.4. Thanks to this design, triple-GEM detectors combine high and tunable gain, stability against discharges, and excellent spatial and temporal resolution, making them well suited for high-rate and high-radiation environments.

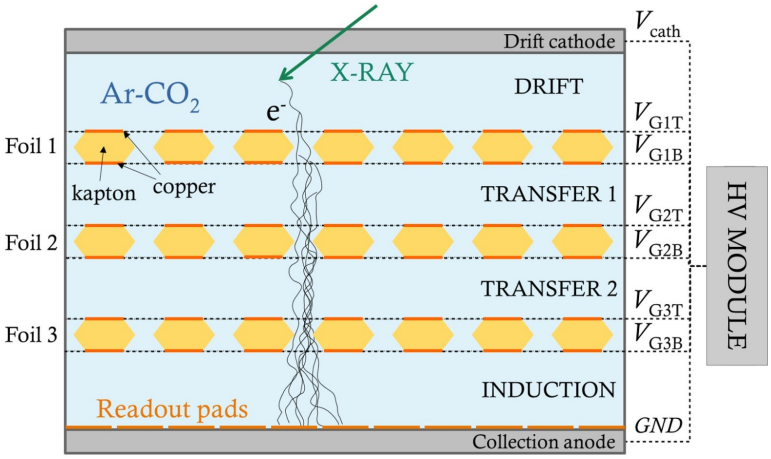

Figure 2.4: Schematic of a triple-GEM detector with signal propagation from a SXR event.

The optimization of a triple-GEM detector involves several parameters. A summary of the most important aspects is provided below, while a detailed assembly routine and characterization of a triple GEM detector is reported in Appendix A.

Electric fields (outside the GEM foils): The drift field must efficiently guide primary electrons into the GEM holes, while limiting transverse diffusion. Transfer fields

are tuned to extract electrons from one GEM and focus them into the next, minimizing losses at the foil surfaces. The induction field maximizes electron collection at the read-out. Typical values are of the order of 1–3 kV/cm.

Gas mixture: GEMs are typically operated with mixtures of a noble gas (e.g., Ar, Ne, or Xe) and a quencher (e.g., CO_2 or CF_4). Noble gases are chosen because they possess a set of key properties: they ionize efficiently, are chemically inert and stable over time, do not significantly reabsorb their own UV emission, provide good electron transport with low attachment probabilities. However, avalanches in noble gases emit UV photons that can trigger secondary avalanches. To suppress this effect and stabilize operation, a quencher gas is added to absorb the UV photons and dissipate energy through molecular excitations. A standard gas mixture for triple GEM detectors is $\mathrm{Ar}{-}\mathrm{CO}_2, 70-30\%$

GEM Voltage distribution: Since the avalanche process is exponential, the Gain is a function of the sum of the voltages applied to the GEM foils. Proper tuning ensures stable operation at high gain, minimizes ion feedback, and reduces discharge probability. A typical operational Gain for SXR measurement is of the order of 10^4, corresponding to a typical cumulative applied Voltage of 1100 V, and electric field of 50kV/cm inside the GEM holes.

2.3.2 GEM detector read-out

Once the electron cloud reaches the induction region, the charge motion induces a current on the readout plate. The readout plate is a conductive surface connected to the front-end electronics. Importantly, its geometry is independent of the GEM foil geometry: the plate can be segmented into pads of arbitrary shapes and dimensions, or into superposed strips [39]. This flexibility allows the readout design to be adapted to the needs of specific applications, typically balancing spatial resolution, count rate capability, and electronic complexity. For example, in tokamak applications the radiation fluxes are substantial, up to $\sim 10^6 \mathrm{counts/cm^2 s}$, therefore the electronic fast rate capability is one of the main requirements, together with stability to high magnetic fields. In the case of this work, the anode is segmented into pads, each read independently by an acquisition channel.
To extract and digitize the induced signals, the detector is coupled to a dedicated acquisition chain based on GEMINI [40] chips, and an FPGA (Field Programmable Gate Array). The GEMINI block diagram is shown in Figure 2.5, together with a schematic of the signal processing step. This setup allows operation in photon-counting mode with an energy resolution of about 30% at 8 keV [41], and a sustainable rate of up to 1 $\mathrm{MHz/cm^2}$.
The GEMINI chip is an Application-Specific Integrated Circuit (ASIC) developed in CMOS 180 nm technology for the readout of GEM-based detectors, consisting of 16 parallel channels. The signal is processed according to the following chain:

1. **Charge-sensitive preamplifier (CSP):** The input current signal (I_{DET}) gen-

erated by electrons reaching the anode is amplified and integrated by a low-noise charge-sensitive preamplifier. The feedback capacitance (C_f) converts the collected charge into a voltage signal (V_{PRE}).

2. **Discriminator with programmable threshold:** V_{PRE} is compared with a threshold (V_{TH}) in a built-in hysteresis comparator. The threshold is provided by an R-2R Digital-to-Analog Converter (DAC), controlled via an $\mathrm{I^2C}$ interface.

3. **LVDS driver:** The discriminator output (V_{DIS}) is converted into a Low-Voltage Differential Signal (LVDS) with a 1.2V offset.

4. **FPGA processing:** The LVDS signals are processed by a custom FPGA, which extracts two information. The *Time of Arrival (ToA)*: the instant the signal exceeds the threshold, with 0.5 ns temporal resolution, this is considered as the photon count event time. The *Time over Threshold (ToT)*: the duration for which the signal remains above threshold, this quantity is related to the deposited charge, and after calibration, is used to retrieve the deposited energy. Both signals are sampled at 2 GHz by firmware running on the readout boards, which use a chain of Time-to-Digital Converters (TDCs). Synchronization is ensured by a pulse-ramp to start acquisition and a 10 MHz reference clock. This clocking scheme enables synchronization of the detector with external systems, such as a tokamak timing system.

5. **Event formatting and transmission:** Each event is encoded into a 64-bit word containing ToA, ToT, and the channel ID. In parallel, a second word containing a global time reference is transmitted, allowing the reconstruction of absolute event timing over long acquisitions.

6. **DAQ and calibration:** The FPGA collects the outputs of multiple ASICs and transmits them to the DAQ PC via a 10 Gbit/s optical link.

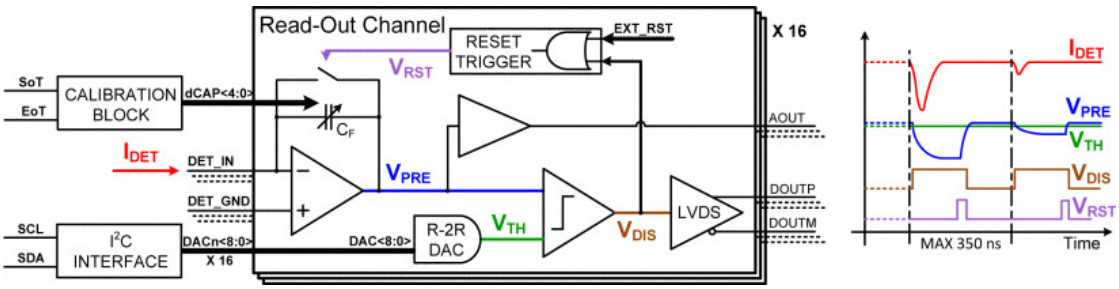

Figure 2.5: Block diagram of the GEMINI ASIC (from [40]).

The output of this process consists of photon counting data that are asynchronous and independent for each pixel, with nanosecond time resolution, although the operational rate is limited to about 1 MHz per channel (and thus per pixel). The energy information

is retrieved through a ToT information, which, after individual channel calibration, is converted into Energy with a nominal energy resolution of 30% at 8 keV.

2.4 Neutron detection

Unlike charged particles or photons, neutrons do not interact directly with bound electrons, therefore their detection is usually mediated by a target material, in which neutron interactions occur and induce prompt energetic charged particles, like protons α particles etc. which are then detected. The interaction cross-section of neutron with matter depends strongly on the energy of the neutron [34]. Since we are here interested in fusion neutrons, at energies of 2.5 MeV, and 14.1 MeV, respectively from DD and DT fusions, we will focus on fast neutron processes. Neutron interactions can be broadly categorized into elastic scattering, inelastic scattering, and absorption processes.

Elastic scattering

In elastic scattering, a neutron collides with a target nucleus and transfers part of its kinetic energy without exciting or transmuting the nucleus. The most effective targets are light nuclei, where large fractions of the neutron energy can be imparted in a single collision. For example, collisions with hydrogen nuclei (protons) are particularly efficient due to the comparable masses of the neutron and proton. Elastic scattering forms the basis of neutron moderation in reactor physics, where successive collisions with light nuclei slow down fast neutrons to thermal energies. For detector applications, elastic scattering is important because the recoil nucleus (e.g., a proton) is charged and can be directly observed in scintillators, gas counters, or semiconductor devices.

Inelastic scattering

At higher neutron energies, inelastic scattering becomes relevant. In this process, the neutron collides with a nucleus, transferring enough energy to excite it into a higher state. The nucleus subsequently de-excites emitting gamma rays or internal conversion electrons. This mechanism provides an indirect way to detect fast neutrons, since the emitted secondary radiation can be observed. Inelastic scattering is particularly relevant for medium and heavy nuclei, where excitation levels lie in the MeV range.

Absorption processes

In absorption interactions, the neutron is captured by the target nucleus. The cross section of this type of processes varies strongly with the interacting nucleus, and can occur over a broad energy range, but is generally higher at thermal energies. After neutron capture, the nucleus can either radiate gamma rays, release charge fragments, or undergo fission.

Fission reactions

For heavy nuclei such as ^{235}U or ^{238}U, neutron absorption can lead to nuclear fission. In this process, the compound nucleus splits into two energetic fission fragments accompanied by the emission of prompt neutrons and gamma rays. The large kinetic energy

deposited by the fission fragments in detector media makes fission reactions particularly suitable for neutron detection. This principle is exploited in fission chambers, which are widely used in fusion experiments for neutron flux monitoring due to their robustness, wide dynamic range, and good discrimination against gamma background.

Moderation-based detectors

Another important class of neutron diagnostics relies on neutron moderation. In these systems, fast neutrons are slowed down through multiple elastic collisions in hydrogen-rich materials until they reach thermal energies, where they can be efficiently detected by capture reactions in materials such as ^{3}He or ^{10}B. Bonner spheres and related REM counters employ this principle using moderators of different thicknesses to obtain spectral information over a wide neutron-energy range. These detectors are particularly valuable for radiation protection and neutron field characterization in fusion environments.

2.5 Single Crystal Chemical Vapour Deposition Diamond Detectors

Diamond has been considered as a suitable detector material for ionizing radiation since the 1940s due to its exceptional intrinsic properties. Early applications, however, were limited by the prohibitive cost of natural diamonds and the poor reproducibility of their performance, which strongly depended on the individual crystal quality. The advent of Chemical Vapour Deposition (CVD) techniques for synthetic diamond growth [42], followed by the development of CVD Single Crystal Diamond Detectors (SDDs), overcame these limitations. As a result, diamond detectors have found applications in the detection of UV, X-rays, γ rays, heavy ions, and neutrons. In particular, SDDs have been successfully employed as neutron spectrometers at JET during both DD and DT campaigns [27, 43].
The key characteristics of SDDs include: a wide bandgap of 5.5 eV, high radiation hardness, low leakage current at room temperature, and insensitivity to visible and infrared photons; a high breakdown field, which enables operation at large bias voltages; compact dimensions (typically a few mm^3), making them suitable for neutron camera applications; fast signal response; low sensitivity to background gamma radiation. Together, these features make SDDs uniquely well-suited for operation in the harsh environment of fusion devices as compact neutron spectrometers.

2.5.1 Principle of operation of diamond detectors

Diamond detectors are solid-state devices where the passage of an ionizing particle generates a measurable current in an external circuit. To fabricate a planar detector, thin metallic electrodes are deposited on two opposite faces of a diamond crystal.
Figure 2.6 illustrates the operating principle of a diamond detector. Diamond is a semiconductive material: particles traversing the crystal ionize electrons and holes, which

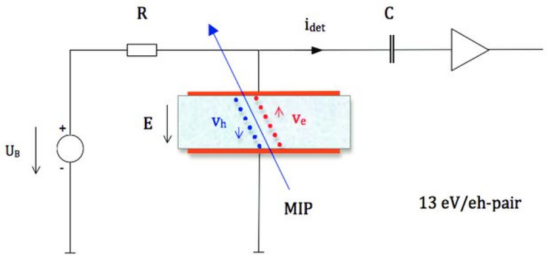

Figure 2.6: Principle of functioning of a diamond detector. From [44]

then drift under an externally applied electric field and induce a current signal in the preamplifier. The ionization energy in CVD diamond is approximately 13 eV/e^-h^+-pair, and the stopping power for minimum-ionizing particles (MIPs) is about 615 eV/μm.
For a single-crystal diamond detector of thickness d = 500 μm, the drift time t_d is of the order of 6 ns under an electric field of 1 V/μm. The corresponding drift velocity is $v_d \approx 10^5$ m/s at a bias voltage U_B = 500 V. The typical front-end readout uses a loading resistor R = 1 MΩ and a coupling capacitance C = 1 nF. [44]

2.5.2 SDD response to neutrons

Neutron detection in diamond is based on the measurement of the charged or electromagnetic products of neutron-induced nuclear reactions, and the efficiency depends strongly on the relevant reaction cross sections. Neutrons can interact directly with the ^{12}C nuclei of the diamond through several mechanisms. Figure 2.7 shows the reaction cross sections of neutrons with carbon nuclei in the MeV energy range, while Figure 2.8 illustrates the response of an SDD to a DT neutron flux.

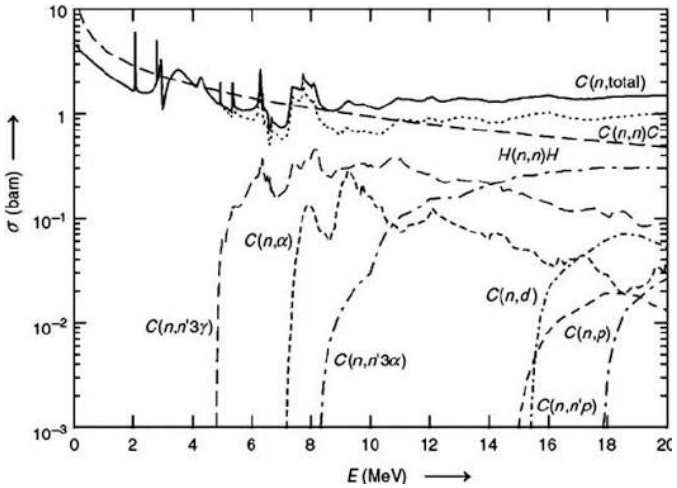

Figure 2.7: Cross sections of various interaction processes of neutrons with carbon nuclei as functions of neutron energy. (from [45]).

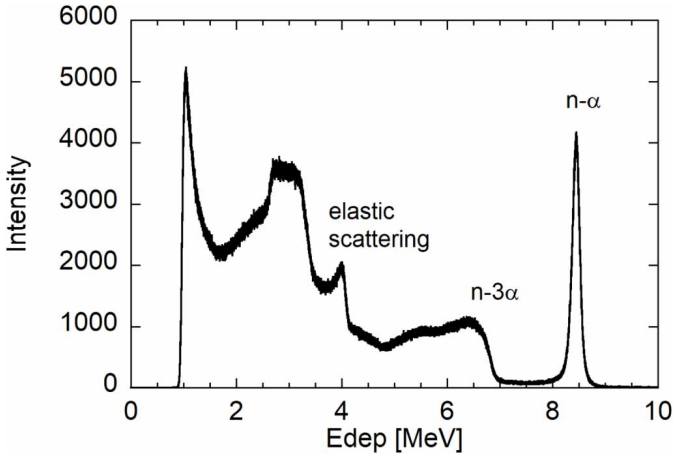

Figure 2.8: Diamond response function to 14.1 MeV neutron irradiation performed at the Frascati Neutron Generator (FNG-ENEA). (from [27]).

The main spectral features arise from:

- Elastic and inelastic scattering: $^{12}\mathrm{C}(n,n')^{12}\mathrm{C}$,
- Three-alpha breakup: $^{12}\mathrm{C}(n,n')3\alpha$ with Q = 7.23 MeV,
- Alpha emission: $^{12}\mathrm{C}(n,\alpha)^{9}\mathrm{Be}$ with Q = 5.7 MeV.

Among these, the $^{12}\mathrm{C}(n,\alpha)^{9}\mathrm{Be}$ reaction is the most relevant for high-resolution 14 MeV neutron spectroscopy. It produces a distinct peak centered at the difference between the incident neutron energy and the reaction Q-value, around 8.3 MeV. This *n–α peak* provides a clean signature of DT neutrons, since the 6 MeV threshold excludes contributions from 2.5 MeV DD neutrons.
The width of the n-α peak contains valuable diagnostic information. It results from the convolution of the detector energy resolution ($\simeq$ 120 keV) and the Doppler broadening caused by the energy spread of the incoming neutrons (see Equation 1.19). The latter reflects the thermal motion of reacting ions, allowing a direct measurement of the ion temperature $\mathrm{T_i}$ of tokamak plasmas through the full width at half maximum (FWHM) of the peak. In the limit of infinite detector energy resolution, the relation becomes [46]:

$$\mathrm{FWHM} = 177 \cdot \sqrt{T_\mathrm{i}}. \tag{2.7}$$

Chapter 3

Development of a multipurpose geometrical transport routine for tokamak radiation studies

This thesis focuses on the development of diagnostic systems that integrate spectroscopic measurements with fast imaging capabilities. To support this goal, a dedicated simulation tool, Revolt [47], and its upgraded version Revolt-U [48], has been developed. These tools are designed both to model and optimize diagnostic performance and to apply inversion methods for assessing local plasma parameters.
Revolt simulates the optical relationship between plasma emission and the radiation detected by the diagnostic system, while Revolt-U extends this framework by including the effects of soft X-ray attenuation through different materials and detector efficiency.
Although several commercial particle transport simulation packages exist, such as GEANT4 [49] and MCNP [50], they are not ideal for early design stages, as their comprehensive and highly accurate nature often comes at the cost of computational efficiency and flexibility when exploring multiple configurations. In this work, we use GEANT4 and MCNP as references to benchmark and validate the outputs of Revolt-U, rather than relying on them as routine design tools. At the same time, multiple diagnostic and transport routines have been developed by individual groups within the nuclear fusion community (an overview can be found in [48]). These tools typically address specific experimental needs or geometries but may not be publicly available. As a result, adopting and applying them to other devices or detector technologies would necessitate substantial developmental efforts. To address the existing limitations in diagnostic development tools and to provide a flexible solution tailored to our diagnostics' requirements, we developed a tool that achieves a balance between accuracy and efficiency, enabling rapid diagnostic design while maintaining reliable results.

3.1 The tomographic inversion problem

In this section, the tomographic inversion problem is introduced, namely the challenge of reconstructing local plasma emission (or parameters) from line-integrated measurements. At the same time, this discussion establishes the framework and terminology that will be used later for discussing the Revolt code and synthetic data generation with Revolt-U. This is because synthetic data production and tomographic inversion represent two complementary sides of the same mathematical problem: the former corresponds to the forward calculation of detector signals from a known emissivity distribution, while the latter seeks to recover the emissivity from those signals.
A detector camera, either for neutron or SXR detection, collects radiation in a set of pixels. The image can be represented as a vector $s \in \mathbb{R}^{\mathrm{m}}$, where "m" is the number of detector pixels, and the value of each element s_i is a quantity related to the flux of radiation, either a current amplitude, a radiation count (in the case of our diagnostics) or similar. The value of s_i is the result of a volume integral of the local emissivity of such radiation ϵ along the field of view (FOV) of the pixel. The effects related to radiation transport, i.e. optical path, attenuation, scattering and so on, can be described by a transport operator L.
If the emitting volume is quantized into n voxels, the emission is $\epsilon \in \mathbb{R}^{\mathrm{n}}$, then the transport operator can also be discretized as a transport matrix $L : \mathrm{m_{pixel}} \times \mathrm{n_{voxel}}$. Assuming L is linear, and without noise effects, the system can be described with a general equation:

$$s = L \cdot \epsilon \tag{3.1}$$

The process of synthetic data generation involves the derivation of s from simulated emission ϵ, while the challenge of tomographic reconstruction centers around the retrieval of ϵ given s.
The production of the transport matrix L is the starting point for both the processes. The general concepts for the production of L in the SXR and neutron cases are here described. For SXR radiation in a nuclear fusion environment the main process that has to be taken into account beyond geometrical-optical considerations (addressed in Section 3.2) is absorption along the traveled path and such problem will be tackled in Section 3.3. For neutrons the low rate of matter interaction and the scattering usually complicates the modelling. Nonetheless in the case of long collimated Line of Sights (LOSs) a geometrical approach offers a qualitatively valid first order approximation.
The inversion problem is first approached using the Tikhonov regularization method, applied to SXR emission images acquired with a GEM-based tangential camera on MAST-U. While Tikhonov inversion is employed for the GEM data (see Chapter 5), signals from the SPARC Neutron Camera are inverted using a custom, more specialized method, presented in detail in Chapter 4.

3.1.1 Dimensionality reduction of the inversion problem.

Standard tomographic camera systems typically consist of a set of two or more cameras with intersecting LOSs on a plasma poloidal plane, producing a grid that combines

camera information for 2D image resolution. An example is the set-up of the SXR diagnostics (including a GEM) on West tokamak [51]. However the diagnostic object of this thesis employs a single camera with a tangential point of view necessitating a different approach, similar to the case of the GEM detector installed on EAST tokamak [52]. To simplify the inversion process, we can significantly reduce the number of voxels by mapping the three-dimensional emission volume onto a two-dimensional surface. This is achieved through a projection method that exploits physical invariants. The idea is illustrated in Figure 3.1. Due to the nature of tokamak plasmas, two possible invariants can be exploited:

1. **Toroidal symmetry:** In this approach, the plasma is assumed to be invariant under toroidal rotations. The advantage is that this assumption does not require additional diagnostic information, relying only on geometry. However, the approximation fails when strong poloidal asymmetries or rotations are present in the plasma emissivity distribution (see schematic example in Figure 3.1).

2. **Magnetic field line invariance:** Alternatively, one may assume that the SXR emission is constant along the magnetic field lines. This is generally valid since electron parallel transport along magnetic field lines is much faster than cross-field transport, therefore the quantities (n_e, T_e, Z_{eff}) can be considered constant along them. The projection is then performed along the helical field lines, which naturally accounts for the plasma rotation. While potentially more accurate, this method depends on the results of magnetic equilibrium reconstruction codes (e.g. EFIT++ [53]). Consequently, the computational cost increases, and the quality of the tomographic inversion becomes strongly dependent on the accuracy of the magnetic reconstruction. This limitation is particularly critical in the plasma core, where equilibrium reconstructions are less reliable due to the edge-localized nature of the magnetic diagnostics.

Since SXR diagnostics are often employed to obtain complementary information on the plasma core, independent of magnetic surface reconstructions, relying on the magnetic field line invariant would risk correlating the results with the equilibrium assumptions. For this reason, the axisymmetric (toroidal invariance) approximation is adopted as the baseline for the inversion algorithm.

3.1.2 The Tikhonov regularization method

Following the Tikhonov approach the inversion problem can be written as the minimization problem:

$$\epsilon_0 = \arg\min_{\epsilon} \|L \cdot \epsilon - s\|. \tag{3.2}$$

The system is generally under-determined, i.e. $m < n$, because of the limited number of available LOS with respect to the number of voxels of the emission space. Moreover, even for the case $m = n$, the problem is usually ill-posed due to experimental issues, such as measurement noise, calibration errors, and positioning inaccuracies. Direct inversion, for

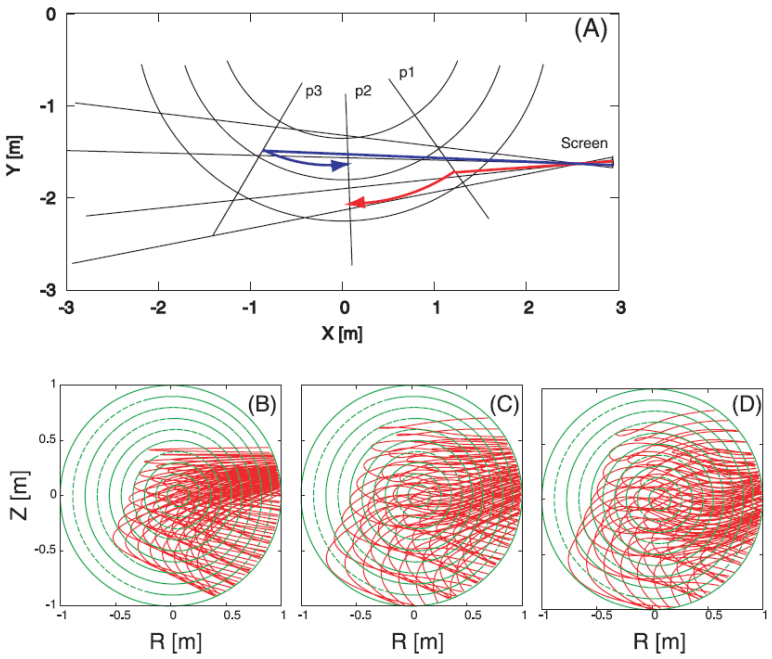

Figure 3.1: A) Red and blue lines are drawn to show how the voxels on LOSs at plane P1 or P3 are projected onto the poloidal reference surface P2. B) projection of the voxels exploiting toroidal symmetry. C-D) projection of the voxels following the magnetic field line, with a weak and a strong poloidal rotation. From [54]

instance through a Singular Value Decomposition (SVD), is therefore highly unstable: small perturbations or rounding errors in the input can lead to unreliable and drastically different reconstructions.
To stabilize the inversion, Tikhonov regularization [55] is one of the common approach in the context of SXR tomographic reconstructions. The idea is to introduce a regularization term into the minimization problem, thereby favoring solutions with specific desirable properties. This is achieved by defining a constraint matrix C, weighted by a free regularization parameter λ, leading to the modified problem

$$\epsilon_0 = \arg\min_{\epsilon} \left\| \begin{bmatrix} L \\ \lambda C \end{bmatrix} \epsilon - \begin{bmatrix} s \\ \lambda C\, \epsilon^* \end{bmatrix} \right\|, \tag{3.3}$$

where ϵ^* represents an *a priori* assumption on the solution. Depending on the scenario, ϵ^* may be set to zero (if no assumption is made) or chosen to represent a reference profile derived from an independent diagnostic. The constraint C can enforce, for example, smoothness of the solution and boundary conditions at the plasma edge.
The Tikhonov approach solves equation 3.2 by the least squares solution. This leads to the equation [56]:

$$(L^T L + \lambda^2 C^T C)\epsilon = L^T s. \tag{3.4}$$

3.1.3 Generalized Singular Value Decomposition

In this work we follow the approach of [52] and [56] to solve Equation 3.4. The generalized Singular Value Decomposition (GSVD) is used to decompose the matrices L and C as:

$$U^T L\, Z = \mathrm{diag}(\sigma), \tag{3.5}$$

$$V^T C\, Z = \mathrm{diag}(\mu), \tag{3.6}$$

where $U \in \mathbb{R}^{m\times n}$ and $V \in \mathbb{R}^{n\times n}$ are orthonormal matrices, $Z \in \mathbb{R}^{n\times n}$ is non-singular, and $\mathrm{diag}(\sigma), \mathrm{diag}(\mu) \in \mathbb{R}^{n\times n}$ are diagonal matrices satisfying

$$0 \le \sigma_1 \le \cdots \le \sigma_n \le 1, \tag{3.7}$$

$$1 \ge \mu_1 \ge \cdots \ge \mu_n \ge 0, \tag{3.8}$$

$$\sigma^T \sigma + \mu^T \mu = I_n. \tag{3.9}$$

The ratios

$$\gamma_i = \frac{\sigma_i}{\mu_i}, \quad i = 1 \ldots n, \tag{3.10}$$

are the generalized singular values of the pair (L, C).
We can also define:

$$\beta = U^T s, \qquad \omega = Z^{-1}\epsilon^*, \tag{3.11}$$

In order to be able to write the regularized solution as:

$$\epsilon_{\lambda,i} = \sum_{j=1}^{n} Z_{ij} f_j \left(\frac{\beta_j}{\sigma_j} + \frac{\lambda^2 \gamma_j^2\, \omega_j}{\sigma_j} \right), \tag{3.12}$$

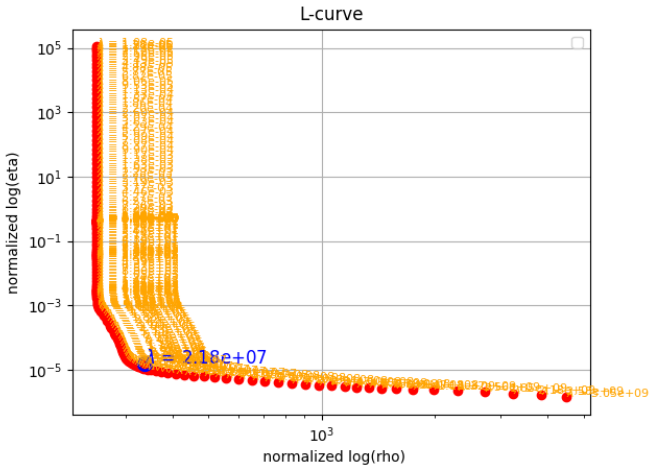

Figure 3.2: Example of an L-Curve from a reconstruction through Tikhonov algorithm of the image obtained with a GEM detector on MAST-U, further details in Chapter 5.

with the filter factors

$$f_j = \frac{\sigma_j^2}{\sigma_j^2 + \lambda^2 \mu_j^2} = \frac{\gamma_j^2}{\gamma_j^2 + \lambda^2}. \tag{3.13}$$

This formulation provides an efficient and numerically stable way to compute the Tikhonov-regularized solution, directly taking into account the conditioning of the system and the effect of the regularization parameter.

3.1.4 Choice of the Regularization Parameter: L-Curve Method

The selection of the optimal regularization parameter λ can be achieved using different methods, in this work the L-curve method is chosen, following the method of [56]. By plotting the residual norm $\|L\epsilon_\lambda - s\|$ against the solution semi-norm $\|C(\epsilon_\lambda - \epsilon^*)\|$ in log-log scale, the L-curve is obtained, an example is shown in Figure 3.2. Its characteristic L-shape allows the corner point (maximum curvature) to be identified, which corresponds to the best compromise between fidelity to the data and smoothness of the solution [56]:

$$\lambda_{\text{opt}} = \arg\max_{\lambda} \kappa(\lambda), \tag{3.14}$$

where $\kappa(\lambda)$ is the curvature of the L-curve.
This method ensures that the reconstructed emission is neither dominated by noise (small λ) nor overly smoothed (large λ), providing physically meaningful and stable results for SXR tomography. The application of this method on the data acquired with a GEM detector on MAST-U will be presented in Chapter 5.

3.2 Revolt

As previously discussed, the geometrical transport code Revolt is developed to produce the matrix L in Equation 3.1. Revolt implements a voxel-based Monte Carlo approach. The source volume, i.e the plasma, is divided into a 3D mesh of voxels. The problem of constructing L can be approximated, in a first geometrical approximation, to calculating which voxels are visible to which detector pixels, and how much they contribute to the total signal detected from each pixel. The challenge arises from the quantization of the emitting volume, which implies that each voxel may contribute both directly to the detector signal and indirectly through partial obstruction by obstacles.

3.2.1 Solid Angle Fraction calculation

The contribution of each voxel to a detector pixel is quantified through the so-called Solid Angle Fraction (SAFRACT), representing the geometrical visibility of the detector to each source region. It is defined as the solid angle subtended by the detector pixel multiplied by the fraction of emitting volume of the voxel that contributes to the pixel signal (assuming that all radiation impinging on the pixel is captured):

$$\text{SAFRACT} = \frac{\Delta\Omega}{4\pi} H\, dV = \frac{dS \cdot \hat{r}}{4\pi d^2} H\, dV [m^3], \tag{3.15}$$

where dS is the pixel surface, d the voxel-to-pixel distance, $\hat{r}$ is the versor between the voxel and the pixel, dV is the voxel volume and H is the shading factor due to obstacles. Calculating the parameter H is the core of Revolt. The matrix L is thus populated with SAFRACT entries, representing the relative contribution of voxel j to the detected signal on the pixel i.
Revolt accounts for obstacles such as collimators, vacuum vessel components, and structural supports. The geometry is modeled analytically with simple solids (cylinders, parallelepipedons, cones) or convex polygons that acts either as collimators or general obstacles.
For each voxel-pixel pair, multiple LOS segments are generated by randomly sampling one point within the voxel volume and one point on the pixel surface; each pair of sampled points defines a line of sight. Revolt then checks for intersections between these lines and obstacles using geometric analytical computations (intersection between line and surfaces of solids). The weight of each voxel on the pixel is proportional to H: the fraction of LOSs that do not intersect with any obstacle over the total amount of lines generated from the voxel-pixel pair.
This approach allows Revolt to model realistic detector geometries with pinholes, apertures, and shaded regions, capturing effects often neglected in purely analytical line-integration methods.

Revolt is implemented in `C`, ensuring efficiency in handling large voxel-pixel combinations. The workflow can be summarized as:

1. Define the 3D world volume and voxel grid.

2. Input detector geometry, position, pixel size, and obstacles from a text file.
3. Perform a pre-check to discard voxels outside the detector view-cone.
4. For each pixel–voxel pair, generate N_{vox} random point pairs.
5. Compute the LoS from the point-pairs and check for intersections with obstacles.
6. Accumulate contributions to L_{ij} using Equation 3.15.

The accuracy of the result is controlled by the number of random samples N_{vox}, which sets the spatial resolution required for each specific application. The statistical uncertainty scales as $1/\sqrt{N_{\text{vox}}}$, offering a trade-off between accuracy and computational cost.

3.2.2 Revolt validation

The Revolt code is tested using toy models to assess its capabilities, with two specific scenarios being discussed here. The first test evaluates the effect of a rectangular collimator edge on representing partially shaded pixels.
In this context, we simulate two cases:

1. The voxel and detector directly face each other, allowing all LOSs from the voxel to be counted.
2. The voxel is offset, resulting in partial visibility to the detector.

The geometry is shown in Figure 3.3. In the latter case, we observe that:

- 50% of LOSs originating from the shaded area are not blocked by the collimator.
- The red area is entirely uncounted, accounting for 25% of LoSs and emission points.
- The white area contributes half of its LoSs to the count if they terminate on the left side of the dashed-blue line.

These findings imply that the expected sensitivity of the absorbed fraction (SAFRACT) for the partially visible model is 62.5% of the fully facing simulation. The SAFRACT value obtained from the direct-facing layout is 0.387 a.u., compared to to 0.240 a.u. in the partially shaded case, corresponding to a scaling factor of 62%.

In the second scenario, a benchmark is performed against the MCNP Monte Carlo transport code. The geometrical setup built both in MCNP and Revolt is composed by a single-pixel detector, at coordinates (-22.8m, -11.5m, 0), observing through a pinhole configuration six sets of voxels arranged in toroidal shapes. Both in Revolt and MCNP all the objects are assumed as completely absorbing materials, and the space is considered vacuum. The LoS are disturbed by a vertical cylinder of absorbing material centered in the origin and with a radius of 1.96 m, and 5 vertical collimating planes, inserted 30 cm after the pinhole, as shown in Figure 3.4a. The set of voxels are 6 horizontal slices of

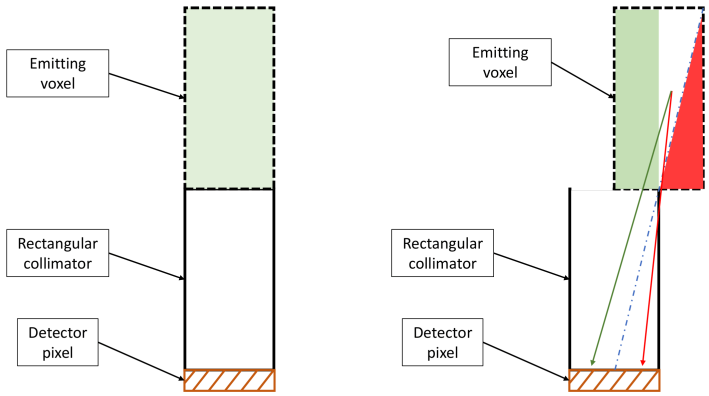

Figure 3.3: Geometries to test the effect of the edge of the collimator on a voxel (dashed black line) adjacent to the collimator. The first simulation (left) is done with voxel and detector facing each other, the voxel is completely seen by the detector, thus completely colored in green. The second simulation (right) is done by shifting the detector so that only half of the volume is facing directly the detector. From [47].

a cylindrical ring, centered in the origin, with internal and external radius respectively of 2.58 and 2.62 m and total height of 0.5 m. To compare the two simulation tools, the SAFRACT is expressed as the probability that a particle emitted from a given ring of voxels reaches the detector, i.e. Equation 3.15 without the voxel volume contribution dV. This probability is obtained by computing the ratio between the sum of obstacle-free lines of sight (LOS) for the emitting ring and the total number of LOS evaluated. The results (Figure 3.4b) show excellent agreement between Revolt and MCNP, with differences below 7% across all voxel rings. The systematic undershoot observed in Revolt is not yet fully understood and remains under investigation.

3.3 Revolt-U: Revolt energy Update

In the Revolt code, it is assumed that radiation propagates through an optically thin medium in the relevant energy range. Consequently, radiation emitted from any point within the source reaches the detector with minimal alterations, except when intersecting components identified as absorbing materials, which are modeled as completely opaque to radiation event. The routine has been upgraded specifically for x-ray pixelated-detector applications on nuclear fusion experiments. Starting from the emissivity of the x-ray source (e.g., a tokamak plasma), Revolt-U calculates counts and energy spectra at each detector pixel, taking into account the detector's efficiency and the x-ray attenuation through various gases and experimental components.
In the Revolt-U framework, in addition to the base obstacle-handling algorithm of Revolt

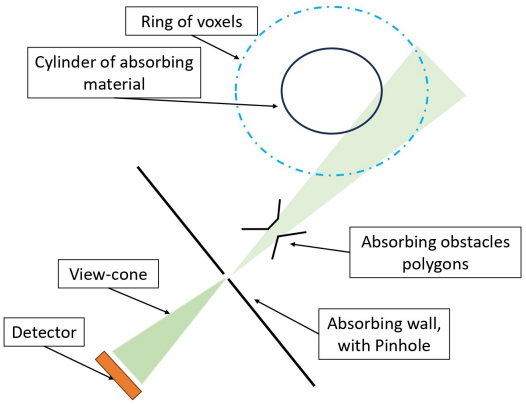

(a) The geometry sketch of the simulated experiment seen from above. From [47].

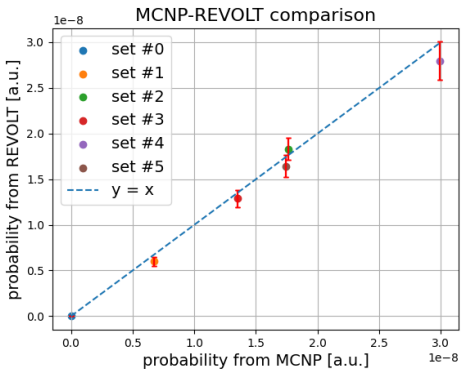

(b) The probabilities for every set of voxels, calculated with the two tools. From [47].

Figure 3.4: Simulation comparison between Revolt and MCNP on a collinated geometry.

—whose effect is embedded in the geometrical matrix L— energy-dependent attenuation along the line of sight is also taken into account. Specifically, the photon flux is reduced according to the absorption coefficients of the materials intersected by the ray path. The resulting synthetic detector data is therefore a function of the energy: $\vec{s} = \vec{s}(E)$, and the relation between source emissivity and detector response is given by:

$$s_i(E) = \sum_j L_{ij} \cdot \int_{E-\Delta E/2}^{E+\Delta E/2} \frac{d\dot{N}_j(E)}{dE}\, dE \cdot \xi_{ij}(E) \cdot e^{-\sum_m \mu_m(E) t_{ijm}}, \tag{3.16}$$

where:

- $s_i(E)$ is the rate at detector pixel i, i.e. the number of detected photons per unit time within the bin,
- E is the central energy of the bin $[E - \Delta E/2, E + \Delta E/2]$,
- dE is the energy differential,
- $\frac{d\dot{N}_j(E)}{dE}$ is the emissivity spectrum of voxel j in the energy range dE,
- L_{ij} is the geometrical element of L linking voxel j to pixel i, including the effect of the absorbing obstacles, i.e. the SAFRACT,
- $\xi_{ij}(E)$ is the detector efficiency at energy E,
- $\mu_m(E)$ is the absorption coefficient of material m, retrieved from the *xraydb* database [57],
- t_{ijm} is the path length through material m for photons traveling from voxel j to pixel i.

The user can define obstacles that are treated as fully absorbing by the original Revolt obstacle-handling algorithm (e.g., tokamak vessel walls or metallic collimators). Other components can instead be modeled as semi-transparent materials and included in the attenuation term through their energy-dependent absorption coefficients, such as beryllium windows used as vacuum–air interfaces (see Chapter 5). The exponential term accounts for SXR attenuation along each material crossed by the line of sight. Any photon interacting with the medium, through the photoelectric effect, Compton scattering, or Rayleigh scattering, is assumed to be fully absorbed and does not reach the detector. This approximation is valid for the typical materials and geometries used in fusion experiments within the [1-20] keV energy range.
For sufficiently fine energy binning, the integral can be approximated by:

$$s_i(E) = \sum_j \left(\int_{E-\Delta E/2}^{E+\Delta E/2} \frac{d\dot{N}_j(E)}{dE}\, dE \right) \cdot L_{ij} \cdot \xi_{ij}(E) \cdot e^{-\sum_m \mu_m(E) t_{ijm}}, \tag{3.17}$$

which can be expressed as:

$$s_i(E) = \sum_j \epsilon_j(E) \cdot SF(i,j,E), \tag{3.18}$$

where:

- $\epsilon_j(E) = \int_{E-\Delta E/2}^{E+\Delta E/2} \frac{d\dot{N}_j(E)}{dE}\, dE$ denotes the emissivity of voxel j within the energy bin $[E - \Delta E/2,\, E + \Delta E/2]$.
- $SF(i,j,E) = L_{ij} \cdot \xi_{ij}(E) \cdot e^{-\sum_m \mu_m(E) t_{ijm}}$ defines the spectral sensitivity tensor, which extends the projection matrix L to include energy dependence. The computation of L_{ij} follows the same approach as implemented in *Revolt*.

A key advantage of the SF tensor is that it is independent of the input emissivity, enabling its reuse for energy-resolved tomographic reconstructions.
The efficiency function $\xi_{ij}(E)$ can be provided directly as an input to Revolt-U. Alternatively, users can specify the detector geometry, active material and detection mechanism, from which Revolt-U computes the analytical efficiency. In the case of GEM detectors, the detection efficiency is determined by the gas absorption coefficient, given by:

$$\xi_{ij}(E) = \left(1 - e^{-\mu_m^{\mathrm{tot}}(E) t_{ij}}\right) \cdot \frac{\mu_m^{\mathrm{ph}}(E)}{\mu_m^{\mathrm{tot}}(E)}, \tag{3.19}$$

where m denotes the gas in the detector's sensitive volume, t_{ij} is the SXR path length within the conversion region (assuming it starts from the center of voxel j and reaches the center of pixel i), and μ_m^{tot} and μ_m^{ph} are the total and photoelectric absorption coefficients, respectively.
The simulated detector response in Revolt-U currently accounts only for the energy deposited in the drift volume. The subsequent stages, signal amplification and electronic processing, can be studied using existing tools, namely Heed [58] and Garfield++. These

programs provide detailed simulations of primary electron generation by incident x-rays, electron multiplication in the gas and GEM foils, and the resulting charge distribution within the detector's induction region.
A simplified internal model for these subsequent processes has not yet been implemented within the Revolt-U toolkit and represents a promising direction for future development. An example of such an approach can be found in the work of Amoroso *et al.* [59].

3.3.1 Energy simulation

To compute synthetic detector data, Revolt-U requires a definition of the x-ray source emissivity, meaning that an energy spectrum must be assigned to each voxel representing the source volume. These spectra can be obtained from independent simulations that account for all contributions to SXR emission (i.e., Bremsstrahlung, radiative recombination, and line radiation) and provide accurate spatial profiles, for example through tomographic reconstruction of experimental data. However, such detailed simulations are often unavailable, or they may only provide the power per unit volume (W/m^{-3}) rather than the full energy spectrum for each voxel. In these cases, Revolt-U computes voxel energy spectra using a simplified model based on accessible experimental plasma parameters and magnetic surfaces. This section describes this calculation method.
Since Revolt-U has primarily been applied to GEM detectors in magnetic confinement fusion experiments, the code assumes a thermonuclear plasma source and a detection energy range of approximately [1-20 keV]. It assumes that SXR emission around 1 keV is dominated by bremsstrahlung radiation, a condition that is not valid across the entire SXR energy range but is applicable to the MAST-U plasmas considered in this thesis. In fact, the electron temperature in MAST-U plasmas is around 1 keV [18] and is therefore insufficient to excite impurities that would emit in the 4-20 keV range. In addition, the beryllium filter and the air gap between the tokamak vacuum vessel and the GEM detector in the MAST-U setup absorb emission lines below approximately 3 keV (see Chapter 5). The plasma is modeled as Maxwellian, with an effective atomic number Z_{eff} representing the average ion charge state:

$$Z_{\text{eff}} = \frac{\sum_i n_i Z_i^2}{\sum_i n_i Z_i}, \tag{3.20}$$

where: n_i is the density of ions of species i and Z_i is the charge number of ions of species i, and quasi neutrality is assumed: $\sum_i n_i Z_i = n_e$. The plasma temperature determines both the mean and standard deviation of the electron energy distribution in a voxel, while the electron density and ion effective charge affects the emission intensity. The corresponding Bremsstrahlung emissivity spectrum, i.e., the number of photons emitted per unit time, energy, and volume, is obtained from 1.11 is:

$$\frac{dN}{dE\,dt\,dV}\left[\frac{\#ph}{sm^3eV}\right] = \zeta\left[\frac{\#pheV^{1/2}m^3}{s}\right] \times \frac{Z_{\text{eff}} n_e^2[m^{-6}]}{E[eV]T^{1/2}[eV^{1/2}]} \times \exp\left(-\frac{E[eV]}{T[eV]}\right), \tag{3.21}$$

where: $\#ph$ is the number of photons,$\zeta = \alpha \cdot u$ is a global scaling factor, with $u = 10^{-19}$ and α can be derived by comparison with experimental data (as in Section 5) or kept as 1, E the photon energy. The parameters T, n_e, and Z_{eff} vary across the plasma volume:

$$T = T(\vec{x}), \tag{3.22}$$
$$n_e = n_e(\vec{x}), \tag{3.23}$$
$$Z_{\text{eff}} = Z_{\text{eff}}(\vec{x}), \tag{3.24}$$

with $\vec{x} = (R, \varphi, Z)$ representing the voxel position in cylindrical coordinates. In most cases, full 3D profiles are not available, and measurements are taken at a fixed toroidal angle φ_0, on the midplane Z_0 such that:

$$T(R, \varphi_0, Z_0) = T(R), \tag{3.25}$$
$$n_e(R, \varphi_0, Z_0) = n_e(R), \tag{3.26}$$
$$Z_{\text{eff}}(R, \varphi_0, Z_0) = Z_{\text{eff}}(R). \tag{3.27}$$

Using this information, SXR emissivity for all voxels is calculated via the poloidal magnetic flux $\psi(R, \varphi, Z)$, assuming $\{T(\vec{x}), n_e(\vec{x}), Z_{\text{eff}}(\vec{x})\}$ are constant along flux surfaces. If ψ is available at multiple toroidal angles, Revolt-U can perform a full 3D emissivity calculation.
In most practical applications, however, simulating the entire toroidal volume is unnecessary. Revolt-U requires only the emissivity in the toroidal region visible to the detector, which usually covers a small fraction of the toroidal sector where toroidal symmetry can be assumed. This approximation remains valid even in non-axisymmetric configurations.

3.3.2 Revolt-U validation

To assess the accuracy of Revolt-U, its results are compared with detailed particle transport simulations performed using the well-established GEANT4 toolkit. The comparison focused on validating the attenuation models and detector efficiency model implemented in Revolt-U under conditions representative of typical soft x-ray (SXR) diagnostics. Two scenario are studied: a Toy Model, i.e. a simplified geometry, and a geometry relevant to the installation of a triple GEM detector on MAST-U tokamak. The total execution time for these simulations are also monitored and reported, to give a qualitative intuition of the time saved by the Revolt-U routine.
In both the simulations the detector is a $ArCO_2, 70-30\%$ GEM detector, $10 \times 10\text{cm}^2$, 5mm thick, with an entrance window of Aluminated Mylar $13\mu m$ thick as the cathode.

Toy model comparison: Energy spectrum

In the toy simulation, both the voxel and the detector are placed in vacuum. The vertical (y) and horizontal (x) coordinates of the voxel center coincide with those of the detector

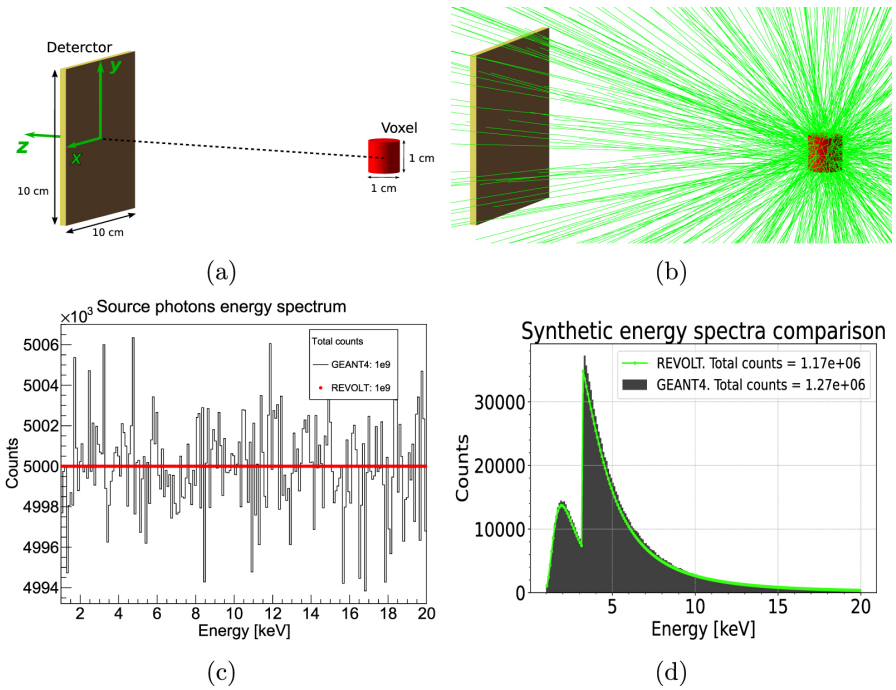

Figure 3.5: Revolt and GEANT4 comparison with the same model (toy model). Figure (a) shows the geometry and the coordinate system used in both cases. Figure (b) shows the isotropic emission of X-rays (only 300 shown in the picture for clarity). Figure (c) shows the overlap of the energy spectra of X-rays coming from the sources. Figure (d) shows the overlap of the "detected" energy spectra. From [48]

center, while the voxel is positioned 20 cm away from the detector along the z-axis, measured from the Mylar entrance window. The geometry and coordinate system are illustrated in Figure 3.5.a.

In Revolt-U, x-rays are emitted isotropically by construction. To ensure consistency, the angular distribution of primary photons in GEANT4 was manually set to isotropic as well, as shown in Figure 3.5.b. In both simulations, the voxel emits 10^9 primary photons with a uniform energy distribution between 1 and 20 keV, divided into 200 energy bins (Figure 3.5.c).

In GEANT4, the counts in each bin depend on Monte Carlo statistics and therefore exhibit random fluctuations around the mean value. In contrast, Revolt-U defines the energy distribution analytically, producing a perfectly flat spectrum that corresponds to the average level of the GEANT4 bins. Figure 3.5.d presents the synthetic energy spectra detected in both simulations. In GEANT4, the detected spectrum was obtained using the *G4EmStandardPhysics* physics list and considering only events involving photoelectric absorption, assuming full energy deposition.

The absolute and relative residuals between the two spectra are shown in Figure 3.6. The absolute residuals correspond to the bin-by-bin difference between GEANT4 and Revolt-U spectra, while the relative residuals are obtained by dividing these differences

by the GEANT4 counts in each energy bin. The absolute residuals reach their maximum near the argon absorption edge (~3.2 keV), whereas the relative residuals remain generally stable at around 10%. The increased scatter in the relative residuals above 12 keV is likely due to the reduced number of counts in the corresponding GEANT4 bins, which amplifies statistical fluctuations in the ratio.
Both the absolute and relative residuals reveal a positive deviation of GEANT4 with respect to Revolt-U, indicating that Revolt-U slightly underestimates the detector counts. To investigate the origin of this bias, several simulations were performed by varying parameters such as the number of energy bins, voxel size, detector distance, and source geometry (including a point-like source located at the voxel center in GEANT4 to better reproduce Revolt-U assumptions). The systematic underestimation persisted in all cases. This behavior is attributed to the intrinsic difference between the two approaches: GEANT4 performs stochastic, step-by-step photon transport including photon scattering with the surrounding materials, whereas Revolt-U applies a deterministic Lambert–Beer attenuation model, which can slightly underestimate transmission. Additionally, small discrepancies between the photo-absorption cross sections used in GEANT4 and those implemented via the XrayDB library in Revolt-U may further contribute to the observed bias. Since a deep understanding of the discrepancy has not been achieved yet, further investigations are needed.
The relative root mean square error (rRMSE) between the detected spectra from the two tools is calculated as:

$$\text{rRMSE} = 100 \cdot \sqrt{\frac{1}{N}\sum_{i=1}^{N}\left(\frac{h_g^i - h_r^i}{h_g^i}\right)^2}, \tag{3.28}$$

where h_g^i and h_r^i represent the counts in the i-th energy bin for GEANT4 and Revolt-U, respectively. The resulting rRMSE value is 8.99%, indicating that Revolt-U reproduces the spectral shape and absolute counts of GEANT4 within 10% accuracy. This level of agreement is considered satisfactory for diagnostic conceptual design and optimization, which is the intended scope of Revolt and for which order-of-magnitude accuracy is sufficient. High-fidelity analyses instead rely on dedicated state-of-the-art tools optimized for this purpose. Both simulations were executed on the same computer (MSI Raider GE67HX, Intel Core i7 CPU). Revolt-U was run in single-thread mode, whereas GEANT4 used all 24 available threads. Under these conditions, the total computation time was 555 ms for Revolt-U and 56.53 minutes for GEANT4, demonstrating the significant computational efficiency of the deterministic approach.

Toy model comparison: 2D image

In this section, the two-dimensional synthetic image produced by Revolt-U from the toy model is compared with the one obtained using GEANT4. The Revolt-U model follows the configuration described in the previous Section 3.3.2, with the only difference being that the detector is divided into a 16×16 pixel grid, covering an active area of 10 cm along both the x and y axes. The GEANT4 model is identical to that used in Section 3.3.2, without modifications.

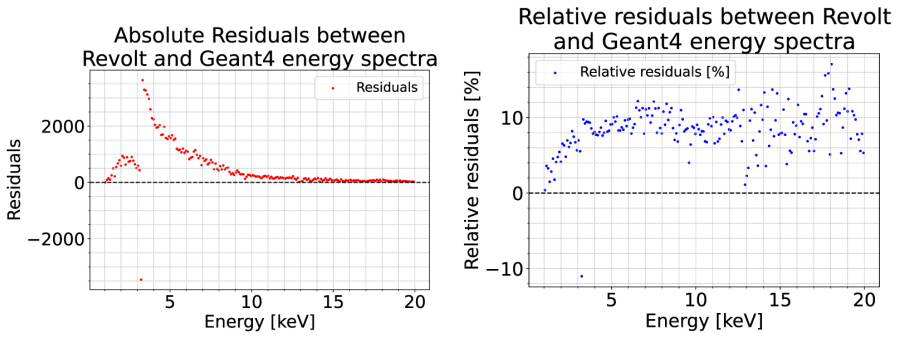

(a) (b)

Figure 3.6: Absolute (a) and relative (b) residuals between the energy spectra obtained with GEANT4 and Revolt-U in the toy-model simulations. The details about the procedure used for their calculation are provided in the text. From [48]

By design, Revolt-U directly computes the counts for each detector pixel as described in Section 3.3. In GEANT4, on the other hand, it is possible to record the coordinates of the interaction points where photons undergo photoelectric absorption in the detector material. Each detected event therefore produces an (x, y) coordinate pair corresponding to the interaction position. These coordinates are accumulated into a two-dimensional histogram with a number of bins equal to the number of detector pixels (16×16). The resulting 2D images from both simulations are shown in Figure 3.7.
The relative residuals (R_{rel}) are defined as:

$$R_{\text{rel},i} = \left| \frac{s_i^g - s_i^r}{s_i^g} \right|,$$

where i denotes the pixel index, and s_i^g and s_i^r represent the counts in the i-th pixel simulated with GEANT4 and Revolt-U, respectively. In addition to pixel-by-pixel residuals, the root mean square errors (RMSE) of the relative and normalized residuals is computed as:

$$\text{RMSE}_{\text{rel}} = 100 \cdot \sqrt{\frac{1}{n} \sum_{i=1}^{n} R_{\text{rel},i}^2}, \tag{3.29}$$

where n is the total number of detector pixels ($16 \times 16 = 256$). The relative resiudals, along with the corresponding RMSE value, are reported in Figure 3.8. The relative RMSE, which quantifies deviations in absolute counts with respect to GEANT4, is equal to 6.72%, consistent with the rRMSE obtained from the energy spectrum comparison in Section 3.3.2.
In summary, the discrepancies between the 2D images generated by Revolt-U and those obtained from GEANT4 are minor and remain well within the accuracy requirements typically expected for diagnostic design and validation in nuclear fusion applications.

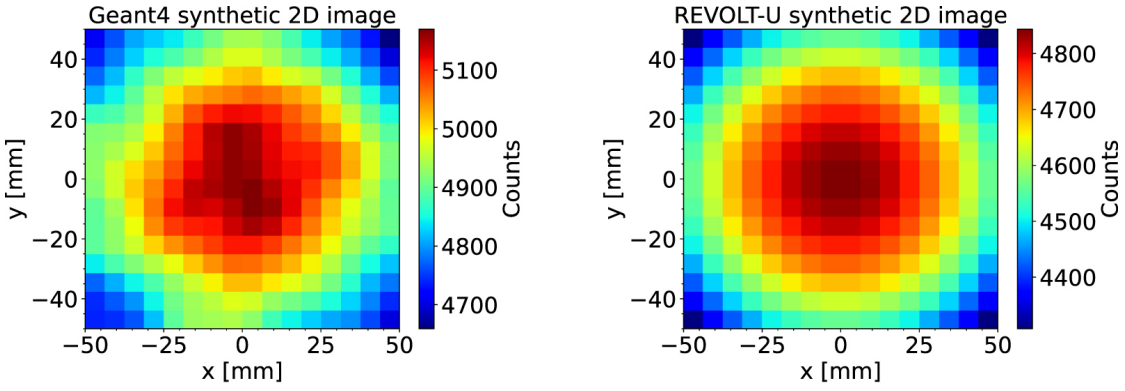

(a) (b)

Figure 3.7: Two-dimensional synthetic images at the detector, simulated with GEANT4 (a) and Revolt-U (b), using the simple toy model.

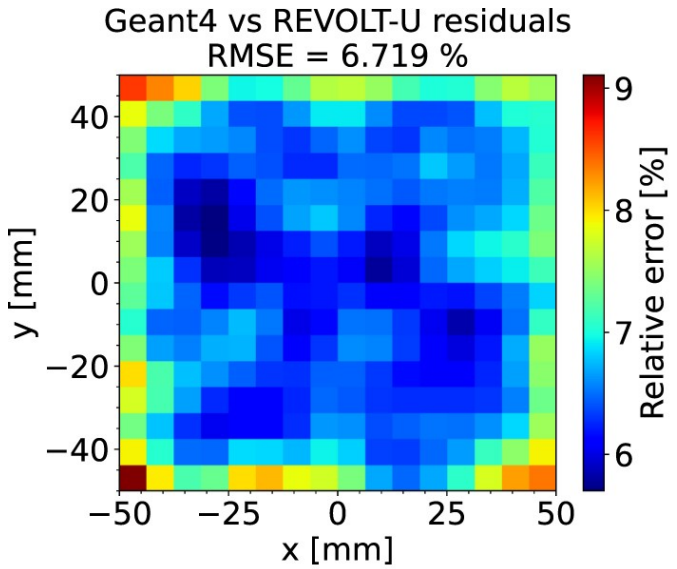

Figure 3.8: The relative residuals and the corresponding RMSE between the GEANT4 and the Revolt-U detector images.

Complex geometry validation

A second validation is carried out using a more complex geometry, based on the CAD model of the line of sight (LOS) of a GEM detector installed on MAST-U during the MU-03 experimental campaign in 2024 (see Chapter 5 for details on the installation and the respective results). The complete geometry was imported into GEANT4 using the *CADMesh* class, which allows direct conversion of CAD models into GEANT4-compatible volumes. For Revolt-U, this step was not required, as the simulation only needs the definition of the apertures through which x-rays can propagate, the obstacles they encounter, and the path lengths through the materials along each line of sight. This approach leads to a substantially simplified representation of the geometry. Nevertheless, if desired, the full CAD model can also be imported into Revolt-U for higher-fidelity comparisons.
A scheme of the CAD model, along with a schematic illustration of the materials traversed by x-rays before reaching the detector's conversion region, is presented in Figure 3.9.
In both simulations, the x-ray source emissivity was modeled according to a Maxwellian distribution of photon energies as in eq. 1.11, which is reported here for readability:

$$\epsilon_{Brem}(E,\bar{x},t) \propto E \cdot n_e(\bar{x},t)^2 \cdot Z_{eff} \cdot T_e(\bar{x},t)^{-1/2} \exp\left[\frac{-E}{k_B T_e(\bar{x},t)}\right] \tag{3.30}$$

The plasma temperature T was set to 1 keV in both simulations, the proportionality constant in the emissivity law was assigned arbitrarily to 1. This simplification is justified since the comparison was performed after normalizing both the detected and source energy spectra. The simulated source energy spectra are shown in Figure 3.10.a, while Figure 3.10.b displays the corresponding energy spectra at the detector, together with their residuals.

In GEANT4, the x-ray source was modeled as a beam uniformly illuminating the entire beryllium window area. In contrast, in Revolt-U, the x-ray emission was isotropic and originated from a single voxel. To account for differences in source configuration between the two simulations, both detected spectra were normalized prior to comparison. Despite this conceptual difference, the two normalized spectra show consistency: the residuals, shown in green in Figure 3.10, remain within the range of −6% to +4%. This level of agreement confirms that both simulation approaches reproduce the underlying physical processes governing x-ray transport and detection with high consistency.
Regarding computational performance, both simulations were executed on the same workstation (MSI Raider GE67HX equipped with Intel Core i7 processors). GEANT4 was run using all 24 available threads, while Revolt-U operated in single-thread mode. Under these conditions, the total computation time for Revolt-U was 830 ms, compared to 1 hour and 34 minutes for GEANT4. A comparison of the execution times for both the toy-model and MAST-U geometries is shown in Figure 3.11.
The large difference in computational time, exceeding three orders of magnitude, is given by the fundamentally different approaches adopted by the two simulation tools. GEANT4 performs step-by-step stochastic transport for each photon, explicitly modeling every interaction, whereas Revolt-U relies on deterministic analytical solutions based

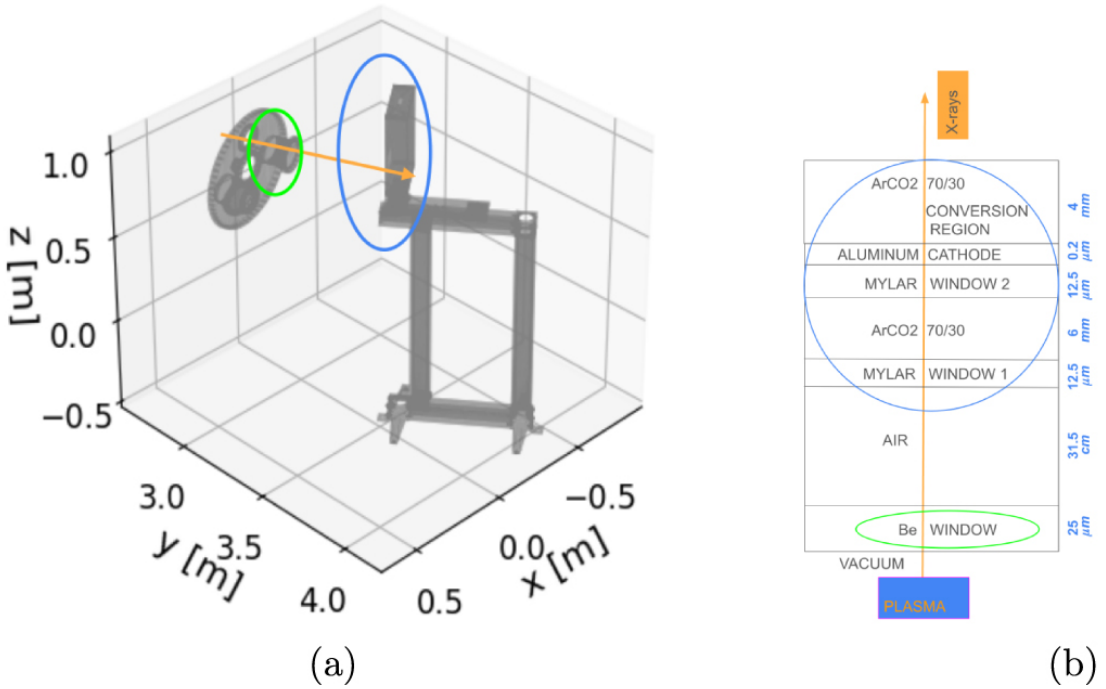

Figure 3.9: Geometry and materials of the detector line of sight used for the Revolt-U validation with GEANT4. In (a), the three-dimensional CAD drawing is shown, with a green circle indicating the location of the x-ray exit window (beryllium window), a blue circle indicating the detector position, and an orange arrow representing the path of the detected x-rays. The detector is housed in a metal box, which acts as a Faraday cage to shield against electromagnetic disturbances. The front face of the box has an aperture that allows x-rays to reach the detector without absorption in the metal. (b) Illustrates a schematic of the materials traversed by x-rays, from the plasma to the detector conversion region. To maintain clarity, components such as access ports, flanges and flange adapters are omitted. However, these components have been modeled in Revolt-U, taking into account the actual dimensions of their apertures and assuming fully absorption of x-rays by their walls. The thickness of each material is displayed in blue text. From [48].

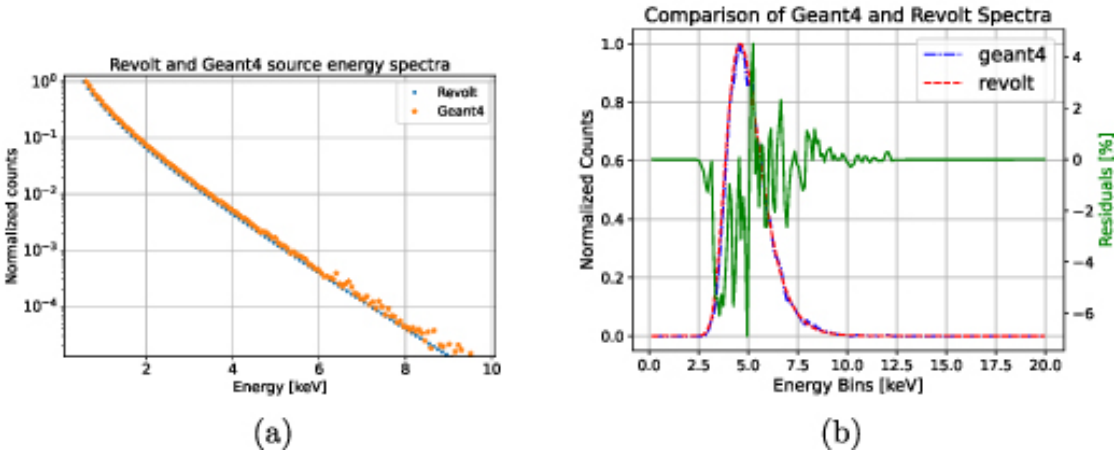

Figure 3.10: (a) Comparison between the normalized source energy spectra defined in Revolt-U and GEANT4 simulations. (b) Comparison between the normalized 'detected' energy spectra obtained from the GEANT4 simulation (shown in blue) and the Revolt-U simulation (shown in red). The green data represent the residuals calculated as the bin-by-bin difference between the GEANT4 and Revolt-U normalized energy spectra.

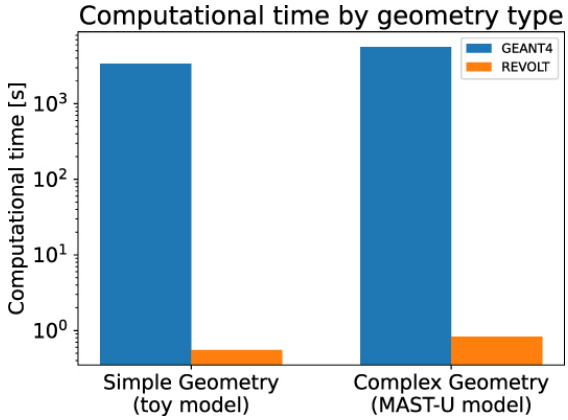

Figure 3.11: Comparison of Revolt-U and GEANT4 computational times by different geometry types. The computational times are represented in logarithmic scale. All simulations were run on the same computer (MSI Raider GE67HX with Intel i7 cores). GEANT4 simulations used all 24 available threads, while Revolt-U simulations ran in single-thread model.

on the Lambert–Beer law. This distinction makes Revolt-U particularly well suited for applications requiring the simulation of large photon populations or complex geometries, where computational efficiency is a priority. It is important to note, however, that a direct quantitative comparison of computational time is not entirely straightforward. In GEANT4, runtime depends on several factors, including the number of primary particles, the physics list used, the step size, the range cut for secondary generation, and the number of processing threads. In contrast, the computational time in Revolt-U depends primarily on the number of plasma voxels, detector pixels, energy bins, geometric paths

for shading calculations, and the number of threads used. Notably, the number of primary particles does not influence the computation time in Revolt-U, since it appears only as a multiplicative parameter in the analytical formulation.
For both benchmark cases discussed, Revolt-U was executed in single-thread mode, while GEANT4 employed all available cores. This makes the observed difference in computation time even more striking. Additionally, while both codes include an equivalent concept of detector pixelation, their scaling behavior differs: in Revolt-U, runtime increases linearly with the number of pixels and voxels, whereas in GEANT4, it is only weakly affected because spatial distributions are typically reconstructed in post-processing.
The purpose of this comparison is therefore not to provide a detailed quantitative performance benchmark between the two tools, but rather to demonstrate qualitatively the substantial computational efficiency of Revolt-U, achieved at the cost of a loss in accuracy for typical nuclear fusion diagnostic applications.

Chapter 4

Design Optimization Study of the SPARC Neutron Camera

Neutron measurement plays a critical role in the operation and research goals of the SPARC tokamak, serving as the primary tool for monitoring fusion power, researching in burning plasma physics, validating neutronics simulations, and providing machine protection feedback [60].
This chapter presents a design optimization study of the SPARC Neutron Camera (NCAM). The NCAM employs up to 19 collimated Line-of-Sight (LOS) offering spatial and time-resolved high-resolution neutron spectroscopy measurements to characterize neutron emissivity, infer ion temperature profiles, and study the ion distribution in the plasma. The geometric sketch of the NCAM LOSs is shown in Figure 4.1, while a technical CAD is shown in Figure 4.2.
The NCAM detectors are designed to achieve an energy resolution ΔE from 1.7% (DT) to 4% (DD) and allow near real-time analyses of the T_i profile, with the ability to separate D and T ions using spectrometry for fusion fuel ion ratio measurements. Ion temperature measurement will be achieved using the Equation 2.7 in the assumption of the SPARC plasma being Maxwellian, with negligible effects related to fast ion population, because SPARC will operate without NBI and is expected to reach the burning plasma regime [61]. The ion temperature is estimated to range between 2 and 20 keV.
Two detectors are being exploited in each NCAM channel: Single Crystal chemical vapor deposition Diamond (SDD) detectors and liquid organic scintillators [62]. Liquid organic scintillators operate effectively in the 1-5 MeV neutron energy range, but have high sensitivity, leading to pulse pileup in DT operation. SDDs provide high radiation hardness, energy resolution and small size, which reduces neutron sensitivity and ensures, together with their count rate capability (up to 1 MHz), compatibility with intense fluxes, making them suitable for DT spectrometry.
This work evaluates the NCAM ability to reconstruct T_i (and emissivity) profiles using diamond detectors by developing a synthetic diagnostics framework. The objective is to define a minimal diagnostic configuration that meets the performance needs throughout the SPARC lifecycle, in terms of total diamond crystals exploited and number of LOSs

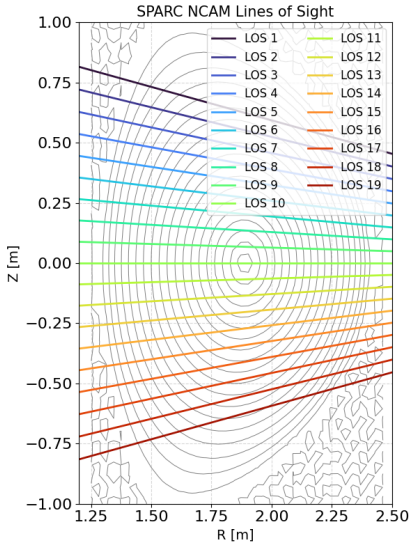

Figure 4.1: Geometry of the LOSs of the Neutron Camera. The LOSs are numbered from 1 to 19 and are symmetric about LOS 10, which corresponds to the horizontal view. LOS 10 is occupied by the Magnetic Proton Recoil, therefore is not available for the NCAM.

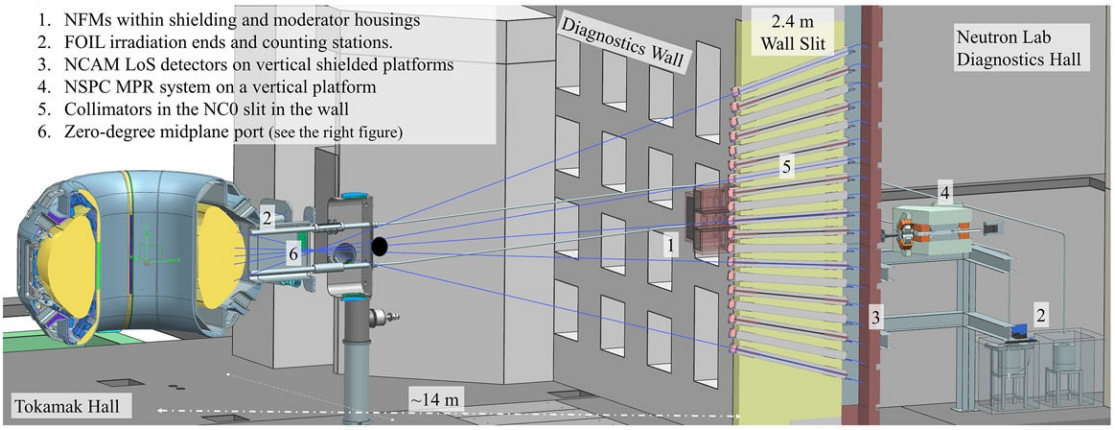

Figure 4.2: Positioning of various NTRN systems in the tokamak and diagnostic halls. From [60].

populated with a detector. The resulting system aims to deliver T_i profiles with < 10% uncertainty at time resolutions better than 100 ms, for a wide range of SPARC fusion power from 1 MW up to 140 MW, while scintillators will operate from lower fusion power up to few MW.

4.1 Dynamic Range Challenge

SPARC is designed to operate up to a fusion power P_{FUS} = 140MW, corresponding to the tokamak total neutron yield spanning more than three orders of magnitude, up to $5 \cdot 10^{19}$n/s [60].
The following workflow summarizes the procedure used in [61], and adopted in this work, to estimate fluxes at the LOS endpoints, starting from experimental plasma profiles and nuclear cross-section data.

1. **Plasma parameters:** Electron density and ion temperature profiles for the reference 140 MW plasma scenario are interpolated over an (R, Z) grid following the reference magnetic equilibrium surfaces estimated through EFIT [63] calculation. Deuteron and triton densities are set as $n_D = n_T = n_e/2$.

2. **Nuclear cross-section:** The D(T,α)n reaction cross-section is computed from tabulated $S(E)$ [64] data using

$$\sigma(E) = \frac{S(E)}{E} e^{-B_G/\sqrt{E}},$$

   where B_G is the Gamow factor.

3. **Local emissivity:** Assuming a Maxwellian ion energy distribution, the local emissivity is obtained as

$$\epsilon(R, Z) = n_D n_T \int \sigma(E) v(E) f(E, T_i)\, dE,$$

   with $v(E) = \sqrt{2E/\mu}$ and $f(E, T_i)$ the normalized Maxwellian.

4. **Outputs:** 2D maps of density, temperature, and emissivity, together with emissivity profiles versus normalized radius ρ are produced combining the local emissivity and the parameters maps.

5. **Fusion power normalization:** The emissivity profile are normalized on several fusion power values to estimate the quantity at different fusion power scenarios. It is assumed that the emissivity scale linearly with the Fusion Power: $\epsilon(P_{FUS}) = \epsilon(140MW) * P_{FUS}/140MW$.

6. **Flux at the endpoints:** The emissivity along each LOS Field of View(FOV) is integrated, and a geometrical analysis is performed to calculate the flux at each LOS end point. The LOS collimator diameter is 1cm on each LOS.

Table 4.1 lists the expected neutron fluxes (in counts per second, cps) for each NCAM line of sight during the first three SPARC campaigns. Specifically, Campaign 1 will focus on DT operations with $Q > 1$ and a maximum expected fusion power of 12 MW. Campaign 2 is planned as a DD plasma campaign, while Campaign 3 targets the full-power scenario of 140 MW [60].

Table 4.1: Neutron fluxes for each NCAM line of sight (LOS). The table reports the DD and DT neutron flux per source rate, and the corresponding flux range ($n/m^2/s$) for the three SPARC campaigns.

LOS	DDn flux / source	DTn flux / source	Campaign 1 (DT)		Campaign 2 (DD)		Campaign 3 (DT)	
	$(1/m^2)$	$(1/m^2)$	Min	Max	Min	Max	Min	Max
1	3.05E−08	5.63E−08	3.36E+09	2.02E+11	5.70E+07	6.87E+09	1.44E+09	3.00E+12
2	2.22E−07	3.62E−07	2.16E+10	1.30E+12	4.13E+08	4.99E+10	9.29E+09	1.93E+13
3	8.91E−07	1.42E−06	8.46E+10	5.09E+12	1.66E+09	2.01E+11	3.64E+10	7.56E+13
4	2.64E−06	3.50E−06	2.09E+11	1.26E+13	4.92E+09	5.94E+11	8.99E+10	1.87E+14
5	4.55E−06	5.95E−06	3.55E+11	2.14E+13	8.50E+09	1.03E+12	1.53E+11	3.18E+14
6	5.30E−06	7.05E−06	4.20E+11	2.53E+13	9.89E+09	1.19E+12	1.81E+11	3.76E+14
7	4.63E−06	5.95E−06	3.55E+11	2.14E+13	8.64E+09	1.04E+12	1.53E+11	3.18E+14
8	2.45E−06	3.45E−06	2.06E+11	1.24E+13	4.57E+09	5.51E+11	8.85E+10	1.84E+14
9	9.38E−07	1.43E−06	8.54E+10	5.14E+12	1.75E+09	2.11E+11	3.67E+10	7.63E+13
10	2.41E−07	3.74E−07	2.23E+10	1.34E+12	4.49E+08	5.42E+10	9.60E+09	1.99E+13
11	3.28E−08	6.16E−08	3.68E+09	2.22E+11	6.12E+07	7.39E+09	1.58E+09	3.29E+12

Two type of SDD pixel are considered for the NCAM: large crystal ($4.5 \times 4.5 \times 0.5$ mm^3), and small crystal ($2.2 \times 2.2 \times 0.5$ mm^3). Their size is constrained by technology: CVD diamond thickness is limited to 500 μm, and lateral dimensions to ~ 5 mm to grow high-quality single crystals.
The expected counting rates for the two options are given in Figure 4.3, assuming an intrinsic detector efficiency of $5 \cdot 10^{-3}$, and including the diamond volume contribution corresponding to a $4.5 \times 4.5 \times 0.5$mm^3 SDD pixel.

A single diamond pixel cannot cover the full fusion power range from ~ 1 to ~ 140 MW. Large pixels provide sufficient statistics at low fluxes, but in the LOSs between 7 and 13, above 60 MW, exceed 1 MHz. This corresponds to a pile-up fraction above 5%,which is considered the maximum acceptable rate of operation for high resolution spectroscopy. Smaller pixels avoid saturation at high fluxes, yet their reduced volume yields insufficient statistics at low fluxes. Thus, a matrix configuration is required to cover the area of interest. Each LOS can combine the two types of crystals, enabling reliable T_i measurements across the full flux range.

The Poisson uncertainty related to the counting statistic is a key parameter in the choice of the NCAM set-up. A trade-off is made between low statistical uncertainties, pile-up minimization (avoid saturation), time resolution and number of channels optimization, since the diagnostic cost scale with the number of pixels employed. The relative standard

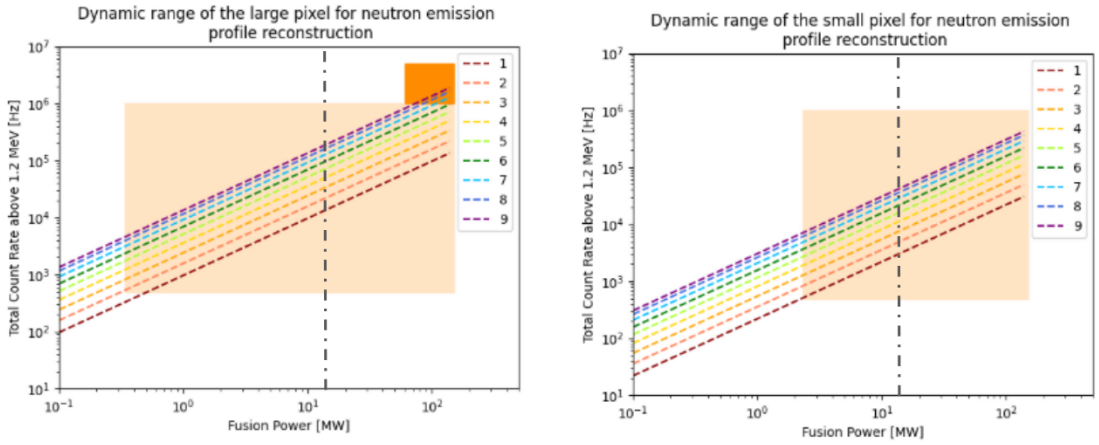

Figure 4.3: Expected neutron rates for large and small Diamond pixels along the NCAM LOSs for different fusion powers. The orange region corresponds to an operational regime that guarantee 500 counts per second per pixel. The dark orange region corresponds to a pile-up prone operational window. The vertical grey line corresponds approximately to P_{fus} = 12MW, i.e. the Campaign 1 and 2 maximum expected power. The colors correspond to different LOSs positions, from the outermost (1) to the centermost (9). The LOS expected counts are symmetrical around the central Line of Sight, number 10.

deviation of the measured emissivity and ion temperature are described by:

$$\sigma_\epsilon(P_{fus}) = \frac{1}{\sqrt{r_n(P_{fus}) \cdot \tau_r}} \tag{4.1}$$

$$\sigma_{T_i}(P_{fus}) = \frac{2}{\sqrt{2 \cdot r_{peak}(P_{fus}) \cdot \tau_r}} \tag{4.2}$$

Here, σ_ϵ represents the statistical uncertainty on the neutron count rate r_n, measured above threshold (1.2MeV) on the SDD pixel and multiplied for the time resolution τ_r. The ion temperature uncertainty σ_{T_i} is derived from error propagation of Equation 2.7, where $T_i = (\mathrm{FWHM}/177)^2$, and r_{peak} is the count rate under the Gaussian n-α peak, also normalized by τ_r. The dependence on P_{fus} reflects the scaling of neutron rates with fusion power, with r_{peak} being approximately twenty times lower than the total rate r_n, where precise values vary among the individual diamonds.

4.1.1 D4N Diamond Matrix

A compact 2×2 diamond matrix (D4N), combining two large and two small pixels, has been proposed in [65] for the SPARC neutron camera, providing the required dynamic range coverage with independent, redundant pixels optimized for neutron spectroscopy. The prototype, in Figure 4.4 features an Aluminum case that acts as Faraday cage and structural support. The aluminum casing has a 3mm diameter aperture in front of the matrix, to allow penetration of γ rays at the order of Mev for laboratory test calibration. The detector works with a ±400 V bias input Voltage, to allow for inversion

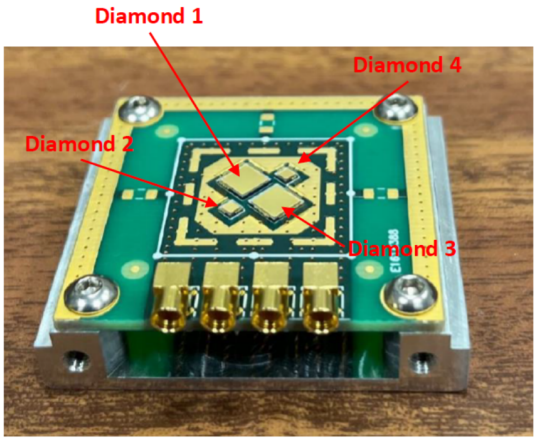

(a) Picture of the D4N prototype: the diamond pixels are gold-metallized and positioned onto the PCB board.

(b) Figure of the D4N within its Aluminum casing.

Figure 4.4: Pictures of the D4N prototype.

of polarity, to contrast polarization issues. The redundant configuration ensures that, for each line of sight, at least two pixels are operational under nominal counting rates, thereby preserving measurement reliability in case of a single-pixel malfunction, on top of increasing the counting statistic. With this detector matrix the trade-off between time resolution and Poisson uncertainty can be summarized in Figure 4.5.

The prototype is tested at the Frascati Neutron Generator (FNG-ENEA), with a 14.1 MeV DT source. Neutrons are generated through the D(T, ^{4}He)n fusion reaction between the 250 keV accelerated deuterium beam and the tritium implanted in the target [66]. Each detector was coupled to a CIVIDEC C6 preamplifier via a 12.5 cm cable, and the resulting signals were sent to a CAEN DT5730 digitizer (14-bit, 500 MS/s) for simultaneous digital acquisition of pulse amplitude and arrival time. The set-up is shown in Figure 4.6. The pulse amplitude data are subsequently processed offline to reconstruct the pulse height spectra of the four independent detectors, shown in Figure 4.7.

The detector position selected for this experiment, at 90 degree from the Beam direction, was chosen to minimize the broadening of the neutron beam spectrum given by the Deuterium kinematics, which is fixed at 130 keV. The broadening of the measured peak ($\mathrm{FWHM_M}$) can be used to determine the intrinsic detector energy resolution ($\mathrm{FWHM_R}$) via the relation:

$$\mathrm{FWHM_M} = \sqrt{\mathrm{FWHM_R^2} + \mathrm{FWHM_{beam}^2}},$$

where $\mathrm{FWHM_{beam}}$ represents the contribution from the neutron beam. Table 4.2 reports the $\mathrm{FWHM_M}$ values of the four n-α peaks for each detector. Assuming a beam broadening of approximately 130 keV, these results confirm the high quality of the diamond crystals, with an achievable resolution on the order of 1.3% at 14.1 MeV.

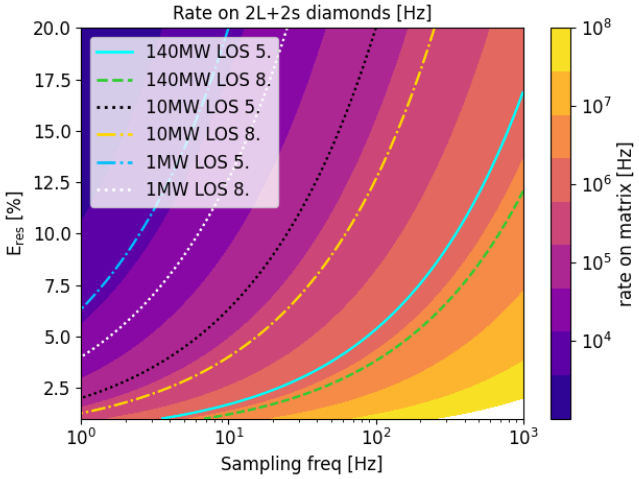

Figure 4.5: Trade-off between T_i sampling frequency and associated Poisson uncertainty on the T_i measurements associated to different neutron rates on the D4N detector, with examples of different LOSs and plasma scenarios.

Figure 4.6: Experimental set-up at the FNG DT neutron source, for the characterization of the D4N diamond matrix.

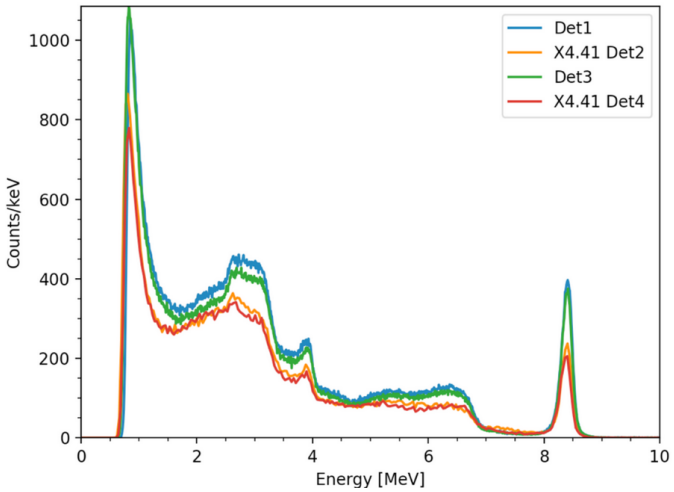

Figure 4.7: Pulse height spectra of the four SDD at the FNG DT beam. The pulse height spectra of the smaller diamonds have been multiplied by 4.41 which is the ratio of the large-small crystals active area.

Table 4.2: Energy resolution of the four pixels. The energy resolution E_{res} is calculated as $E_{res} = FWHM_R/14.1MeV$.

Pixel	$FWHM_M$ [keV]	E_{res}
1	222	1.28%
2	219	1.27%
3	220	1.27%
4	230	1.35%

4.2 Synthetic data production and inversion algorithm development

The production of synthetic data for the NCAM detector follows the same workflow used to estimate the neutron flux, with the addition of energy information. The starting point is the reference 140 MW full power scenario. The known quantities are the magnetic equilibrium surfaces and the radial profiles of density and T_i, which are combined to obtain $T_i(R, Z)$ and $\epsilon(R, Z)$ on a poloidal surface defined over a 40×70 grid.
The detectors measure line-integrated emissivity and effective temperature, calculated as weighted averages along the line of sight (LOS) of each detector:

$$\epsilon_{\text{eff},i} = \frac{\int_{\text{LOS}i} \epsilon(R,Z) \cdot G_i(R,Z) dV}{\int_{\text{LOS}i} \cdot G_i(R,Z) dV} \tag{4.3}$$

$$T\text{eff}, i = \frac{\int_{\text{LOS}i} T_i(R,Z) \cdot \epsilon(R,Z) \cdot G_i(R,Z) dV}{\int_{\text{LOS}i} \epsilon(R,Z) \cdot G_i(R,Z) dV} \tag{4.4}$$

where $G_i(R, Z)$ is the geometrical transport matrix. This matrix is computed with the Revolt routine using a voxel grid of 1600×2800 points. The LOS geometry is modeled as a straight cylinder, starting 14.5m from the tokamak center, long 2.5m with a 1 cm diameter. The simulated detector consists of 19 circular pixels, each 1 cm in diameter, positioned at the LOS endpoints. Under this assumption, the SDDs occupy the entire available detector area in the simulation. Depending on the number of SDDs employed, the final counts are normalized to the ratio of the effective area to the total, assuming perfect alignment of SDDs within the LOS. The number of SDDs affects only the Poisson uncertainty, while T_i (and ϵ) measurements, and therefore T_{eff} (and ϵ_{eff}), remain unchanged. A full neutronic model is excluded from this work since the aim is to optimize the NCAM for ion temperature estimation. Such modeling, along with an accurate detector calibration, would instead be required for fusion power estimation using the NCAM, which is an interesting future development, based on the emissivity estimation, to further exploit the capability of the diagnostic.
While Equation 4.3 represents a straightforward weighted sum of counts, the validity of Equation 4.4 is not as trivial. However, as discussed in [46], the recorded spectrum is a superposition of local spectra from plasma regions with different temperatures, convoluted with the detector response. Since the neutron energy information is embedded in a Gaussian broadening, and the detector response, in the region of interest, is also Gaussian, the assumption in Equation 4.4 holds for T_i estimation.
The reference T_i and emission profiles are parameterized using analytic forms appropriate for thermal plasmas [46]:

$$\epsilon(r) = \epsilon_0 \left(1 - \left(\frac{r}{a}\right)^2\right)^{\beta} + \epsilon_{\text{offset}} \tag{4.5}$$

$$T_i(r) = T_{i0} \left(1 - \left(\frac{r}{a}\right)^2\right)^{\alpha} + T_{\text{offset}} \tag{4.6}$$

Here, r/a is the normalized radius obtained from EFIT equilibrium. The parameters α and β control the radial gradients, while ϵ_0 and T_{i0} set the central values of emissivity and temperature, excluding the offsets. The offset terms account for unmodelled pedestal effects. This parameterization is a key assumption both for profile inversion and for simulating profile variability, where α and β are perturbed and plasma positions are shifted by up to ±15 cm, as discussed in Section 4.2.1. A visualization of the synthetic data production is shown in Figure 4.8.

4.2.1 Profile inversion routine

The profile reconstruction routine adopts a weighted least-squares approach to fit the synthetic line-integrated profiles of ϵ_{eff} and T_{eff}. The independent variable is the line-of-sight (LOS) index, while the dependent variables are the LOS-integrated ion temperature and neutron emissivity, with weights given by the inverse Poisson variance of each measurement. The fitting function is the forward model previously described, assuming that the magnetic profile is already known. The free parameters correspond to those defined in the $\text{T}_\text{i}(\text{r/a})$ $\epsilon(\text{r/a})$ Equations 4.5 and 4.6, which are used within the forward model: Equations 4.3 and 4.4.
The reconstruction procedure is divided into two steps:

- **Neutron emissivity fit:** in the first step, the routine fits the neutron rate data (Equation 4.3) to reconstruct the emissivity profile, allowing the estimation of the parameters in Equation 4.5.
- **Ion temperature fit:** in the second step, the parameters obtained from the emissivity fit are held fixed, and a fit is performed on the ion temperature profile using Equation 4.4. The remaining free parameters, defined in Equation 4.6, are optimized in this stage.

The reconstructed T_i profile is then evaluated from Equation 4.6 across the normalized radial coordinate r/a. The accuracy of the reconstruction along this coordinate is assessed as described in Section 4.2.2.
It is important to note that, since the NCAM detector features only a vertical array, a full tomographic reconstruction cannot be performed without assumptions. In this work, the magnetic equilibrium is used to compensate for the absence of a second projection. This approach assumes that the plasma position and shape are known from EFIT reconstructions. The information comes into play when projecting T_i and ϵ on the (R, Z) space. While this assumption is valid for inter-shot analysis, future real-time control applications may require alternative strategies, such as directly feeding into the control system the raw T_{eff} and ϵ_{eff} data.
Figure 4.9 illustrates the workflow of the inversion procedure. The upper panels show the synthetic detected emissivity and Temperature profiles generated from the reference plasma scenario, including the effects of plasma shifts and Gaussian noise. The lower panel presents an example of reconstructed (r/a) profiles, compared with the corresponding input profiles used to generate the synthetic data.

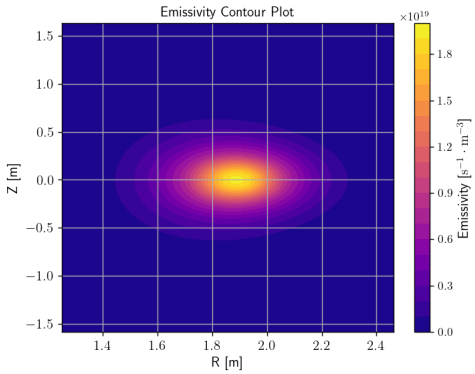

(a) Emissivity map $\epsilon(R, Z)$ on the reference poloidal grid.

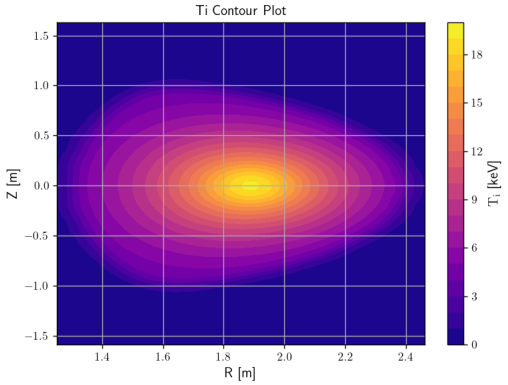

(b) Ion temperature map $\mathrm{T_i}(R, Z)$ obtained from interpolated profiles.

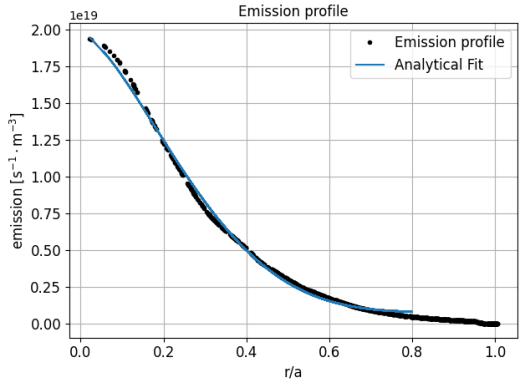

(c) Radial emissivity profile fitted with Equation 4.5.

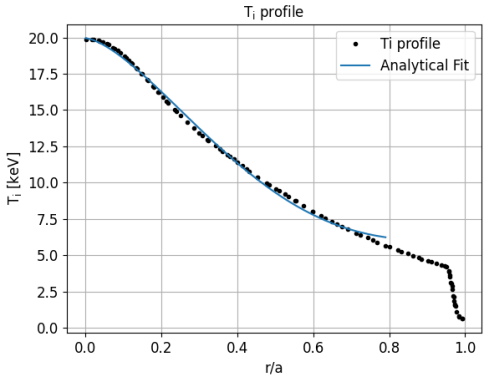

(d) Radial ion temperature profile fitted with Equation 4.6.

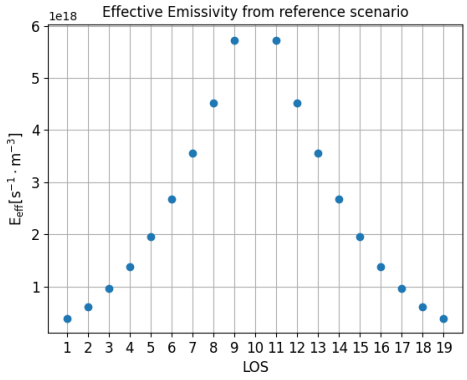

(e) Line-integrated emissivity $\epsilon_{\mathrm{eff},i}$ computed along detector LOS. The corresponding error bars, derived from Equation 4.1 are smaller thant the points.

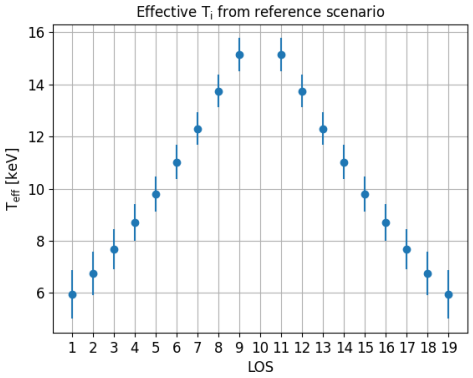

(f) Effective ion temperature $\mathrm{T_{eff}, i}$ derived from Equation 4.4, with corresponding Poisson error bars, derived from Equation 4.2.

Figure 4.8: Synthetic data generation workflow. From the reference profiles, $\epsilon(R, Z)$ and $\mathrm{T_i}(R, Z)$ are obtained, the profile are parametrized, and integrated along detector lines of sight to compute $\epsilon_{\mathrm{eff},i}$ and $\mathrm{T_{eff}, i}$.

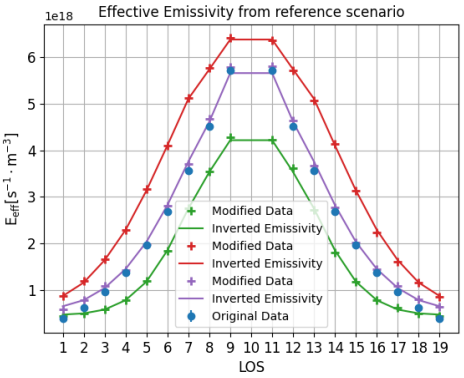

(a) Example of synthetic effective Emission on the NCAM.

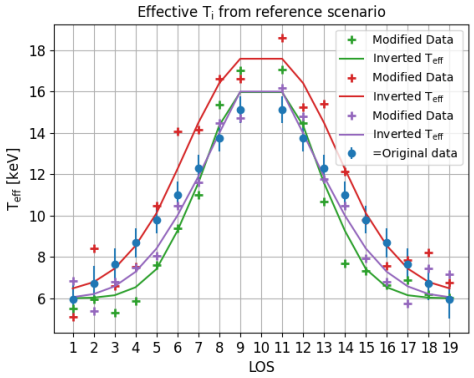

(b) Example of synthetic effective Ion Temperature on the NCAM.

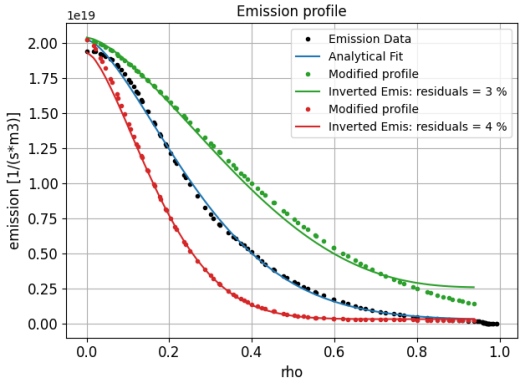

(c) Example of Emission profile reconstruction.

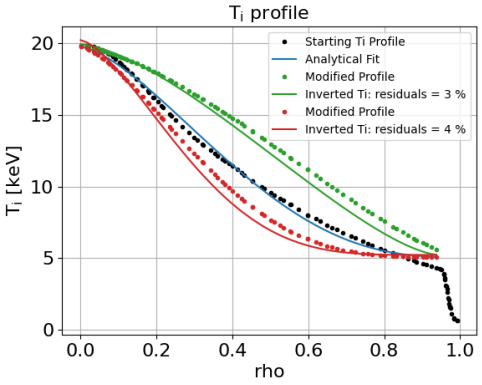

(d) Example of Ion Temperature profile reconstruction.

Figure 4.9: Illustrations of the synthetic inversion process. On the first row: examples of synthetic effective measurements on the NCAM. The blue points correspond to the reference SPARC scenario, while the other points represents data produced with stochastically varied parameters, and the respective fit lines. On the second line: examples of profile reconstruction. The black line shows the baseline profile, while the dotted colored curves represent modified synthetic profiles. The corresponding reconstructed profiles are shown as solid lines, along with their average residuals.

4.2.2 Performance evaluation

The performance analysis focuses on the average residuals of the reconstructed ion temperature profile. For each profile reconstruction, the average residual is computed over all points along the normalized radial coordinate r/a:

$$\langle \delta T_i \rangle \ [\%] = \left\langle \left| \frac{T_{i,\mathrm{true}}(r/a) - T_{i,\mathrm{rec}}(r/a)}{T_{i,\mathrm{true}}(r/a)} \right| \right\rangle \times 100 \tag{4.7}$$

where $\mathrm{T_{i,true}}(r/a)$ is the input ion temperature at point r/a, and $T_{\mathrm{i,rec}}(r/a)$ is the corresponding reconstructed value. The same figure of merit is evaluated for the emissivity profile.
A statistical distribution of average residuals is obtained by repeating the synthetic data generation and reconstruction process N=1000 times, each with independently varied synthetic measurement inputs. In each iteration, three stochastic perturbations are applied to the baseline $\mathrm{P_{fus}}$=140 MW scenario:

- **Profile shape variation:** the shape of the ion temperature and neutron emissivity profiles is varied heuristically by scaling the parameters α and β (Equations 4.5-4.6) by a random factor uniformly drawn from (1.0,1.2,1.4,...,3.0), or their reciprocals (1/1.2,1/1.4,...,1/3.0). This produces broaden or makes the profile more peaked, respectively. This approach is not physically consistent with simulated plasma scenarios and is adopted solely to test the robustness of the inversion, given the current lack of multiple plasma scenarios, which will be available and analyzed in future optimization steps. The same reasoning apply to the plasma position shifts at the next point.

- **Plasma position shift:** the robustness of the reconstruction is tested against random vertical and horizontal plasma displacements up to ±0.15 m (tokamak minor radius a = 0.57m), obtained by shifting the magnetic equilibrium matrix along the poloidal (R,Z) plane. These shifts are assumed to be reconstructed by the EFIT routine.

- **Measurement noise:** Gaussian noise is added to the line-integrated profiles $\mathrm{T_{eff}}$ and ϵ_{eff}, with standard deviations defined by Eqs. 4.1 and 4.2.

Different NCAM configurations can be compared on the base of the performance of the inversion algorithm with the chosen configuration. An example of the statistical distribution of the average residual for a given set-up is shown in Figure 4.10.

4.3 Design Optimization

This section explores the performances of the key options for the NCAM setup. Two key parameters are considered: the number of LOSs to be populated and the number of detectors deployed along each LOS. The NCAM can serve multiple purposes, for instance, central LOS are preferable for $\mathrm{T_i}$ and neutron emissivity estimation, whereas studying

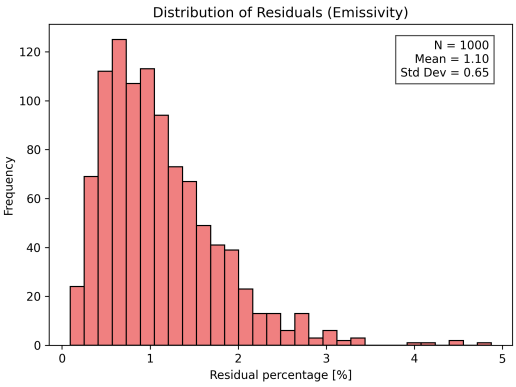

(a) Emissivity profile-averaged residuals distribution.

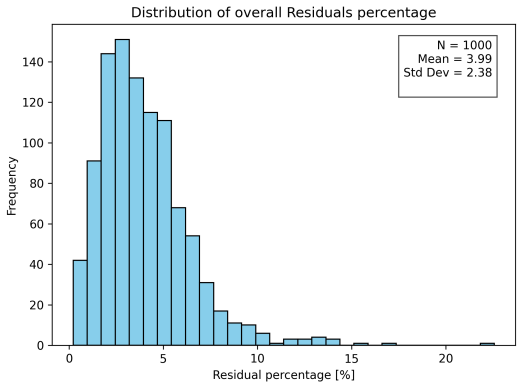

(b) Ion Temperature profile-averaged residuals distribution.

Figure 4.10: Example of the statistical distribution of the profile-averaged residuals of the reconstructed quantities, for a scenario of P_{fus} = 10MW, time resolution of 100 ms, exploiting 7 LOSs equipped with 1 Large and 1 small SDD each.

the plasma edge or alpha particle physics benefits from populating the outer LOS. In this analysis, only T_i and emissivity estimation are considered, as these represent the primary performance targets identified for the current stage of the system development.

Regarding the combination of SDD pixels, three main configurations are selected: 1 large + 1 small pixel (1L+1S), 2 large pixels (2L), and the 2 large + 2 small pixel matrix (D4n). Single pixels were excluded due to insufficient statistics and lack of redundancy, while double small pixels were discarded because they would not provide adequate counting statistics during low-power operation phases. Using a larger number of diamonds would result in an overly expensive NCAM design, as the cost scales with the number of pixels.

The statistical uncertainty of measurements along each LOS is a key factor in prioritizing which LOS to populate. Figures 4.11 summarize the statistical uncertainty for each LOS under scenarios with P_{fus} = 1, 10 MW, which are used as the main study cases. It is important to note that in this analysis the scenarios differ only in terms of Poisson-related measurement uncertainty and not in plasma shape parameters. The analysis focuses on these low-power scenarios because they represent the critical operational limit. Time resolution of 4, 10, and 100 Hz were analyzed, corresponding respectively to the CFS minimum required time resolution, the target resolution, and the optimal case for real-time control applications.

Once the number of pixels on each LOS is fixed, different LOS configurations can be evaluated. Table 4.3 summarizes some representative options. For each case, the configuration that minimises the average residual is selected as the optimal one. For configurations with a small number of LOS (5 or 6), the analysis is restricted to geometries that prioritise central LOSs, as these provide the highest sensitivity to the core parameters of interest. When the total number of LOS increases, the number of distinct configurations that require examination naturally decreases, since most viable arrangements still favour

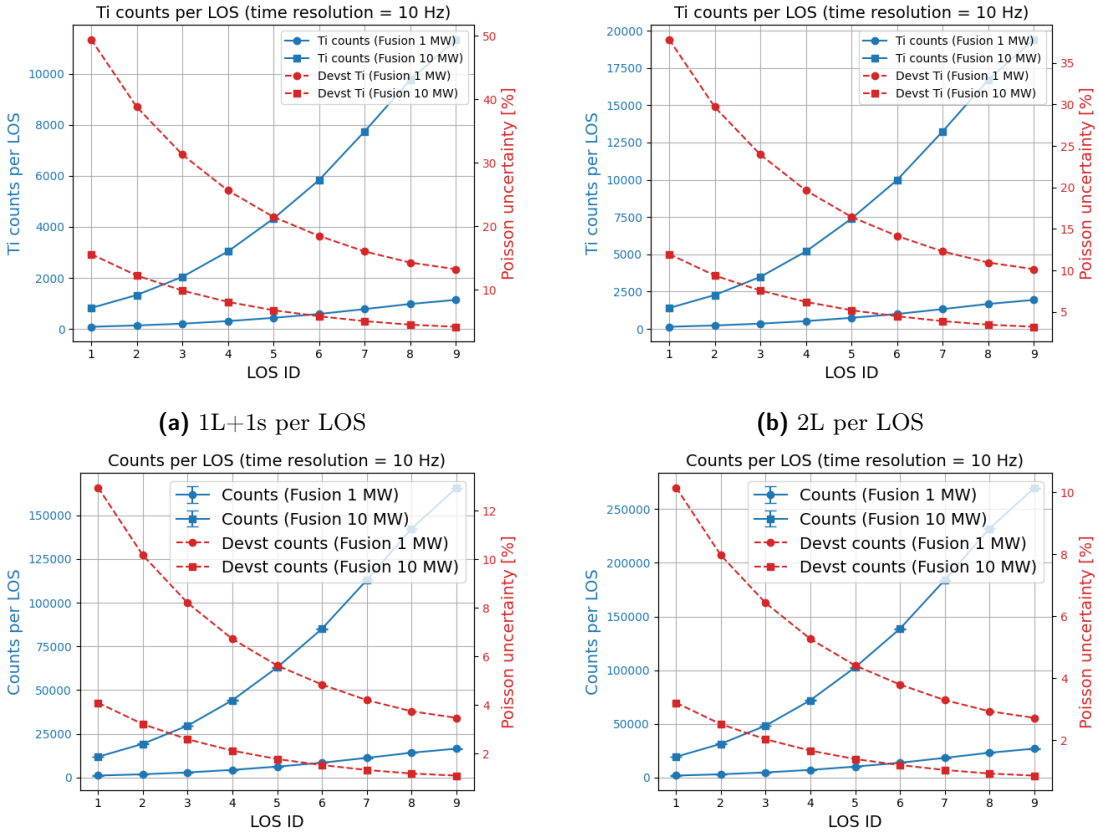

(a) 1L+1s per LOS

(b) 2L per LOS

(c) 1L+1s per LOS

(d) 2L per LOS

Figure 4.11: Statistical limitations for two detector configurations: 1L+1s pixels (left column) and 2L pixels (right column), evaluated for both measured ion temperature (first line) and emissivity (second line).

Config.	#LOS	1	2	3	4	5	6	7	8	9	10	11	12	13	14	15	16	17	18	19
a	5					X		X		X		X		X						
b	6					X		X		X		X		X		X				
c	7		X		X			X		X		X		X			X			
d	7		X			X		X		X		X		X			X			
e	7			X		X		X					X		X		X		X	
f	7		X			X		X		X		X		X		X				
g	8		X			X		X		X		X		X		X		X		
h	8			X		X		X		X		X		X		X		X		
i	8			X		X		X		X			X		X		X		X	
l	8		X		X		X		X			X		X		X		X		
m	9		X			X		X		X		X	X		X		X		X	
n	9		X			X		X	X	X		X		X		X		X		
o	9	X		X		X		X		X		X		X		X		X		
p	9		X			X		X	X			X	X	X		X			X	
q	9		X		X		X		X	X		X	X		X		X			
r	9		X		X		X		X			X		X		X	X		X	
s	10		X			X		X	X	X		X	X		X		X		X	
t	10	X		X		X		X		X		X		X		X		X		X
u	12				X	X	X	X	X	X		X	X	X	X	X	X			
v	12			X		X	X	X	X	X		X		X		X	X	X	X	
w	16		X	X	X	X	X	X	X	X		X	X	X	X	X	X	X		
all	18	X	X	X	X	X	X	X	X	X		X	X	X	X	X	X	X	X	

Table 4.3: Configurations sorted by increasing number of LOS. Each X marks the utilization of that LOS; a thicker line separates groups with different LOS counts.The best LOS configurations for each LOS number are highlighted in gray.

central coverage; for instance, with 16 LOS only the two outermost LOS are omitted. Intermediate cases (e.g., 9 LOS) allow for different strategies, such as alternating LOS placement or enhancing central coverage while excluding the extreme periphery. For moderate LOS counts, the space of possible configurations becomes rich, but the study focuses on those that are most relevant for assessing core-diagnostic performance.

Figure 4.12 illustrates the residual comparison for nine LOS configurations at 100 Hz, for P_{fus} = 1 and 10 MW, using a D4n pixel matrix in the central LOS (LOS between 7 and 13) and 2L pixels on the outermost LOSs. The error bars in the plots indicate the 16th and 84th percentiles of the distribution, corresponding to a 68% confidence interval around the median, providing a robust, non-parametric estimate of measurement uncertainty. Overall, the differences observed across the tested configurations are relatively small and remain well within these uncertainties. This might be due to the fact that the present analysis is based on a single operational scenario, complemented only by a set of heuristic variations. A broader set of scenarios would likely reveal more pronounced trends and offer a deeper comparison and will be explored in future analyses.

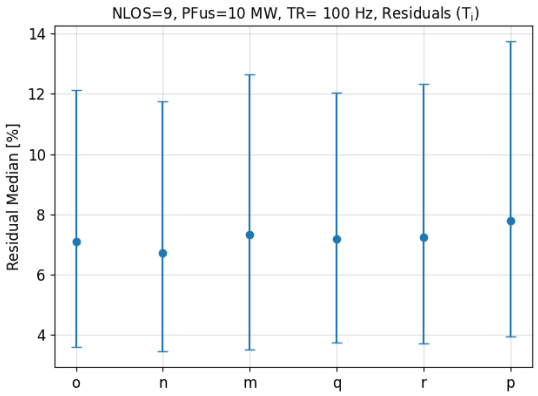

Figure 4.12: Comparison of the inversion algorithm performance for different configurations with 9 LOS (names corresponding to configuration in Table 4.3), at 10MW, 100 Hz, using D4n pixels in central LOS and 2L pixels in the outermost LOS.

After selecting the optimal combination of LOS for each exploited LOS number, the average residuals are plotted to illustrate how increasing the number of LOS improves performance. Figures 4.13 present the impact of adding more lines of sight for the 1L+1s configuration on each LOS, which serves as the baseline setup. This analysis shows that within the model assumptions the emission profile estimation is not the critical parameter, because all the configurations, exploiting more than 6 LOSs, satisfy the requirement of overall uncertainty below 10% even at 100Hz and P_{fus} = 1MW. However the requirement regarding the T_i, at 10Hz is not satisfied in any configuration for $P_{fus} \sim$ 1MW.

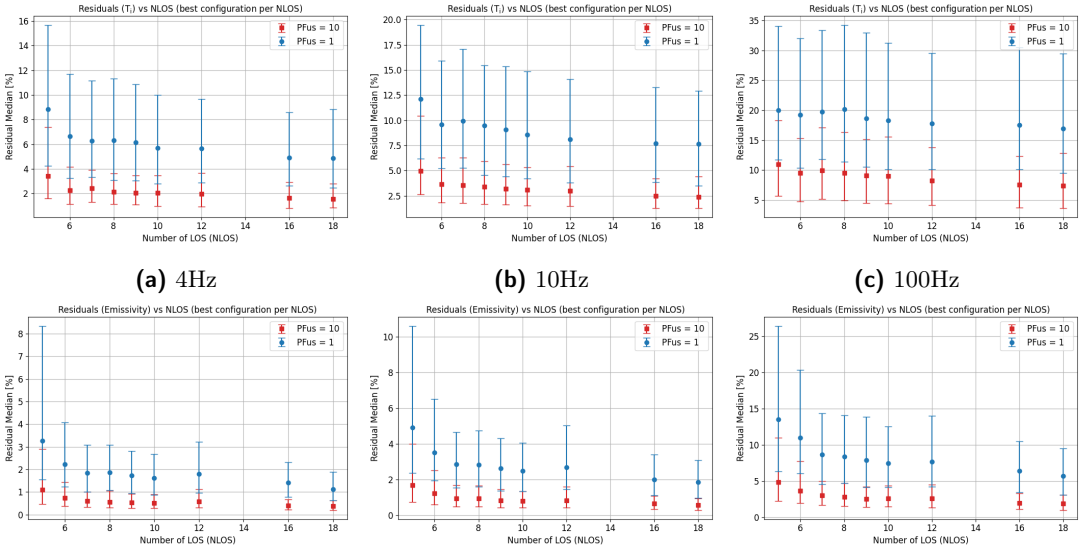

(a) 4Hz **(b)** 10Hz **(c)** 100Hz

(d) 4Hz **(e)** 10Hz **(f)** 100Hz

Figure 4.13: Residuals of reconstructed T_i on the first line, and Emission profile on the second line, for the optimal set-up of different number of LOS occupation, with 1L+1s configuration on each LOS for different time resolution.

To enhance statistics, the outer LOS (defined as < 7 or > 13) can be equipped with 2L pixels, while the central LOS retain the 1L+1s configuration to prevent pile-up on both SDDs at $P_{fus} > 60$MW (see Figure 4.3). A more comprehensive solution, which ensures redundancy across all LOS under any tokamak operating condition, and further enhance the statistic on the LOSs involves installing the D4n matrix on the central lines and 2 large SDDs on the outermost LOSs. The group of Figures 4.14 and 4.15 instead compare the performance of the 3 pixel configurations at 10Hz and 100Hz respectively.

In particular this highlights that the usage of all the LOSs does not add enough information, but an improvement statistic uncertainty in the central LOSs achieve better performances.

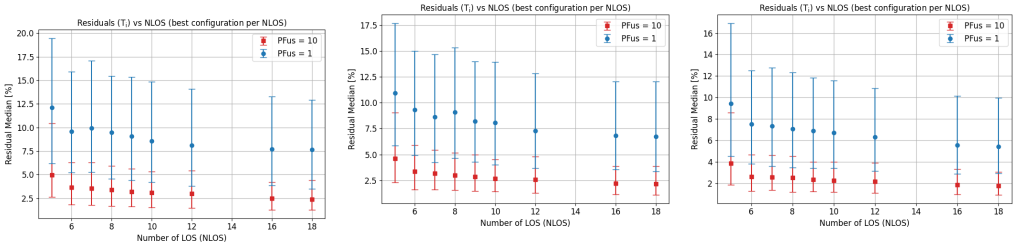

(a) 1L1s on every LOS

(b) 1L1s on central LOSs, 2L on the outer LOSs

(c) D4n on central LOSs, 2L on the outer LOSs

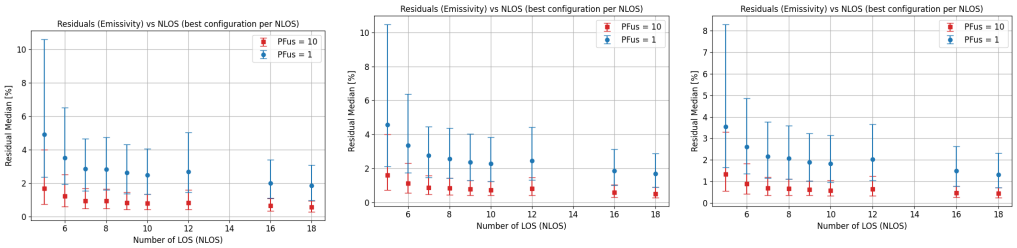

(d) 1L1s on every LOS

(e) 1L1s on central LOSs, 2L on the outer LOSs

(f) D4n on central LOSs, 2L on the outer LOSs

Figure 4.14: Residuals of reconstructed T_i on the first line, and Emission profile on the second line, for the optimal set-ups of different number of LOS occupation, with different pixel configurations on each LOS for 100ms time resolution.

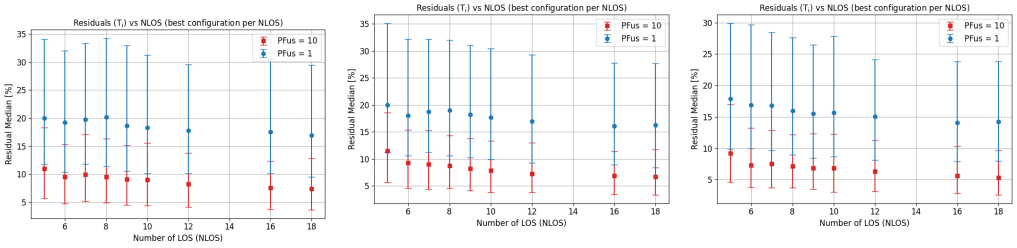

(a) 1L1s on every LOS

(b) 1L1s on central LOSs, 2L on the outer LOSs

(c) D4n on central LOSs, 2L on the outer LOSs

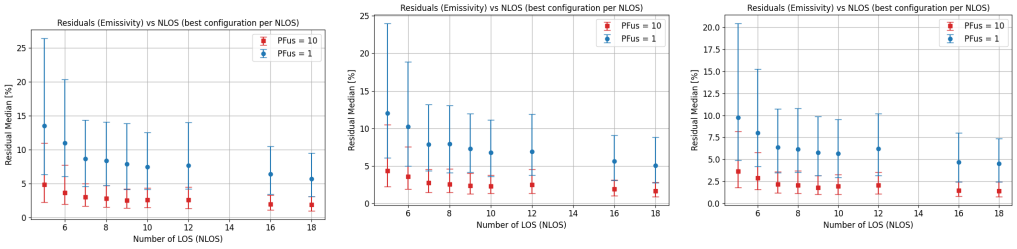

(d) 1L1s on every LOS

(e) 1L1s on central LOSs, 2L on the outer LOSs

(f) D4n on central LOSs, 2L on the outer LOSs

Figure 4.15: Residuals of reconstructed T_i on the first line, and Emission profile on the second line, for the optimal set-ups of different number of LOS occupation, with different pixel configurations on each LOS for 10ms time resolution.

4.3.1 Conclusions

The analysis presented in this section provides several important insights:

- A method was developed to reconstruct the plasma ion temperature (T_i) and emissivity (ϵ) profiles using the NCAM-measured quantities T_{eff} and ϵ_{eff}, combined with magnetic reconstruction profiles and assuming a Maxwellian plasma. This method can be applied in future design optimization studies across different plasma scenarios and for offline data analysis during operation.

- For emissivity measurements alone, any setup with more than 5 lines of sight (LOS) performs adequately up to a time resolution of 100Hz, even using the baseline 1L+1s detector configuration (see Figure 4.15).

- Small diamond detectors are only necessary for fusion powers above 60 MW (Campaign 3), as indicated by Figure 4.3. Consequently, a proposed design intended exclusively for the first two SPARC campaigns, which are expected to reach a maximum fusion power of 12 MW, can employ large pixels on all LOS.

- At 100Hz time resolution and P_{fus} = 1MW, the reconstruction of T_i is inadequate for all current configurations. Thus the operational limit is around 10Hz. The most promising viable solution is to increase the number of diamond detectors beyond the D4n set-up. One potential approach is to align multiple diamonds on different layers, with the downside of possible cross-talk between the pixels, and complications for in-situ α calibration; further studies will investigate this option.

- A target time resolution of 10Hz is achievable at 1MW $\geq P_{fus} \geq$ 140MW . Since increasing the number of LOS beyond 9 provides minimal improvement, while fewer than 9 LOS noticeably degrades performance, a design with 9 LOS is a reasonable choice, which can be upgraded in later machine phases by adding pixels or populating more LOSs. This can be implemented using either the 2 large pixels detector or a configuration with the D4n matrix in the center and 2L at the edges. Since the analysis of different LOS configurations did not reveal any particularly favorable option (the differences in the average residuals in Figure 4.12 lie within the error bars), an evenly distributed set of LOSs is recommended to maintain symmetry and ensure homogeneous coverage of both the core and edge. The optimal design is summarized in Table 4.4.

LOS ID	**1**	**2**	**3**	**4**	**5**	**6**	**7**	**8**	**9**	**10**	**11**	**12**	**13**	**14**	**15**	**16**	**17**	**18**	**19**
	2L		2L		2L		2L		2L	/ /	2L		2L		2L		2L		
	2L		2L		2L		2L+2s		2L+2s	/ /	2L+2s		2L+2s		2L		2L		

Table 4.4: LOS Design of Minimum Viable Product selected. The first line indicates the pixel choice optimized for the first campaign, while second line indicates the pixel choice optimized for the entire SPARC lifecycle.

Chapter 5

Assessment of GEM detector as SXR diagnostic for spherical tokamaks

This chapter presents the results obtained with the GEM-based soft X-ray diagnostic on the MAST-U spherical tokamak. It first describes the installation and integration of the detector into the machine (Section 5.1). The first analysis of the experimental data is then discussed (Section 5.2), followed by a comparison with the predictions of the Revolt synthetic diagnostic (Section 5.2.3). Data-analysis approaches to perform tomographic reconstruction and electron temperature estimation, are introduced in Section 5.3. The study of neutron background affecting the diagnostic is illustrated in Section 5.5.

5.1 GEM diagnostic installation on MAST-U

A GEM detector was installed as a compact SXR camera on a spherical tokamak for the first time on MAST-U in November 2023, operating during the final three months of the MU3 experimental campaign [67]. The detector is a standard triple GEM, described in [39] and schematically shown in Figure 5.1a. It features three aluminized GEM foils and a copper anode segmented into a 16×16 array of 6×6 mm^2 pads (Figure 5.1b). The detector operates with a controlled flow of the standard Ar–CO_2 (70–30%) gas mixture. The cathode consists of an aluminized Mylar foil (12 μm thick). In front of it, a 4 mm ga, terminating in a Kapton window prevents direct exposure of the cathode to ambient air. This gap is filled with the same Ar–CO_2 gas mixture. The Drift, Transfer, and Induction gaps are $4, 1, 2, 1$ mm, respectively. The readout is based on the GEMINI system (Figure 5.2). The detector was characterized and calibrated at the ISTP laboratories in Milan following the procedure described in Appendix A.

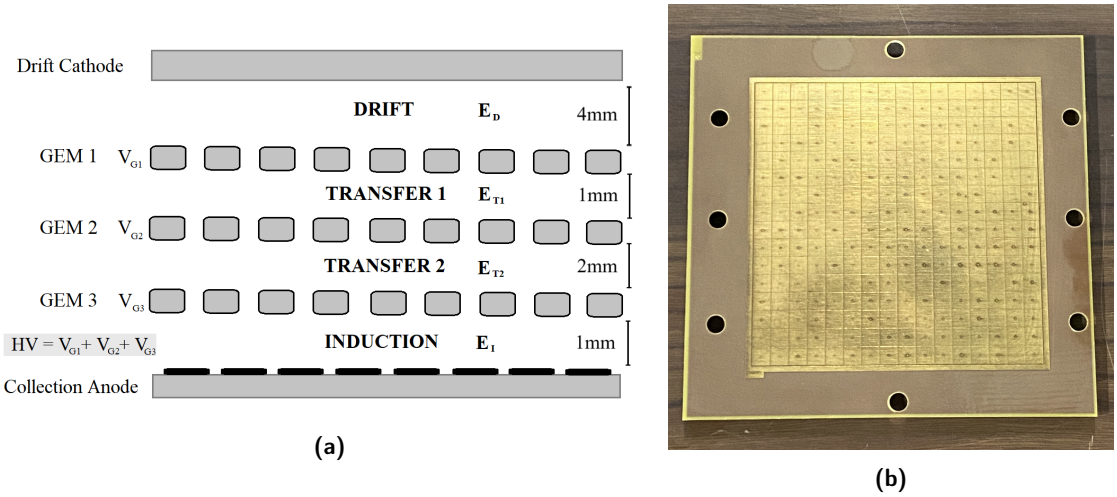

Figure 5.1: (a) Schematic of the triple-GEM detector. (b) Picture of the 16×16 pixel detector anode. From [39].

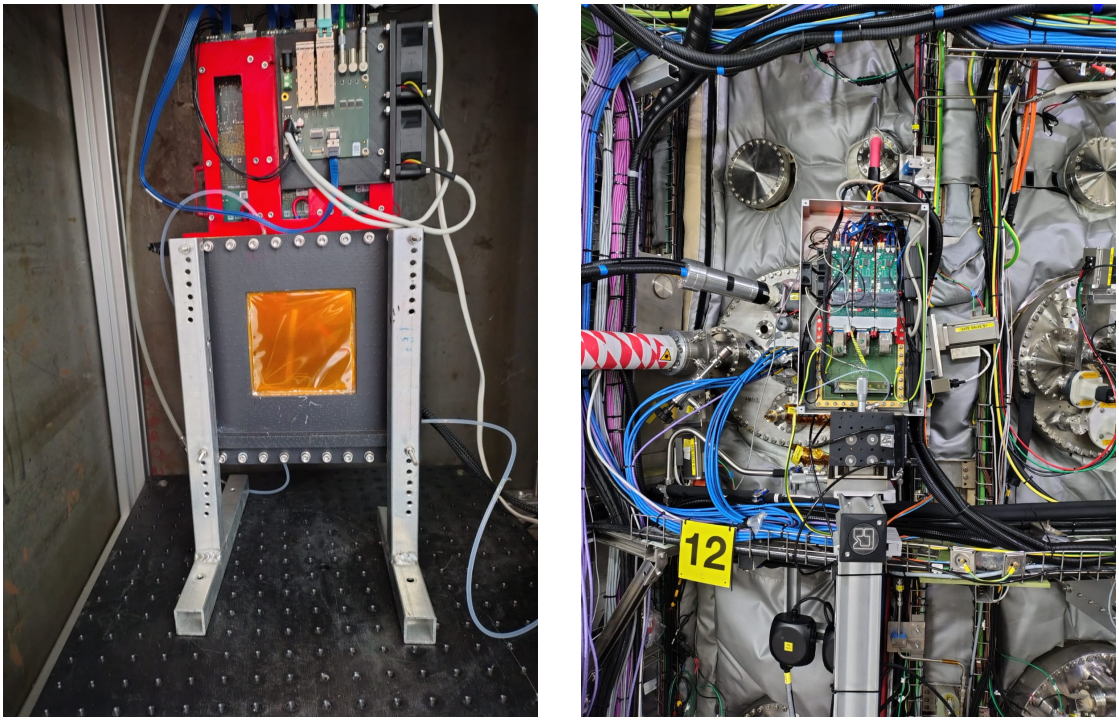

Figure 5.2: Front and back view of the GEM diagnostic installed on MAST-U, showing the readout electronics connected to the detector, housed in an aluminum casing.

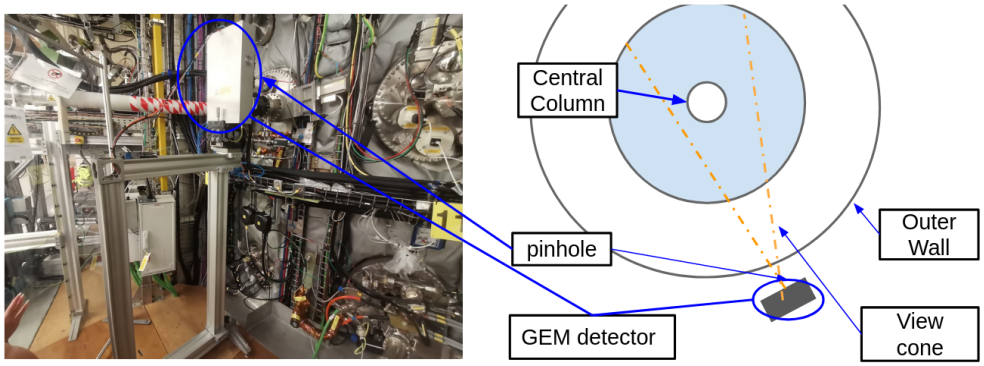

Figure 5.3: Left: GEM detector in its protective case installed on MAST-U. Right: top view of the GEM setup on MAST-U.

5.1.1 Experimental setup

The detector is installed as a pinhole camera in the MAST-U tokamak hall, positioned outside the vacuum vessel on the equatorial plane outside port in a radial configuration, as shown in Figure 5.3. It is enclosed in an aluminum case that serves as both electromagnetic interference (EMI) shielding and mechanical protection. The system is mounted on a mechanical support allowing manual radial position adjustments of up to ±20 cm, effectively varying the field of view.
The pinhole consists of a commercial beryllium window (25 μm thick, 13 mm diameter) mounted on a CF40DN flange 2.4 m from the tokamak center on the mid-plane. This window serves as the vacuum–air interface and was selected for its mechanical strength and SXR transparency, with a low-energy cut-off around 1 keV. A gate valve installed before the pinhole provides an additional vacuum barrier and is routinely opened a few seconds before each plasma pulse. The detector is placed 30 cm behind the beryllium window, corresponding to 2.7 m from the tokamak center, this result in a undesired low energy filter, discussed later in the chapter. A telescopic plastic tube (12 cm diameter, 2 mm thick) connects the pinhole to the detector to protect both the beryllium and Kapton windows from accidental impacts. A vertical section of the setup is shown in Figure 5.4, and the CAD model of the complete assembly is shown in Figure 5.5. The materials of the main components are listed in Table 5.1, while Table 5.2 summarizes the materials encountered by photons along the SXR path.
The GEM system is remotely controlled via a fiber-optic connection linking a PC in the control room to a cubicle located about one meter from the detector, housing the high-voltage (HV) module. The same PC manages GEM voltages and data acquisition from the FPGA-based readout system.
The HVGEM module is a high-voltage power supply that provides seven fully isolated channels, each equipped with a high-sensitivity current meter capable of detecting discharges, and includes programmable current protection [69].

The GEM detector bidimensional structure, exploited with a radial point of view allows

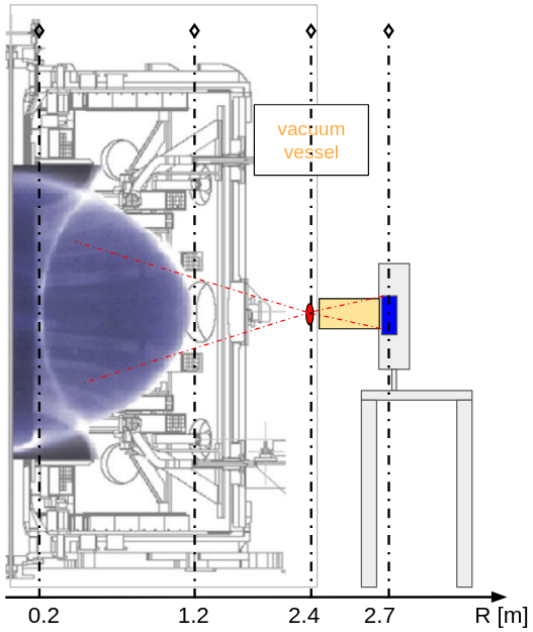

Figure 5.4: Vertical section of the GEM diagnostic installation on MAST-U. The GEM integration scheme is overlaid on the MAST-U schematic from [68], showing a typical plasma cross-section. The detector (blue rectangle) is enclosed in its EMI shielding case. A telescopic plastic protection (the yellow rectangle) for the GEM cathode and beryllium windows (red ellipse, not to scale). The camera view cone is marked by red dashed lines, while vertical dashed lines indicate the radial positions of the central column, first wall, vacuum vessel, and GEM detector.

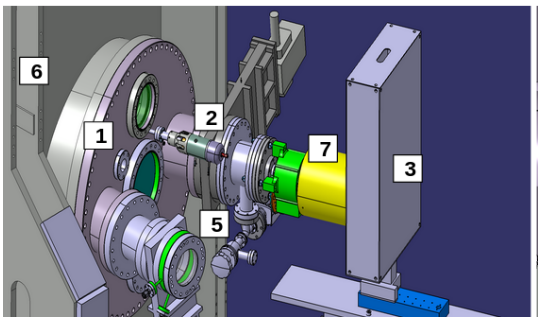

(a) CAD model view.

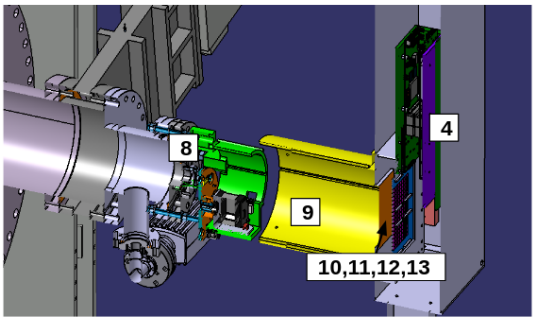

(b) Section of the CAD model.

Figure 5.5: CAD model of the GEM diagnostic integrated on MAST-U. Labels identify the main components of the setup, described in Tables 5.1 and 5.2.

Surrounding Element	Material	Label
Tokamak flange	Stainless steel	1
GEM port: CF40DN flange	Stainless steel	2
GEM EMI box	Aluminum	3
Detector structure	FR4	4
Valve supports	Stainless steel	5
Vacuum chamber wall	Stainless steel	6
Protection	Plastic (PLA)	7

Table 5.1: Main components of the experimental setup contributing to neutron-related background, with materials and corresponding labels as shown in Figure 5.5.

SXR Path Element	Thickness	Label
Plasma	1.2 m	
Vacuum	1.2 m	
Beryllium window	25 μm	8
Air	$\sim$ 30 cm	9
Aluminized Mylar window	12.5 μm	10
$ArCO_2$	6mm in MU3, 1.8 mm in MU4	11
Aluminized Mylar cathode	12.5 μm	12
$ArCO_2$ detector volume	4 mm in MU3, 5 mm in MU4	13

Table 5.2: Materials traversed by photons along the SXR path, from the plasma source to the detector sensitive volume. For parameters that differ between the MU3 and MU4 campaigns, two values are reported.

post process integration over pixel rows to produce the equivalent of a one-dimensional horizontal camera. This type of analysis is useful to compare the GEM data with the data acquired from the existing SXR camera.
The MAST-U SXR diode diagnostic includes multiple pinhole cameras in both horizontal and vertical configurations, which serve as the primary benchmark for validating GEM data. The horizontal camera consists of two arrays of 32 photo-diodes spaced 50 mm apart, each generating a current when illuminated by photons. Its pinhole is a 1×3 mm^2 rectangular slit equipped with a 12.5 μm beryllium foil to block photons below 1 keV. The lines of sight (LOSs) are comparable to those of the GEM camera, as shown in Figure 5.6. The reduced number of LOSs and narrower plasma coverage of the GEM system are due to its compact design, which allows flexible orientation and positioning, including zooming adjustments by changing the detector-pinhole distance.

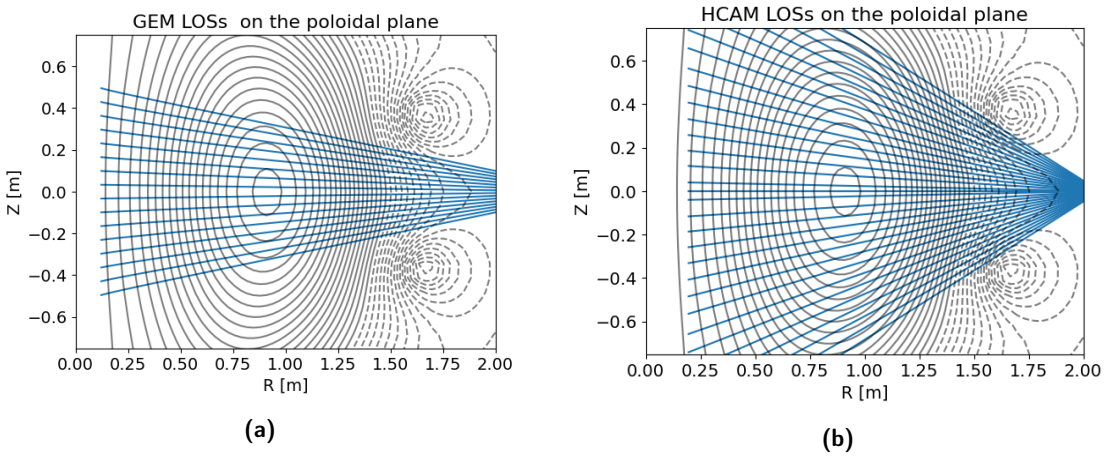

Figure 5.6: (a): LOSs geometry of the rows of the GEM camera. (b): LOSs geometry of the horizontal SXR camera.

5.2 Assessment of GEM diagnostic capabilities on the MAST-U spherical tokamak.

5.2.1 Validation of GEM data

To validate the measurements obtained with the GEM diagnostic, a direct comparison is performed against data from the MAST-U horizontal diode camera, with particular attention to the ohmic discharge #49020.
The analysis begins by comparing the global time traces of the two systems, using the Plasma Current signal (Figure 5.7a) as a reference indicator of the overall plasma behaviour. Because the two SXR diagnostics operate in fundamentally different modes, the GEM in photon-counting mode and the diodes in current-measurement mode, their respective time traces must be constructed using different procedures.
The horizontal camera produces a current signal over time from the diodes viewing the central plasma region, whereas the GEM time trace is generated from a time histogram of individual photon-count events summed over the pixels corresponding to the core of the plasma. An additional difference arises from the different detector sensitivities and from the different Beryllium window thicknesses. The horizontal camera is installed directly in the tokamak vacuum vessel and uses a 12.5μm Be filter, giving a low-energy cut-off of approximately 1 keV, with diode sensitivity essentially flat across the SXR range. In contrast, the GEM camera employs a 25μm Be foil, and photons travel through roughly 30cm of air before reaching the detector. Attenuation by Argon in the gas further suppresses low-energy photons, resulting in an effective cut-off near 3.2keV. The two reconstructed time traces are shown in Figure 5.7b. Their different energy sensitivities explain features such as the SXR peak at 0.58s detected by the diode camera but not by the GEM.
Despite these differences, both diagnostics capture the key temporal features: a total

pulse duration of about 0.82, s and a pronounced SXR crash at 0.21, s (indicated by the dashed red line), followed by a recovery of the SXR emission. This crash corresponds to an Internal Reconnection Event (IRE), a phenomenon characteristic of ohmic discharges in spherical tokamaks [70], and is also associated with a spike in the plasma current. The timing and occurrence of SXR peaks agree well between the two diagnostics, although their amplitudes differ due to the different detector sensitivities.

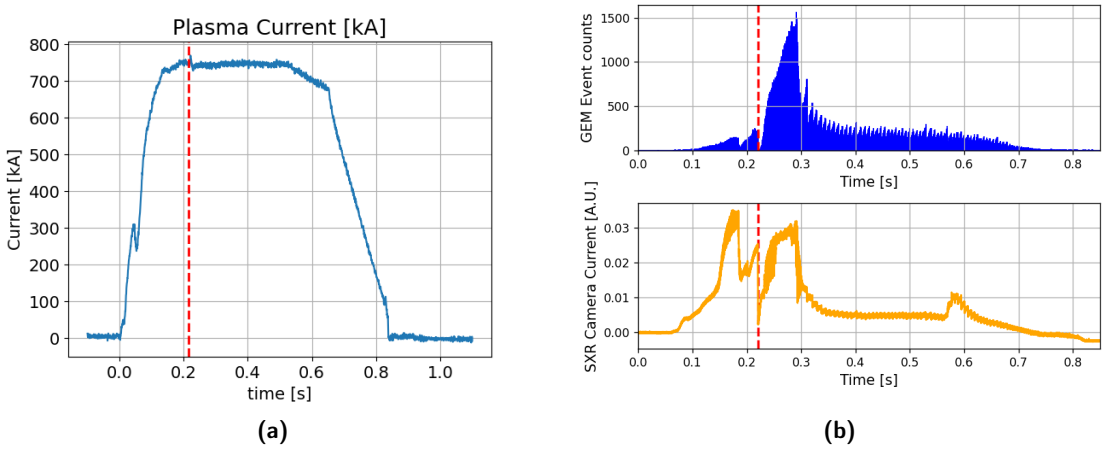

Figure 5.7: Ohmic shot #49020. (a): Plasma current. (b): Histogram of the GEM time-trace in blue on the upper plot, with a time binning of $0.1ms$; horizontal camera time-trace in orange on the lower plot. The IRE is highlighted with the dashed red line in the three graphs. From [67]

In the latter part of the discharge, clear sawtooth activity appears, visible in the time traces of both the GEM system and the horizontal diode camera. Sawteeth are well-known periodic instabilities in tokamak plasmas, marked by a gradual increase followed by a rapid collapse of the central temperature. Such events indicate a reconfiguration of the plasma core and influence both particle and energy transport, as well as the resulting SXR emission (Figure 5.8). Their consistent detection in both diagnostics provides additional confirmation of the correct operation of the GEM system.

Another important feature of SXR cameras is their ability to spatially localize SXR activity. An illustrative example from the ohmic discharge #49020 is the identification of the emission peak associated with a Snake instability [71, 72], whose characteristic signature is shown in Figure 5.9. This instability corresponds to a rotating region of increased density and enhanced X-ray emission, and its localization is crucial for tracking the evolution of key magnetic surfaces in the plasma. In MAST-U, the spontaneous appearance of snakes provides valuable information on impurity accumulation and confinement within a magnetic island prior to the first sawtooth crash [73], offering insight into plasma behaviour in the vicinity of these structures. In the case shown, sawtooth events occur from 0.31s, an example is shown in Figure 5.10.
Both the GEM and the horizontal diode camera consistently localize the maximum vertical extent of the SXR emission peak at approximately ±280, mm, as seen in Figure 5.10.

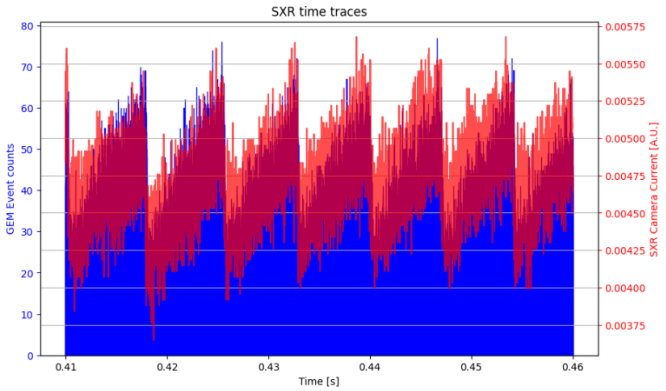

Figure 5.8: Ohmic shot #49020. The fingerprint of sawtooth activity at 130 Hz visible with the GEM and the diode cameras. The GEM time binning is 5 μs.

The peak is visible in the innermost lines of sight and gradually disappears toward the outer channels (only half of the LOSs are displayed for clarity).

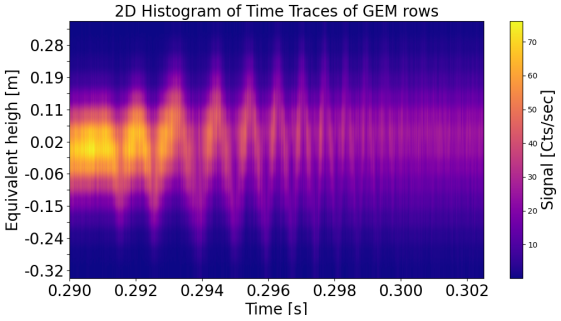

Figure 5.9: Ohmic shot #49020. The fingerprint of a snake instability, obtained by plotting the time histogram from every row of the GEM camera with a time binning of 10μs. On the y-axis is shown the equivalent height: the height of each row LOS at the plasma axis. From [67].

5.2.2 GEM Spectroscopic capabilities

The GEM detector provides both imaging capabilities and coarse spectroscopic measurements, enabling the study of plasma behaviour and the extraction of key plasma parameters from the acquired energy spectra. These spectra can be analyzed either through energy-selected cuts or by fitting procedures that quantify important plasma properties.
To interpret the measured spectra, it is important to consider that the dominant source of soft X-ray emission above 3keV in MAST-U plasmas is Bremsstrahlung radiation. The emissivity ϵ, expressed as a function of major radius R and photon energy E, depends sensitively on the electron temperature (T_e), electron density (n_e), and effective ion charge (Z_{eff}). For the ohmic discharge considered here, assuming a Maxwellian electron

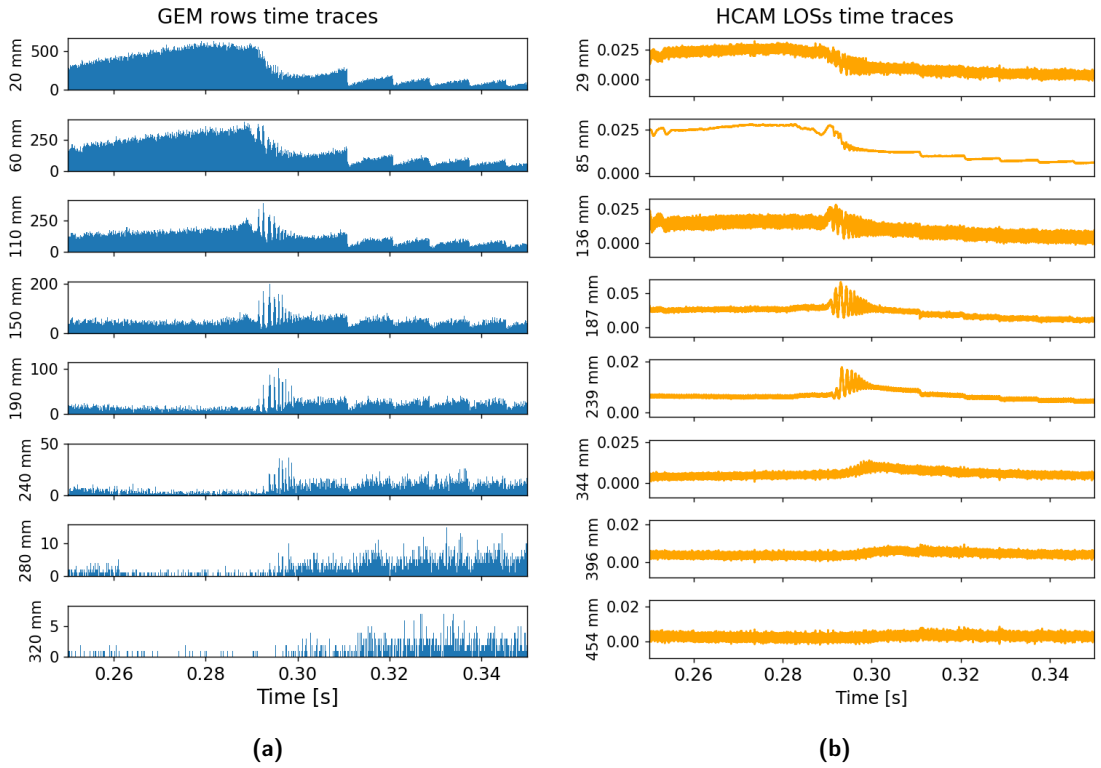

Figure 5.10: Ohmic shot #49020, presenting a snake instability at 0.29s and the first sawtooth crash at 0.31s. (a): Time-trace histogram for different GEM rows with 0.1ms time binning, identified with their equivalent height (the height of each row LOS at the plasma axis). (b): Time-trace histogram for different horizontal camera LOSs, identified with their equivalent height. From [67]

distribution, the emissivity decreases exponentially with energy, with a slope directly related to T_e.
An example of a GEM-based spectroscopic analysis is shown in Figure 5.11. An exponential fit of the simplified form in Equation 5.1, derived from Equation 1.11, is applied to extract an effective T_{eff} from the exponential slope:

$$\epsilon(E) = A \cdot E \cdot e^{-E/k_B T_{eff}}. \tag{5.1}$$

This estimation of T_e does not take into account the absorption of radiation along its path, nor the detector response function, therefore can be considered just an effective temperature, while the proper estimation of T_e will be discussed in depth in Section 5.4. Figure 5.11 shows a high-energy tail in the spectrum and a feature around 8 keV. The high-energy tail is attributed to neutron-induced background and is examined in Section 5.5. The feature observed around 8 keV could be attributed either to pile-up effects (since 8 keV corresponds to twice the main peak energy at 4 keV) or to fluorescence of copper present in the GEM detector. Copper is commonly found in several detector

components—including configurations employing aluminized GEM foils—and exhibits characteristic fluorescence lines around 8 keV. However, two observations support the pile-up interpretation:

1. The 8 keV feature is primarily visible in spectra from the MU3 campaign, where the GEM foils were made of aluminum, specifically to mitigate this effect [39]. In this configuration, the anode pads were $6 \times 6\text{mm}^2$. In contrast, during the MU4 campaign the GEM foils were made of copper (because aluminum GEM foils were not available at the time of detector construction), but the anode pads were reduced to $3 \times 3\text{mm}^2$, thereby lowering the detector count rate.

2. The presence of the 8 keV peak across multiple discharges, as well as its temporal evolution within individual shots, appears to correlate with the GEM detector count rate.

A brief discussion regarding the pile-up is mandatory: during some discharges, the detector operates at several hundred kHz per channel, leading to a pile-up fraction of a few percent, comparable to the height of the bump relative to the main spectrum (around 4% in height). The pile-up level can be estimated using the standard formula for a paralyzable detector [34]:

$$P_{\text{pile-up}} = 1 - e^{-r\tau}, \tag{5.2}$$

where r is the true count rate and τ the detector dead time. For the GEM system, $\tau = (100 + 50)$ns, consisting of a $\sim$ 100ns pulse length for an 8keV photon processed by the GEMINI chip plus an additional 50ns analysis time of the detector. An estimate of the pile-up probability for shot #49020 is provided in Figure 5.12.

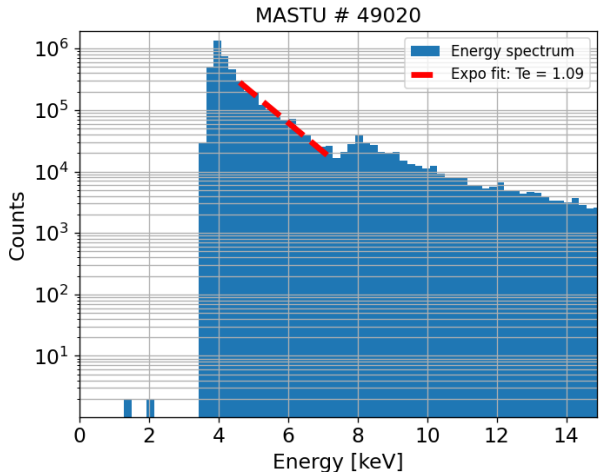

Figure 5.11: Ohmic shot #49020. Example of a GEM Energy spectrum integrate over the full pulse and over the entire camera. An exponential fit (the dashed red line) is applied in the range 4.2-7.5 keV to estimate an effective electron temperature. From [67]

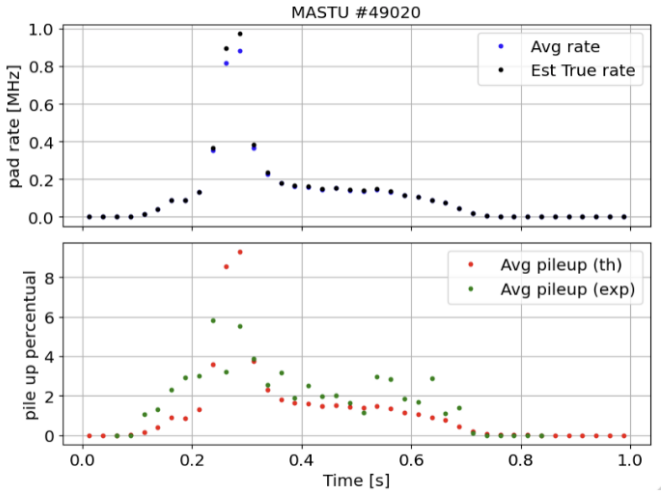

Figure 5.12: Estimation of the pile-up fraction for the ohmic shot #49020

During the shot #49020, the IRE induces a loop voltage that accelerates ions and electrons, resulting in the burst of SXR emission (figure 5.7b) and the rise of SXR energy. This event can be observed through an energy spectrogram perspective (Figure 5.13): the post-IRE burst generates both a rise in the temperature and a tail of high energy counts, in accordance with the theory [74].

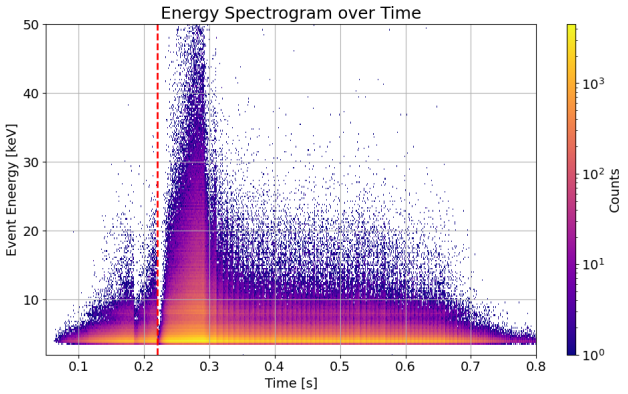

Figure 5.13: Ohmic shot #49020. Energy spectrogram: on the x-axis the time (time binning of 1ms), on the y-axis the SXR energy in keV and the color proportional to the logarithmic number of events per bin. The events are integrated over the whole camera. From [67]

5.2.3 Comparison with Revolt synthetic diagnostic

2D image comparison

In this section the GEM data from the MU3 campaign are compared with synthetic data produced with the Revolt-U software with the dual result of furthermore validate the Revolt-U product and to interpret the experimental data.

The first comparison concerns the detector image. The data analyzed are taken from shot #49020, in the time window $[0.2, 0.25]$s. The 2D image obtained with the GEM camera selecting only the counts in the $[5, 7]$keV energy range. This range is associated with pure SXR emission (see section 5.5).
The REVOLT-U image is obtained by dividing the plasma volume in $120 \times 120 \times 120$ cylindrical voxels and associating to each voxel, seen by the detector, the Bremsstrahlung emissivity (see Chapter 3). The density and temperature used in the formula are those measured experimentally by the Thomson Scattering diagnostics of MAST-U, and are shown in figure 5.14 together with the poloidal magnetic flux function $\Psi(R, Z)$, from the magnetic reconstruction. The effective charge Z_{eff} and the Gamov factor g_{ff} are assumed to be constant and equal to 1.5 and 1, respectively, following the standard approximations commonly adopted in the MAST-U community for plasma modelling [75].
The GEM experimental data and REVOLT-U synthetic data are shown in Figure 5.15.
The difference between REVOLT-U and MAST-U data are quantified by calculating the residuals, pixel by pixel, between the normalized images and the root mean square error (RMSE). Normalization is obtained by dividing the counts in each pixel by the counts of the maximum counting pixel.
The Revolt-U synthetic data exhibit an acceptable correspondence with the experimental data, with both images sharing a similar overall structure and intensity gradients: the RMSE is 0.264 and the residuals remain below 0.5. In the upper part of the image (for y pixel IDs between 0 and 7), the residuals remain below 0.3, while more critical is the lower part of the image. Nevertheless, the simulated data capture the overall intensity distribution, with its transition to lower counts toward the center, demonstrating the model capability to reproduce key experimental features. While discrepancies are present, these differences might be attributable to the exclusion of detector electronics artifacts in the simulation, or to the simplified model adopted for the plasma emissivity.

It is clear from the 2D image that the detector is not alligned perfectly with a radial Line Of Sight: the image appears asymmetric, indicating that the detector is slightly tilted.

Such an effect is likely due to the manual alignment of the diagnostic during the installation, but it does not constitute a severe problem. Nevertheless, quantifying the magnitude of this misalignment is useful for a clear interpretation of the experimental data. To this end, the Revolt code is used to make a manual forward fit, consisting in repeating the emission simulation modifying the GEM tilting angle corresponding to the radial direction. With a direct comparison with the experimental data the estimate tilting angle is found to be 1.5 deg, the field of view tilting is visualized in Figure 5.16.

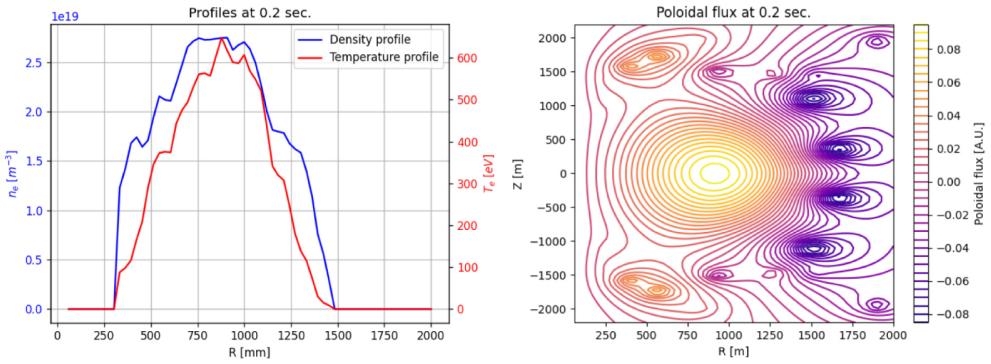

(a) (b)

Figure 5.14: (a) Shows the density and temperature profiles of MAST-U shot #49020, measured at 0.2s. (b) Shows the poloidal flux of the same MAST-U shot, at the same time instant. From [48]

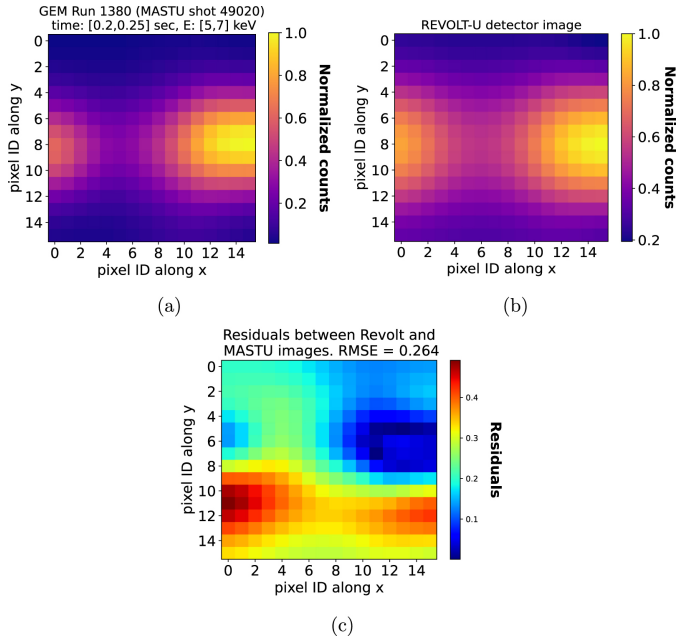

(a) (b)

(c)

Figure 5.15: Comparison of experimental data from MAST-U shot #49020 (a), with the synthetic data obtained with REVOLT-U (b). In both cases, data are normalized in [0,1]. (c) Shows the residuals between the normalized images of (a) and (b). The value of the RMSE calculated is $0,254$. From [48]

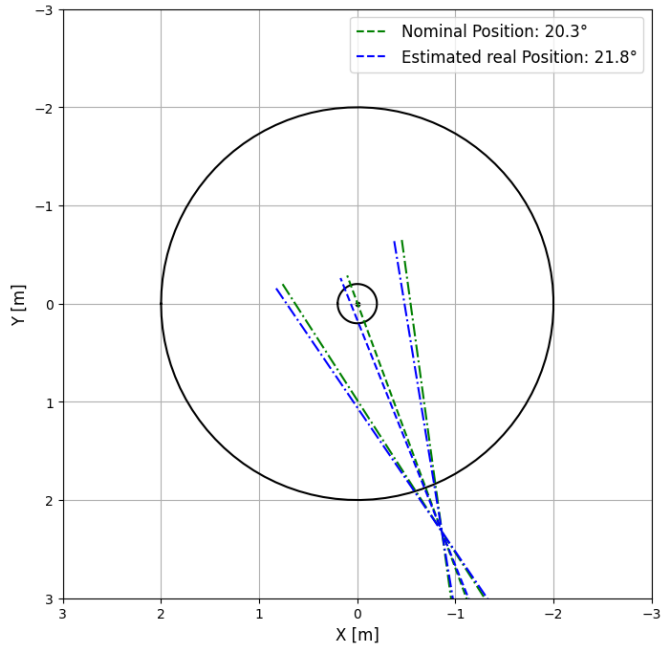

Figure 5.16: Scheme of the GEM field of view tilting during the MU3 experimental campaign.

Spectra comparison

The same method of producing the 2D synthetic image is used for producing a spectrum from the data of three shots: #49020, #49012, #49013, the respective MAST-U data are shown in Figure 5.17. The SXR attenuation path is described in Table 5.2, even though the precise material length vary slightly from each pixel-voxel pair, according to the Revolt-U geometrical calculation.
To further improve the reproducibility of the synthetic data, the synthetic counts are normalized on the experimental counts of shot #49020, and the normalization coefficient α is used for the comparison of the two remaining shots. A brief description of the process is given here. The experimental counts C_{exp} measured in each GEM pixel (integrated over the time window $[0.17, 0.23]$ s) are compared with the corresponding simulated counts C_{sim}.

- A linear fit of the form $y = \alpha x$ is performed in the range 5.3–7.4 keV. This selection avoids detector non-linearities, neutron-induced background, and pile-up.

- The REVOLT-U uncertainty with respect to experimental data is estimated as

$$\text{err} = \text{std}(C_{\text{exp}} - \alpha\, C_{\text{sim}})\,, \tag{5.3}$$

  where std() denotes the standard deviation.

- Figure 5.18(a) shows C_{exp} versus αC_{sim}; each point corresponds to a pixel. Statistical error bars are given by

$$\text{err}_i^{\text{stat}} = \sqrt{C_{\text{exp}}(i)}\,, \tag{5.4}$$

  where i is the pixel index. The lines $y = \alpha x$, $y = (\alpha + \text{err})x$ and $y = (\alpha - \text{err})x$ illustrate the fitted scaling and its uncertainty.

With the global scaling constant $\alpha = 0.2 \pm 0.1$ determined, and its uncertainty estimated from the integrated counts, the simulated energy spectrum is compared with the experimental one. The simulated spectrum is the REVOLT-U output, summed over pixels and scaled by α. Figure 5.18(b) shows the comparison. Simulated error bars are obtained by multiplying the bin heights by $\alpha \pm \text{err}$, while experimental uncertainty is statistical:

$$\text{err}_i^{\text{stat}} = \sqrt{h_i}, \tag{5.5}$$

where h_i is the height of bin i.
The simulated spectrum does not reproduce the low-energy peak at $[3.2, 4.5]$ keV of the experimental spectrum because the discrepancy is attributed to non-ideal detector electronics near threshold. Good agreement (within the REVOLT-U uncertainty) is observed in the range 4.5–7.5 keV, which corresponds to pure SXR emission, the only component modelled by REVOLT-U. Above 7.5 keV, an increasing mismatch appears, due to pile-up, and neutron background, subject of the following Section 5.5.
To test robustness, the same α and err extracted from shot #49020 are applied to Revolt-U simulations of shots #49013 and #49012. Figure 5.19 compares the resulting spectra with the MAST-U measurements. Both shots exhibit behavior consistent with that of #49020, indicating that the Revolt-U estimates are stable across different experimental conditions.
Overall REVOLT-U provides a reliable estimate of the expected SXR-only counts and spectra. This makes it particularly valuable in the design phase of SXR diagnostics, where order-of-magnitude accuracy is sufficient to assess feasibility and support key design decisions.

5.3 Study of localized SXR emission energy.

The GEM diagnostic installed on the MU3 campaign has been upgraded for the 2024 MAST-U MU4 campaign. Three main upgrades have been made: the GEM detector has been replaced with one featuring an upgraded anode, a remote controllable iris has been installed as a pinhole, and the Point of View (POV) has been changed.
The anode pads has been updated from the 256 $6 \times 6mm^2$ pads, to an anode with 384 pads, of which 16×16 are $3{\times}3mm^2$ in the center of the anode, plus 128 $6{\times}6mm^2$ "external" pads, shown in Figure 5.20. The benefit of this upgrade are straightforward: with same SXR (and neutron) fluxes on smaller pads, the pile-up probability diminish, and smaller pads allows a better space resolution. The second upgrade is the controllable metal iris

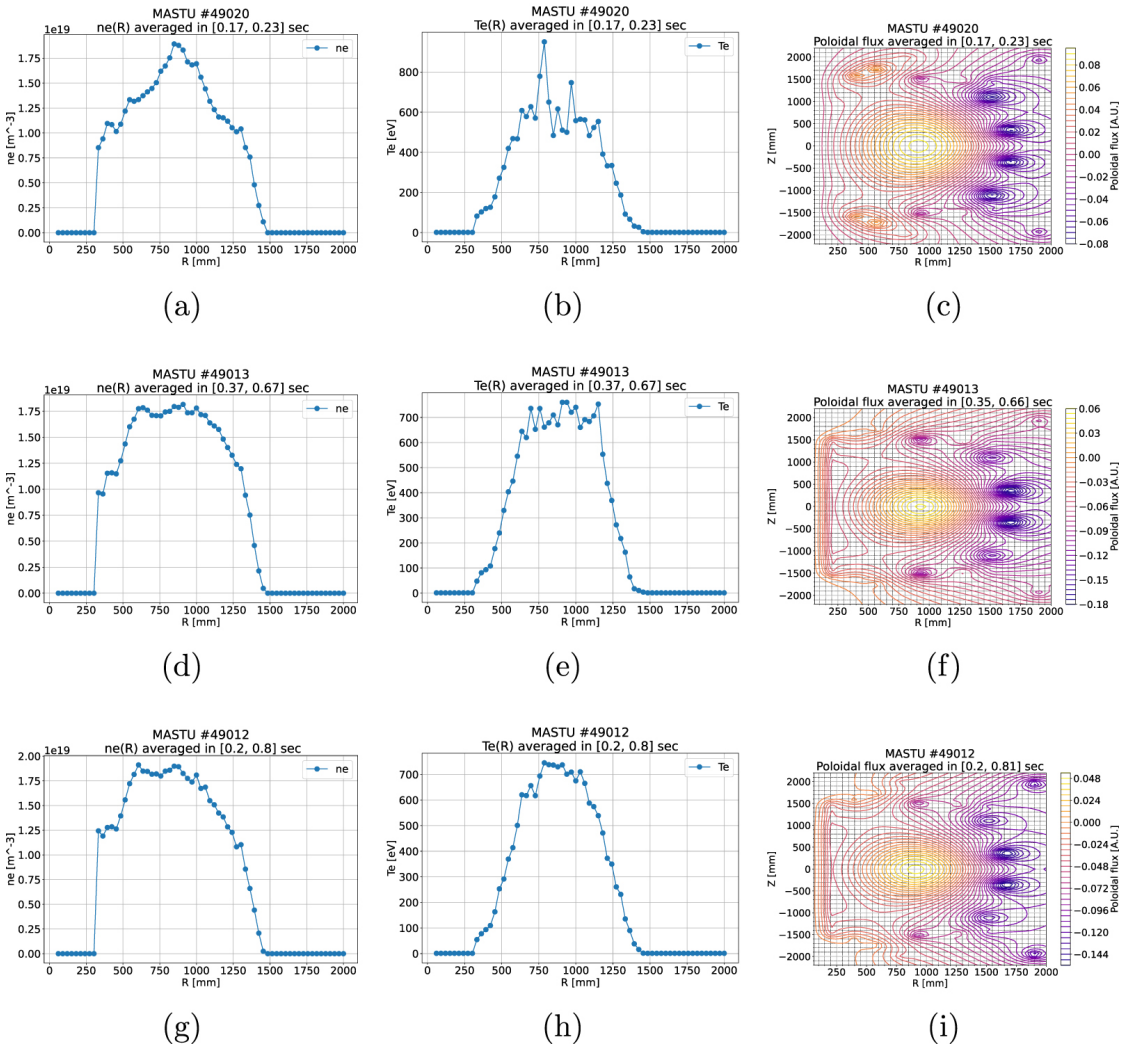

Figure 5.17: MAST-U input data $(n_e(R), T_e(R), \Psi(R,Z))$ for SXR synthetic data production. From [48].

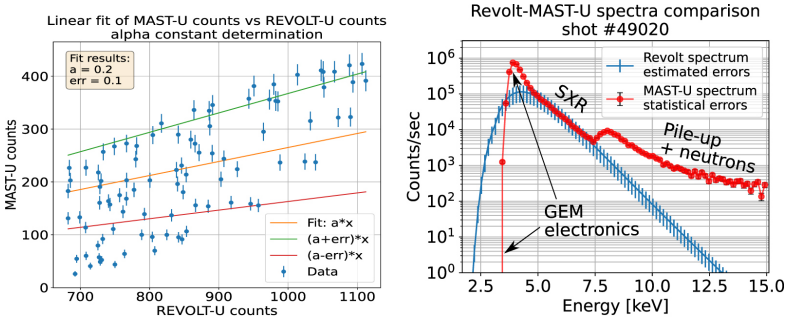

(a) (b)

Figure 5.18: Comparison of Revolt-U synthetic data and GEM experimental spectrum for shot #49020. (a) shows the extrapolation of the α to scale the synthetic counts with the experimental spectrum. (b) shows the spectra comparison. From [48]

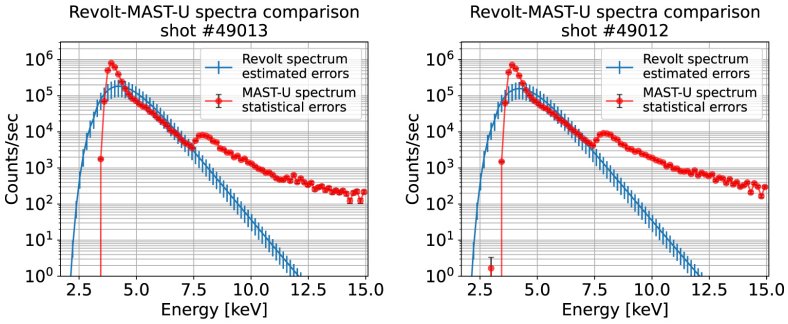

(a) (b)

Figure 5.19: Comparison of Revolt-U synthetic spectrum and the GEM experimental spectrum for shots #49012 and #49013. From [48].

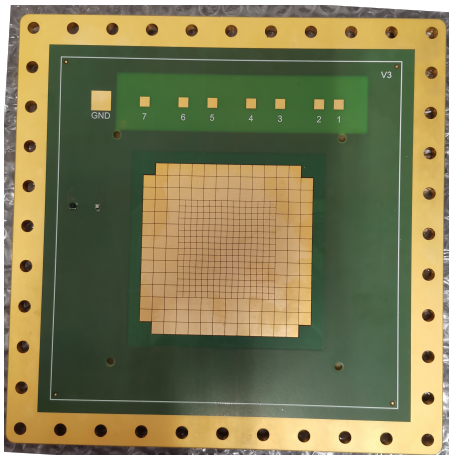

Figure 5.20: Picture of the 384 pads anode of the GEM detector installed on the MU4 MAST-U experimental campaign.

installed 2cm after the beryllium window: it allows to adapt the pinhole diameter to different MAST-U shots parameters, to diminish the incident flux on the detector. The Iris maximum diameter is 20 mm (whereas the Beryllium window is 13mm) and can be diminished down to 1mm. In particular for Ohmic shots, the Iris can be kept open, while for NBI shots the Iris is generally set to its minimum of 1mm.
The third upgrade is the switch from a radial POV to a tangential POV, this allows the exploitation of the two dimensions of the detector, that can be used to reconstruct poloidal emission images of the plasma, similarly to what have been done with the GEM diagnostic installed on EAST tokamak [52]. Figure 5.21 shows the difference in the POV of the GEM camera.

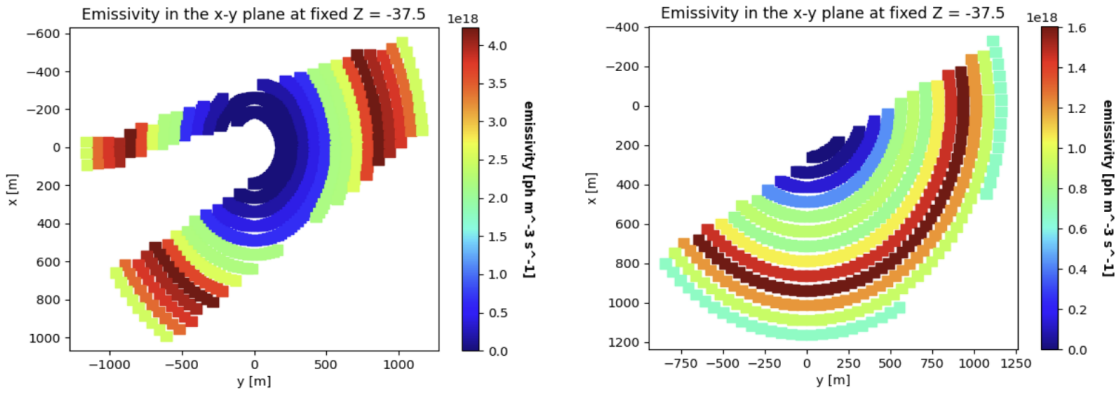

(a) MU3 **(b)** MU4

Figure 5.21: Comparison of the POV of the GEM camera on MU3 and MU4 campaigns on MAST-U. The emissivity of two plasma shots are shown as examples.

2D Images Inversion

In this section the workflow used to solve the inversion problem using the Tikhonov minimization method in the GSVD framework described in Chapter 3 is presented. Shot #51920 is used as a reference example, its main plasma parameters are shown in Figure 5.22. During this shot the iris diameter is 1mm, the total Voltage on the GEM foils is 1100V.

The data processing and inversion steps are:

1. Acquisition of line-integrated SXR signals from the GEM detector, each corresponding to a specific line of sight, as shown in Figure 5.23. The data are organized in 2D images integrated over time windows at a chosen duration. In the present example, the frequency is 200 kHz, covering the time interval from 0.2 s to 0.7 s.

2. Preprocessing of the raw GEM data. Because the GEM images obtained during the MU4 (and MU3) campaigns were significantly affected by noise, arising from neutron-induced background and channel-to-channel gain fluctuations.

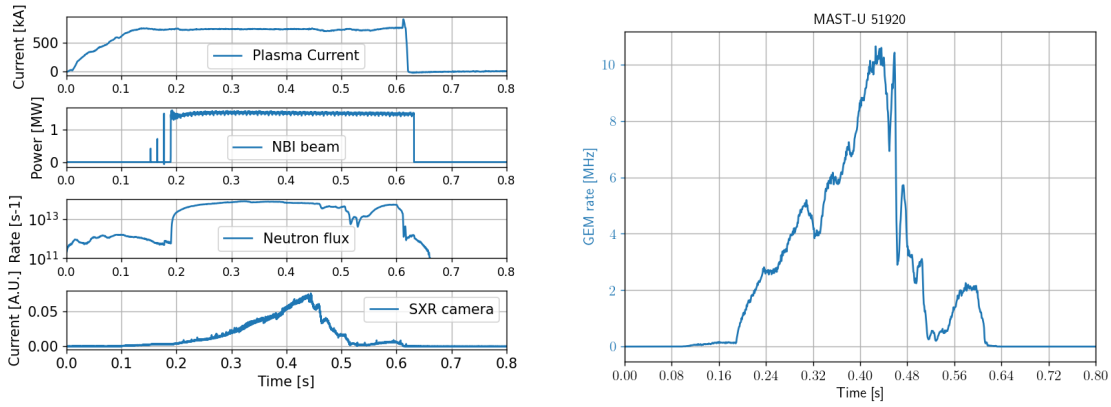

(a) (b)

Figure 5.22: Time traces of few global plasma parameters for MAST-U shot #51920: on the left the MAST-U parameters, on the right the GEM global timetrace.

(a) The poloidal emission reconstruction is limited to the 256 central pads ($3 \times 3\text{mm}^2$) due to a non-uniform response between small and large pads. This non-uniformity originates from the different pad sizes, which result in different capacitances and, consequently, different collected charges. At present, the GEMINI readout does not apply pad-size-dependent calibration, so these capacitance differences are not compensated. This impacts the Time-over-Threshold acquisition method, the detection efficiency for low-energy signals, and charge sharing between small and large pads, ultimately introducing undesired biases in the reconstructed detector images. Future work will focus on calibrating the GEMINI readout capacitances to equalize the response across pad sizes. Despite this limitation, identified during the MU4 campaign, the reconstruction method remains valid for the present study.

(b) Malfunctioning channels are corrected by replacing their counts with the average of neighboring channels. This step mitigates the non-uniformity of the detector, which would otherwise significantly impact the inversion.

(c) Singular Value Decomposition (SVD) of the data matrix along the spatial and temporal axes, following the approach of [76]. Calling the data matrix S of size $N_{\text{time}} \times N_{\text{pads}}$, the SVD reads

$$S = U \Sigma V^T,$$

where U contains temporal modes named *chronos*, V contains spatial eigenimages named *topos*, and $\Sigma = \text{diag}(\sigma_1, \sigma_2, \dots)$ contains the singular values in decreasing order. Each pair of chronos and topos associated with a singular value σ_i constitutes a spatio-temporal element of the orthonormal basis, that describes the data set. Figure 5.24 illustrates the decomposition, while Figure 5.25 shows the singular values. The magnitude of each singular value

σ_i reflects the information content of its associated mode. A confirmation of the quality of the SVD analysis is the topos of the first singular value, which time-development closely resemble the global GEM timetrace of Figure 5.22

(d) Selection of dominant singular values: since noise predominantly populates small singular values, truncating Σ naturally smooths the GEM images. Only the first k modes with the largest σ_i are retained. The truncated SVD reconstruction is therefore

$$S_k = \sum_{i=1}^{k} \sigma_i U_i V_i^T,$$

effectively suppressing high-frequency noise. In our case, three dominant modes capture nearly all the relevant information. Figure 5.26 compares the original data and the reconstruction using only these three modes.

(e) The processed data are then organized into a $x \times 256$ matrix, where x is the number of time bins and 256 corresponds to the number of central pads.

3. Construction of the forward model through the geometric response matrix L obtained with Revolt-U. The matrix dimensions are 256×256, corresponding to a plasma discretization of $16 \times 16 \times 180$ voxels projected onto the poloidal cross-section along magnetic field lines.

4. Application of Tikhonov regularization to each SVD-filtered frame of the selected time window. For each time slice, the numerical GSVD method is used to solve the inversion problem (see Chapter 3). The resulting emissivity map is shown in Figure 5.27.

An additional example, from shot #51913, of reconstruction is given, where the camera observe a vertical displacement of the plasma, also visible from the magnetic flux surfaces reconstruction. The time lapse at 200Hz is shown in Figure 5.28, together with the reference Thomson Scattering radial profiles for an extracted time frame, shown in Figure 5.29.

Although the results are encouraging, they should be regarded as preliminary. More refined analyses will be explored in future work, such as:

- reconstructing only the perturbed emissivity by discarding the first SVD mode and inverting from the second onward, potentially enhancing the visibility of magnetic islands,
- reducing the temporal integration time to resolve faster phenomena, such as MHD modes.

At present, the stability of the GEM channels still requires improvement, as artifacts can affect the robustness of advanced reconstructions. A more detailed characterization of the pixel response uniformity, along with a deeper study of how pressure and temperature variations and charging-up effects influence the GEM behaviour, will likely enable these

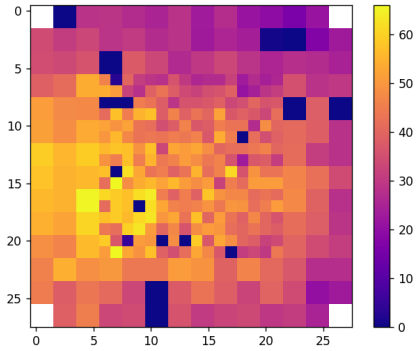

Figure 5.23: Heatmap of the signal on the GEM detector during the MAST-U shot #51920, integrated in the time window $[350, 355]$s.

developments. However, these aspects could not be fully addressed within the scope of this thesis.

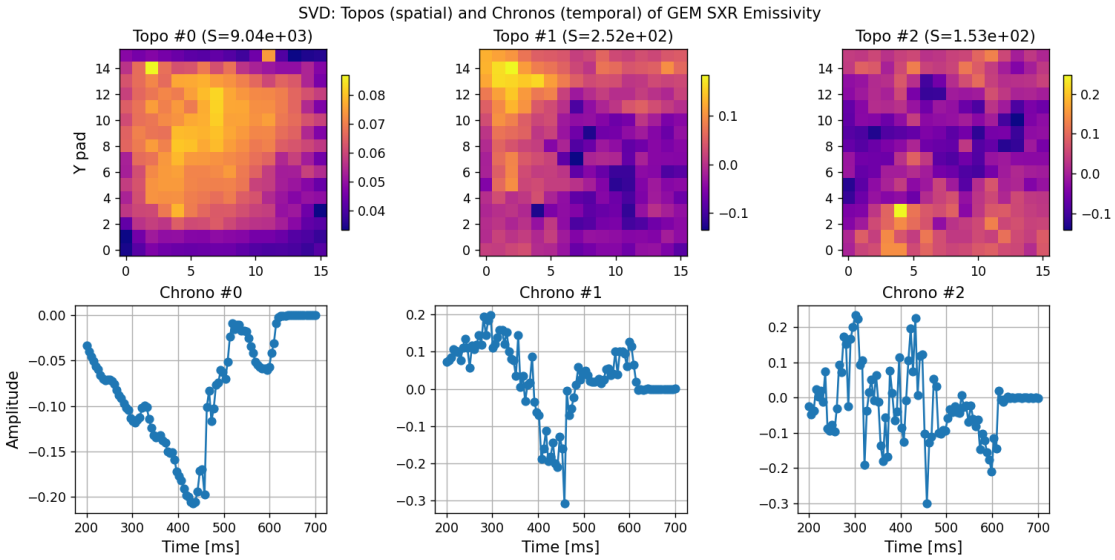

Figure 5.24: SVD decomposition in temporal (chronos) and spatial (topos) eigenmodes for the GEM heatmap during the MAST-U shot #51920.

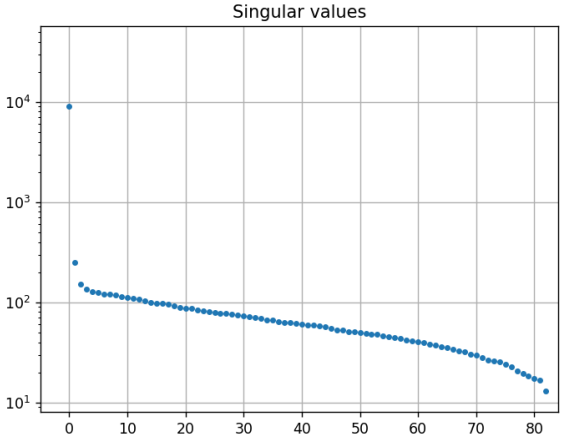

Figure 5.25: Singular Values obtained with the SVD of the GEM 2D images of the MAST-U shot #51920.

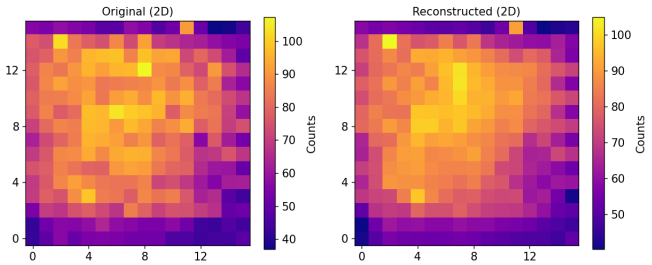

Figure 5.26: Reconstructed Heatmap of the signal on the GEM detector during the MAST-U shot #51920, integrated in the time window $[350, 355]$s. On the left the detector signal, on the right the SVD reconstruction.

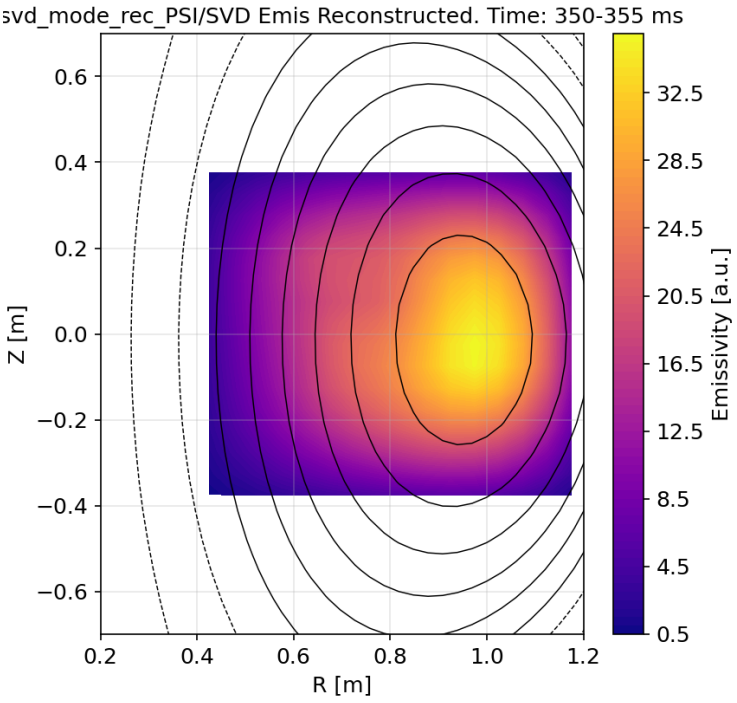

Figure 5.27: Example of the recostructed poloidal emissivity during the MAST-U shot #51920, integrated in the time window $[350, 352]$s. The magnetic flux lines are plotted as reference.

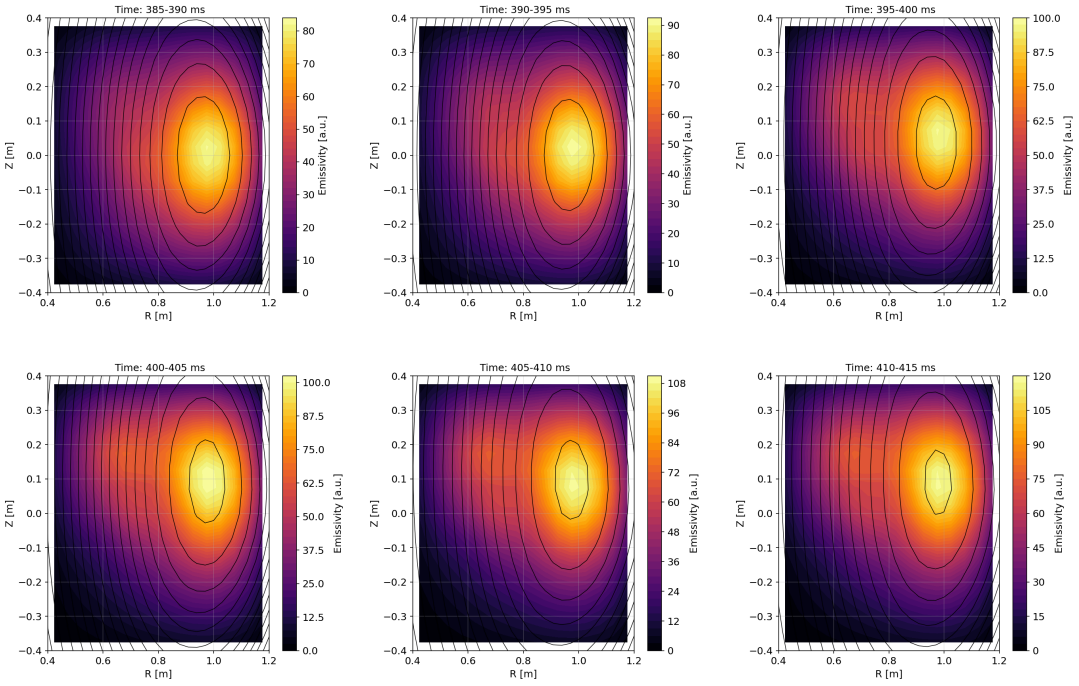

Figure 5.28: NBI heated MAST-U shot #51913. Time lapse, at 200Hz, of a vertical displacement. Reconstruction from the GEM camera (coloured plot)on the EFIT++ magnetic reconstruction (black lines).

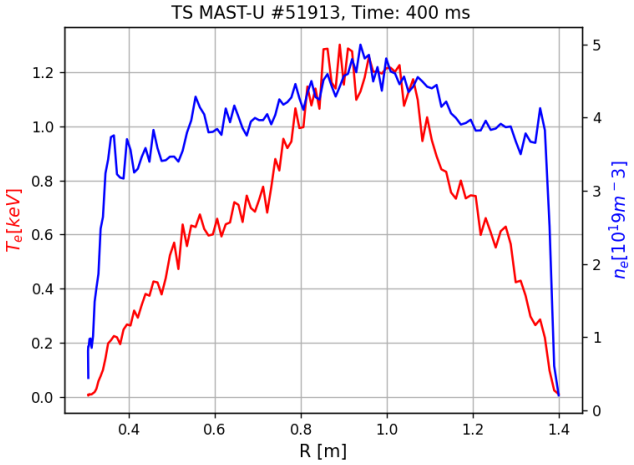

Figure 5.29: Thomson scattering data of radial T_e and n_e of shot #51913 in the time window 395-405 s.

5.4 Te estimation technique

This section illustrates the data analysis designed to infer the Electron Temperature T_e from the GEM energy spectrum. Figure 5.11 shows an estimation of what can be defined as electron effective temperature, but the method adopted to extract the parameter was a simplification that ignored two important aspects: the SXR attenuation before reaching the GEM detector, and the energy response of the detector. The resulting estimation can be therefore treated as an effective temperature. In this section the analysis is refined to obtain a valid estimation. Nonetheless, a key assumption still holds: the SXR spectrum is dominated by Bremsstrahlung emission. This restricts the applicability of the method to an energy interval where detector response non-idealities, such as pile-up or neutron background (see next Section), are negligible. Under the present experimental conditions, this requirement limits the analysis to Ohmic heated plasmas.
Line radiation is also neglected as a source of spectral distortion. This is justified because the relatively low electron temperature (around 1 keV) is insufficient to significantly excite high-Z impurities, while the air attenuation along the SXR path suppresses the low-energy portion of the spectrum where emission lines may appear. With these considerations, the approach remains general: in other scenarios, the energy interval for the fit can be suitably chosen to exclude additional spectral features.

5.4.1 Detector energy resolution effect

The first correction addresses the non-constant energy resolution of the triple GEM detector, which arises from stochastic gain fluctuations that depend on the deposited energy, combined with manifacturing and electronic non-idealities. To model the GEM energy resolution, each energy bin can be represented as convolved with a function that is well-approximated by a Gaussian, whose width (FWHM) corresponds to the detector resolution at that energy. The resulting spectrum is obtained by summing the contributions of all initial energy bins, each broadened by its corresponding Gaussian. The experimentally measured energy resolution of the detectors used in this thesis is shown in Figure 5.30.

Given that the detector response introduces an energy-dependent broadening, the measured spectrum $S'(E)$ is therefore not a direct representation of the physical spectrum $S(E)$, but rather a convolution of it with the detector response. Mathematically, this can be written as

$$S'(E) = \int S(E')\, G(E, E')\, dE' \tag{5.6}$$

where $G(E, E')$ is the Gaussian kernel whose width reflects the detector's energy resolution at the true energy E'. As a consequence, the gradient in the energy resolution redistributes counts unevenly across the spectrum: energies with poorer resolution spread their content over many bins, while regions with better resolution confine the counts into fewer bins. This effect distorts the apparent spectral shape, as illustrated in Figure 5.31.

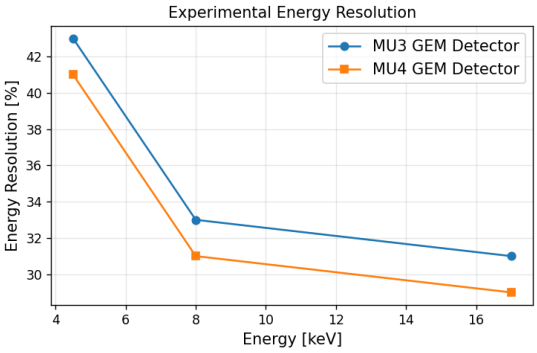

Figure 5.30: Experimental energy resolutions at different energies of the detectors exploited in the MU3 and MU4 campaign. Calculated as $E_{res} = FWHM/E_P$, where E_P is a peak position, anf its respective FWHM, for Fluorescence lines of respectively T_i, Cu, Mo.

To recover the original spectrum $S(E)$, an inversion of the convolution is required. However, this is an ill-posed problem: directly inverting the response matrix amplifies noise and produces unphysical oscillations. Because of this reason, we employ Tikhonov regularization, which stabilizes the solution by balancing fidelity to the measured spectrum with smoothness constraints. The deconvolution is formulated as

$$\min_S \left\|GS - S'\right\|^2 + \lambda^2 \left\|LS\right\|^2, \tag{5.7}$$

where G is the discretized response matrix, L is a smoothing operator, in this work a second-derivative matrix, and λ is the regularization parameter. The first term enforces agreement with the measured data, while the second suppresses noise-driven oscillations. By selecting an appropriate value of λ with the L-curve method, Tikhonov deconvolution retrieves a physically meaningful estimate of the true spectrum, preserving real features such as peaks while mitigating the distortions introduced by the energy-dependent resolution, an example on simulated data is given in Figure 5.32.

5.4.2 SXR attenuation

The second aspect is the SXR attenuation from the media on its path, and the detector efficiency. Figure 5.33 illustrate the value of the attenuation coefficients in the energy range of interest, for the material along the SXR path in the MAST-U set-up. The tensor matrix provided by Revolt-U is used to divide the count of each energy bin by the corresponding attenuation coefficient (see Chapter 3). Revolt-U tensor also includes the correction for the detector efficiency, given by the photoelectric coefficient of the gas mixture. The result of the overall process is shown in Figure 5.34.

Finally, the spectrum can be fitted using Equation 5.1 to extract the electron temperature T_e, as shown in Figure 5.35. This procedure was applied to the GEM diagnostic data, integrated over the full detector and evaluated in 10 ms time windows, for different Ohmic

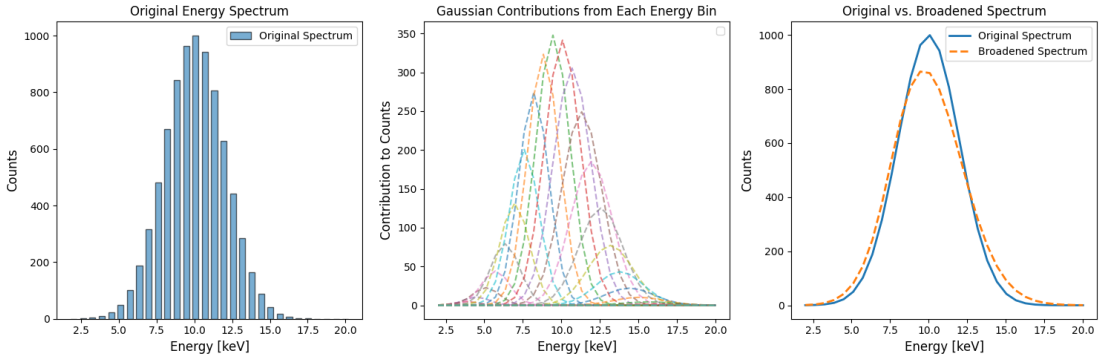

Figure 5.31: Example of the effect of the varying energy resolution on a Gaussian histogram. From the left to the right: the starting histogram, the gaussians centered on each bin, and the result of the convolution. The standard deviation of each gaussian is computed by evaluating the linear interpolation of the energy resolution of the MU4 detector at the corresponding energy.

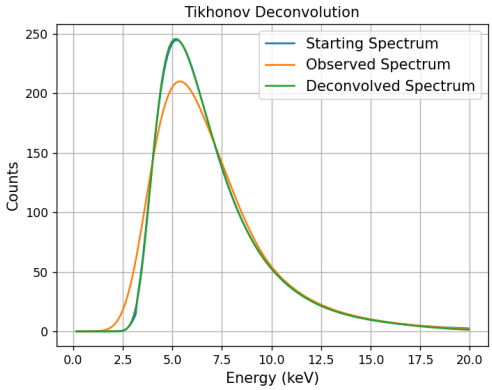

Figure 5.32: Deconvolution of a Revolt-U simulated SXR spectrum in the MU4 configuration with the detector varying energy resolution response. The SXR source is modelled as a single voxel emitting isotropically a Bremmstrahlung spectrum with temperature of 1keV.

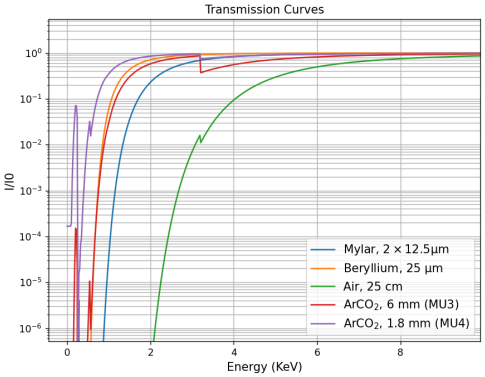

Figure 5.33: Attenuation curves for the media on the SXR path of the GEM diagnostic on MAST-U (see Table 5.2).

shots, shot #51356 is reported as proof-of-principle. Figure 5.36 illustrates the impact of the data-processing pipeline by comparing the T_e estimates obtained from fits to the raw data with those derived from the processed data, using the parameters estimated by the Thomson Scattering diagnostic as a reference. The method shows good agreement with the Thomson Scattering measurements, representing a promising result.
The next step in exploiting the GEM diagnostic is to extend this analysis to subsets of pads (or even individual pads) in order to reconstruct spatially resolved T_e profiles. At present, however, this approach can only be applied to Ohmic shots: NBI-heated discharges are dominated by a strong neutron-induced background that masks the dependence of the spectrum on T_e. The following section is dedicated to analysing this effect.

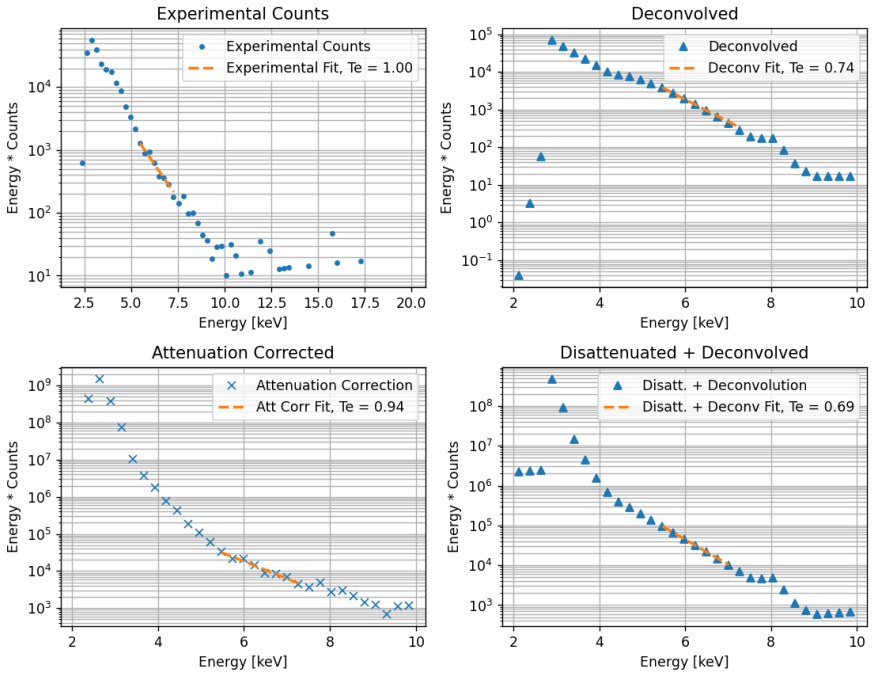

Figure 5.34: Experimental energy histogram treated during the analysis to extrapolate the electron temperature. Figures illustrate the experimental spectrum, the separate effects of the energy-deconvolution and of the disattenuation and the combined result by applying first the deconvolution and then the attenuation correction.

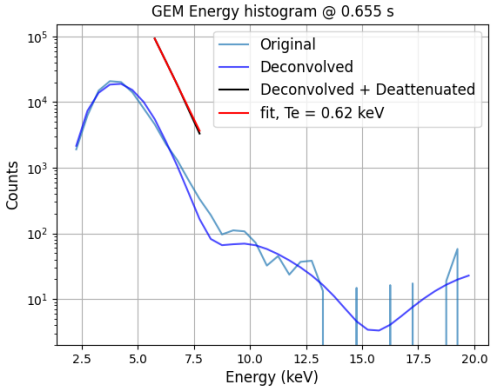

Figure 5.35: Example of electron temperature estimation from GEM data treated with attenuation correction and detector energy resolution deconvolution.

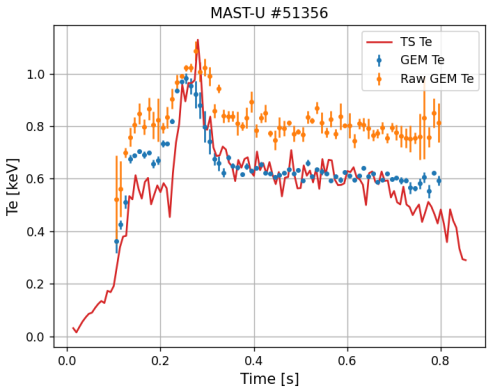

Figure 5.36: Time traces of the T_e estimated with the data integrated over the whole GEM camera. The values are from the direct estimation of the untreated data, and from the deconvolution and dis-attenuation processes, compared with the estimated Thomson Scattering core T_e.

5.5 Neutron-related background studies

Figure 5.11 suggested the presence of a signal that cannot be attributed to SXR radiation above 10keV. In this section, the origin of this signal is analyzed and shown to arise from neutron-related background. This contribution is particularly significant during NBI-heated discharges, where plasma performance is enhanced, compared to ohmic-only operations.

5.5.1 Study of neutron related background in GEM data

Identification of neutron related background

The first step to assess the influence of neutron background on SXR measurements is to close the gate valve in front of the Beryllium window during selected MAST-U discharges. In this configuration, SXR are effectively blocked, so only neutrons and gamma radiation reach the GEM detector and generate a signal [77]. The resulting time traces can then be compared with both the SXR signal recorded by the horizontal camera and the neutron signal from MAST-U fission chambers [78], as well as with standard shots where the gate remains open. The measured time-traces are shown in Figure 5.37. The first observation is that significant amount of signal is measured also with the gate closed, up to few MHz integrating over the whole detector. The data also reveal that in gate-closed shots (Figure 5.37a), the GEM signal (blue) closely follows the neutron signal (red), whereas in gate-open shots (Figure 5.37b), it aligns with the horizontal camera SXR signal (orange). This comparison clearly demonstrates the presence of neutron-induced background in the GEM measurements. Applying an energy cut to the GEM signal in gate-open shots, as shown in Figure 5.38, further demonstrates that the high-energy part of the spectrum (events with energy > 10 keV, shown in red in Figure 5.38a) is predominantly due to neutron-related background, as it closely follows the neutron signal (red

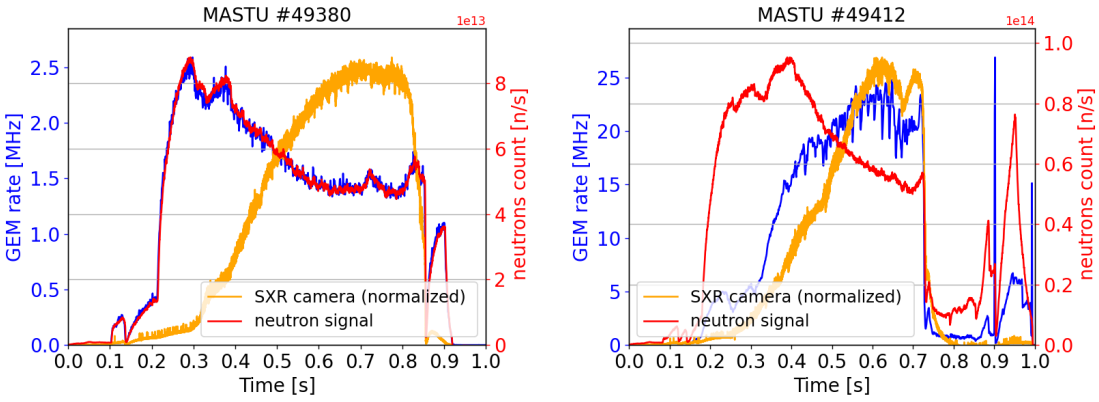

(a) From [67] **(b)**

Figure 5.37: Comparison of the time evolution of: the GEM counts (in blue), the neutron rate (in red), normalized horizontal camera SXR signal (in orange) (a): Shot #49380, beam on, gate closed. (b): Shot #49412, beam on, gate open. From [67]

in Figure 5.38b), whereas the low-energy portion reproduces the SXR signal (orange in the figures). The overall GEM signal (blue) continues to track the SXR evolution, and the ratio of counts indicates a neutron contribution between 1% and 10% of the total, depending on plasma conditions (higher during NBI-heated shots, lower during Ohmic shots) and the choice of energy cut. These observations underline the importance of improving the signal-to-noise ratio to enable more detailed energy-resolved analysis.

Analysis of the post-IRE burst in GEM data

An important feature of the GEM signal, discussed in Section 5.2.2, is the post-IRE spike. It is interesting to determine whether this spike arises solely from increased neutron activity or also from elevated electron energy. Figure 5.39 presents data from shot #49452 with NBI. The neutron rate rises sharply between 0.2 s and 0.3 s and continues to increase more gradually until 0.4 s (red line in Figure 5.39a). The GEM signal, however, peaks at 0.3 s before rapidly decreasing (blue line).

Figure 5.39b shows the ratio of the GEM signal to the neutron rate for all GEM events, as well as for subsets with energies below and above 10 keV. If the GEM signal were entirely neutron-driven, as in the gate-closed shots (Figure 5.37a), these ratios would be flat. Instead, the peak observed between 0.2 s and 0.33 s across all three cases indicates that the signal is primarily SXR in origin, whereas the flat region between 0.33 s and 0.4 s corresponds to a neutron contribution.

The ratios for different energy cuts reveal differences in the neutron influence on the GEM signal. The peaks at 0.28 s in the global and low-energy cut ratios (blue and orange in Figure 5.38b) are roughly four times the baseline, indicating a minor neutron contribution. By contrast, the high-energy cut ratio (red) shows a peak only 1.5 times

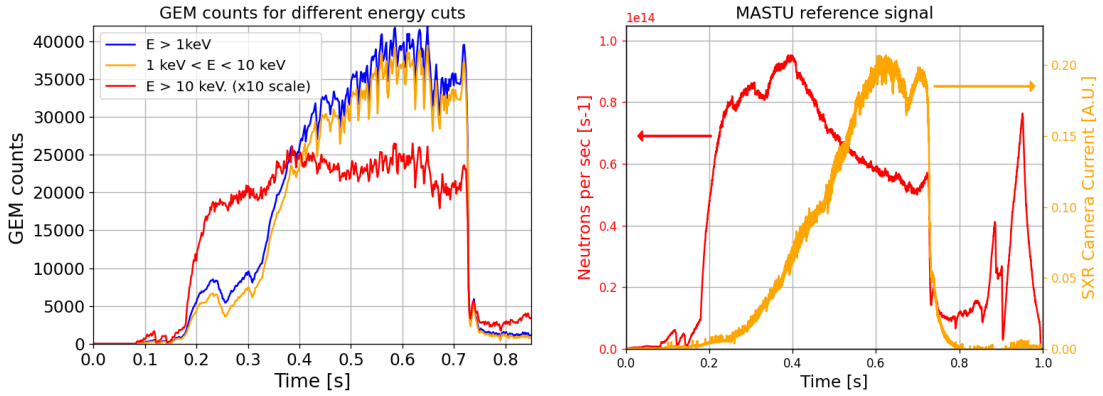

Figure 5.38: Signals time evolution of Shot #49412, with beam heating on. (a): GEM signal time trace. The global trace is shown in blue, the trace for events with energy $E < 10keV$, in orange, and the trace for events with energy $E > 10keV$, in red (scaled by a factor of 10 for visibility). (b): Reference signals: SXR time evolution in orange (referred to the y-axis on the right) and neutron rate time evolution in red (referred to the y-axis on the left). From' [67]'

the baseline, suggesting that neutrons contribute about three times more to the high-energy tail of the signal than to the lower-energy portion. This analysis indicates that while SXR energy information is not entirely lost in the presence of neutron background, it is partially compromised, complicating detailed spectral analysis.

Analysis of the energy spectrum for an LH mode transition

Having established the presence of neutron-related background in the GEM signal, it is important to understand under which conditions this background is significant and which data can be considered reliable.

MAST-U shot #49325 provides a clear example of the neutron background effect during NBI-heated discharges, highlighting a marked difference with Ohmic-only shots. The GEM data are interpreted by comparison with selected MAST-U diagnostics, shown in Figure 5.40. In Figure 5.40a, the plasma current (first row) reflects the overall plasma behavior, while the NBI power output (second row) indicates the heating system status. The fission chamber signal (third row) provides the total neutron emission ϵ_n over 4π, and the SXR camera current (fourth row) shows the soft X-ray emission integrated over the plasma core. Electron temperature and density measurements from the Thomson Scattering diagnostic are reported in Figure 5.40b.

In this shot, NBI heating was activated at 0.46 s, allowing the discharge to be divided into two phases. The first phase corresponds to a purely Ohmic plasma in L mode, with relatively low neutron production. The MAST-U fission chambers [78] recorded a total neutron emission rate of approximately 10^{11} n/s. Assuming isotropic emission from the tokamak center, in a zeroth-order approximation, the neutron counts incident on the

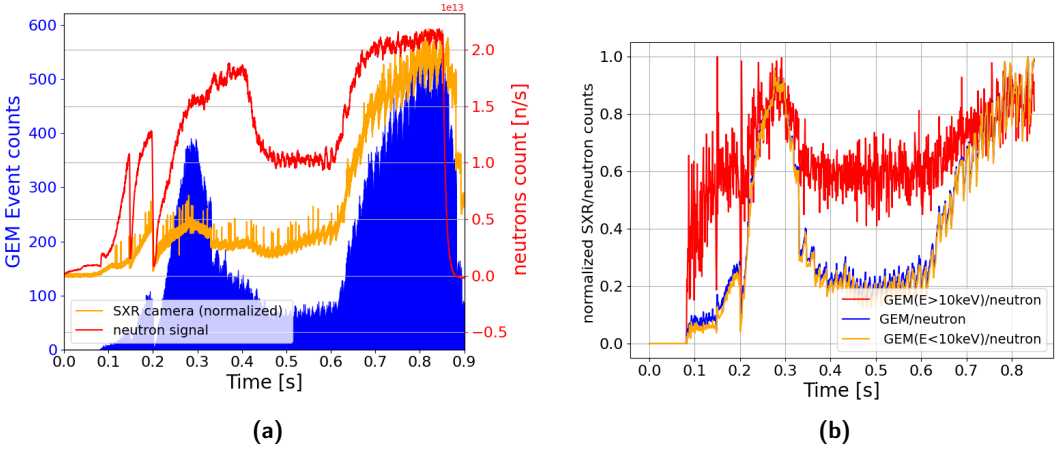

Figure 5.39: Beam heated Shot #49452. (a): GEM signal time-trace (in blue), normalized horizontal camera SXR signal (in orange), neutron rate evolution in time (in red).(b): Ratio of the GEM signal over the neutron rate signal for different energy cuts. From [67]

GEM detector can be estimated as: $\Phi_{det} \approx \frac{\epsilon_n \cdot \Omega_{det}}{4\pi} \approx 10^7 \text{n/s}$, where Ω_{det} where Ω_{det} is the solid angle subtended by the detector, calculated from its distance to the tokamak center (2.7 m) and surface area (0.1^2 m^2): $\Omega_{\text{det}} = 0.1^2/2.7^2 \approx 1.37 \times 10^{-3}$ sr.
The second phase corresponds to beam-heated plasma in H mode, where the total neutron emission increases by two orders of magnitude, giving an estimated detector flux of $\Phi_{\text{det}} \approx 10^9$ n/s. This sudden rise leads to the appearance of a high-energy tail in the GEM energy spectrogram, as illustrated in Figure 5.41a.

LH transition timetrace analysis

The GEM energy spectrogram in Figure 5.41a shows a sudden emergence of a high-energy tail, in contrast to the gradual increase observed in the SXR signal measured by the MAST-U SXR camera (Figure 5.40a). This difference arises from the intrinsic energy sensitivities of the diagnostics: the GEM system in its current configuration is sensitive to photons above 3.2 keV, whereas the diodes have a lower cut-off, around 1keV. Additionally, absorption along the diagnostic lines of sight differs: the diodes are located inside the tokamak vacuum chamber, while the GEM detector is positioned outside, resulting in a 26 cm air path that attenuates low-energy photons.
Core electron density and temperature measurements from Thomson scattering (Figure 5.40b) are used in Revolt-U to compute the core SXR emissivity at different energies and times, $\epsilon_{\text{Brem}}(E,t)$. Energy-dependent absorption along the photon path (Table 5.2) is applied to account for radiation losses.
The results, shown in Figure 5.42a, indicate that selecting GEM photons with energies below 7 keV yields a time trace that closely follows the SXR estimate. In contrast, considering only photons above 7 keV, the GEM signal aligns with the neutron emission

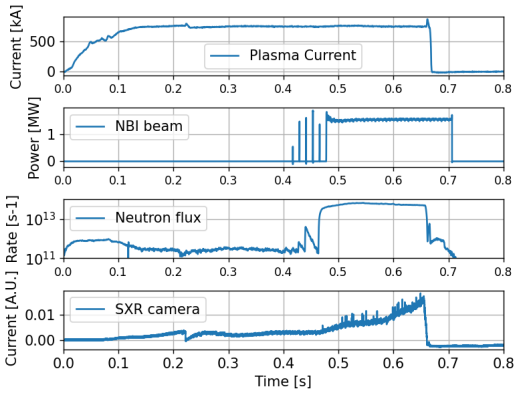

(a) Time evolution of key plasma parameters: (from top to bottom) plasma current, injected NBI power, total measured neutron emission, and SXR signal from a central chord of the MAST-U horizontal camera. From [79]

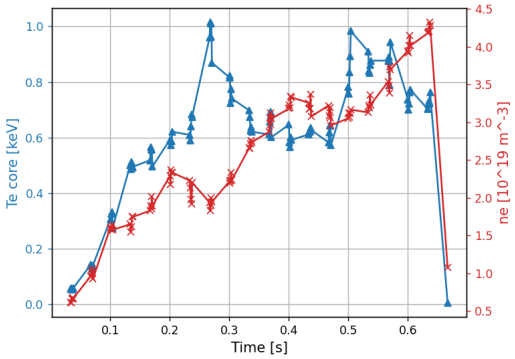

(b) Time evolution of the electron temperature and density in the core region, measured by the Thomson Scattering diagnostic.

Figure 5.40: MAST-U diagnostics data, shot #49325. From [79].

recorded by the fission chambers (Figure 5.42b). This demonstrates that neutron-related background primarily affects the high-energy portion of the spectrum, while lower-energy photons provide reliable SXR information, highlighting the potential to separate these contributions.

5.5.2 Neutron background simulation

The first-order geometrical estimate of the previous section suggests that, during an H-mode plasma, the total number of neutrons incident on the detector surface (100 cm^2) is approximately $\Phi_{det} \sim 10^9$ n/s. To assess the detector response to SXR and the impact of neutron radiation, GEANT4 simulations were performed to evaluate sensitivity to neutron-induced background and its influence on measurements. The simulation geometry was imported from the CAD model designed to integrate the GEM detector and its support structure within the MAST-U tokamak (Figure 5.5).
In experiments, SXR radiation from the extended plasma volume is collimated by the pinhole and flange system, whereas neutrons can reach the detector both directly and via scattering off tokamak components. In the simulations, these sources are modeled as particle beams originating from the plasma center. Each beam consists of $5 \cdot 10^8$ particles directed toward the detector in separate runs, with the beam cross-section larger than the tokamak flange to account for interactions within surrounding materials.
While this beam approximation accurately represents SXR radiation, it oversimplifies neutron transport, as neutrons initially emitted away from the detector may still contribute via scattering. Consequently, this approach provides only a first-order estimate of neutron-induced background. A full evaluation would require simulating a volumetric neutron source within a complete tokamak neutronic model, a task beyond the scope

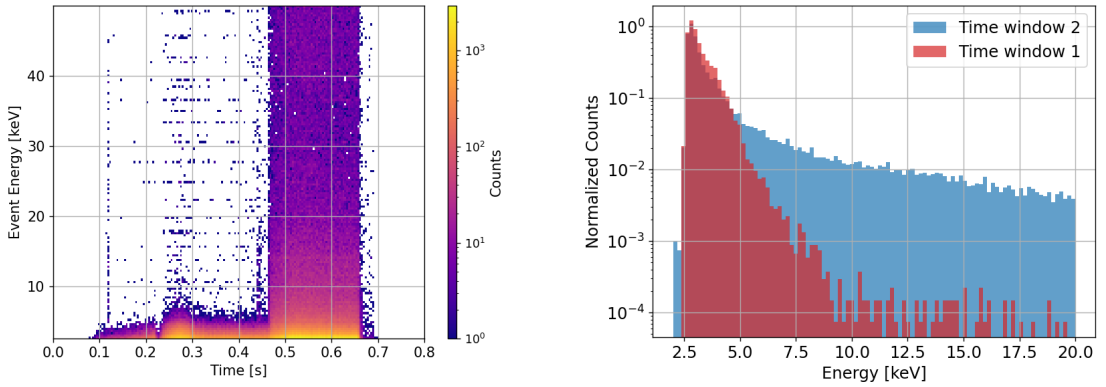

(a) Energy spectrogram obtained with the GEM detector. On the x-axis the time (time binning of 1 ms), on the y-axis the SXR energy in keV and the color proportional to the logarithmic number of events per bin. From [79]

(b) Experimental normalized energy spectra from the GEM camera in different time windows: Time window 1 (up to 0.45 sec) and Time window 2 (starting from 0.46 sec). From [79]

Figure 5.41: MAST-U shot #49325, GEM data.

of this thesis work but that could be pursued in future work and may yield valuable insights.

Neutrons in the simulations are generated at 2.45 MeV, corresponding to D-D fusion products. Energy deposition in the detector sensitive volume is tracked, along with the type of interaction and the location of particle creation, to assess signal and neutron background. Multiple physics lists are employed: "QGSP-BIC-HP" for hadronic processes, "G4IonPhysicsXS" and "G4IonElasticPhysics" for ion scattering, and "G4EmPenelopePhysics" for electromagnetic interactions. Fluorescence, Auger processes, and Particle-Induced X-ray Emission are also activated to capture photon interactions accurately.

The main results of the neutron beam simulations are shown in Figure 5.43. In the 1-20 keV energy range, the primary contributors to background energy in the GEM sensitive volume are electrons and neutrons. The electrons originate from neutron interactions with materials along their path, producing secondary γ photons that scatter via Compton processes in surrounding components, generating electrons that enter the detector. The creation volumes of these secondary gammas and electrons are illustrated in Figure 5.43b. Additional contributions come from incident gamma particles and protons generated by neutron interactions with the cathode. The "Neutrons" labeled interactions in Figure 5.43 correspond to ions produced by neutron scattering with the active gas, identified in Figure 5.44.

The simulated spectrum closely matches the GEM energy spectrum from the high-neutron region of shot #49325 (blue curve in Figure 5.41b). Both spectra are normalized to the total area, and their high-energy tails (240 keV) are fitted with an exponential function, $y = A \cdot e^{-E/\tau}$. The decay constants are consistent within uncertainties: $\tau_{\text{sim}} = 31.97 \pm 3.90$ keV and $\tau_{\text{meas}} = 27.42 \pm 1.60$ keV, as shown in Figure 5.45.

Although the exponential fits confirm statistical agreement in the high-energy tails, the

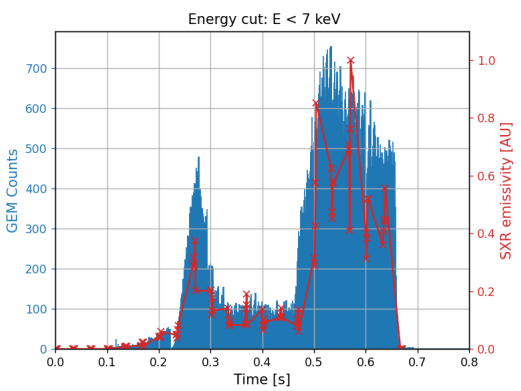

(a) Comparison between the GEM time trace, with 1 ms time binning, for energy between 3 and 7 keV (filled blue signal); and the estimated SXR emission $\epsilon_{SXR}(t)$ (red line with cruxes points).

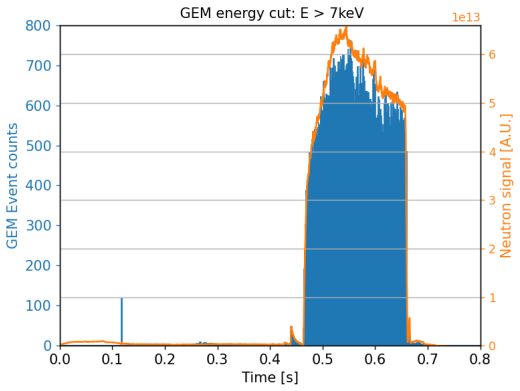

(b) Comparison between the GEM time trace, with 1 ms time binning, for energy above 7 keV (filled blue signal), and the fission chamber neutron total emission (orange curve).

Figure 5.42: MAST-U shot #49325. Comparison of GEM timetrace, estimated SXR emissivity, and fission chamber neutron total emission. From [79].

simulated spectrum exhibits a weaker high-energy component, since it accounts only for neutron-induced events, whereas the experimental spectrum includes both SXR and neutron contributions, with SXR dominating between 2.5 and 10 keV.

While this analysis focuses on the soft X-ray range, it is noteworthy that the neutron flux can produce energy deposition up to 500 keV (Figure 5.46), primarily due to protons generated by neutron interactions with plastic materials surrounding the sensitive volume. Together with the time-traces discussed in the previous section, these observations support the concept of GEM-based neutron detection for tokamak applications, as recently explored in the literature [80], although this topic lies beyond the scope of the present thesis.

Another possible approach would be to exploit different regions of the measured energy spectrum to separate the contributions of SXR photons and neutron-induced signals. In the case of MAST-U, the range above the air-filter cutoff (around 3 keV) up to roughly 20 keV contains both SXR photons and neutron-induced events, while other regions should be dominated by neutron contributions. However, several aspects of the present detector configuration may complicate such an approach.

First, the response of the detector electronics introduces distortions in the low-energy part of the spectrum. The electronics reconstruct the energy of each event using a threshold-based method. As a consequence, SXR photons with energies only slightly above the detection threshold may produce signals whose amplitudes are only marginally above this threshold. These signals can therefore be reconstructed with artificially lower energies than the true photon energy, effectively shifting some events toward the lower-energy part of the spectrum.

In addition, neutron interactions can produce secondary electrons entering the GEM

induction region (see Figure 5.43). These electrons generate signals through the same amplification mechanism as those produced by SXR photons. As a result, neutron-induced events can produce detector signals that are difficult to distinguish from those generated by SXR photons based solely on spectral and spatial information.

Consequently, the separation of SXR and neutron contributions using only GEM measurements would require a more detailed characterization of the detector response and the development of dedicated analysis techniques for the present detector configuration.

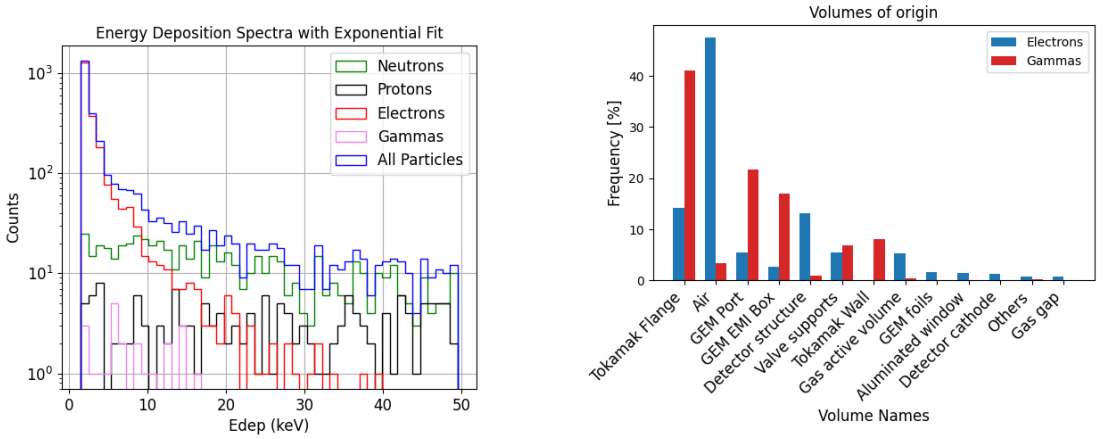

(a) Spectrum of Energy deposited in the GEM sensitive volume, divided by interacting entering particle.

(b) List of Mother Volumes of the electrons that deposit energy in the GEM detector and of the gamma particles that produce them.

Figure 5.43: Geant4 simulation of the GEM response to 2.5 MeV neutron beam in the present setup, and list of Source Volumes contributing to the GEM detector energy deposition. From [79]

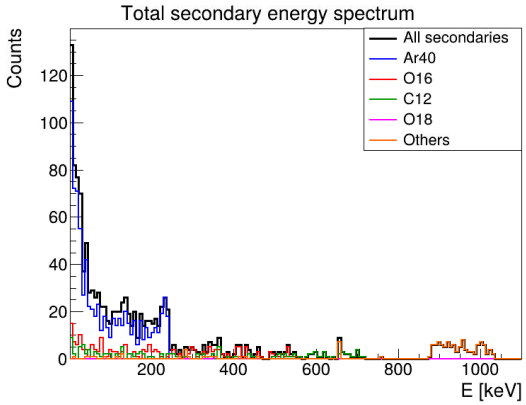

Figure 5.44: Plot of the deposited energy spectrum of particles produced by neutron interacting with the gas in the sensitive detector volume.

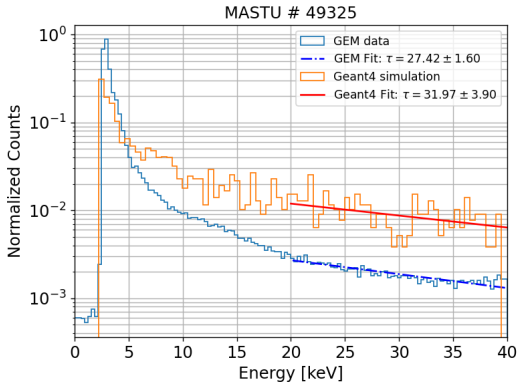

Figure 5.45: Superposition of the GEM spectrum for the MAST-U shot #49325 for t $>$ 0.46 sec, and of the Geant4 neutron simulated spectrum with corresponding fit lines. From [79]

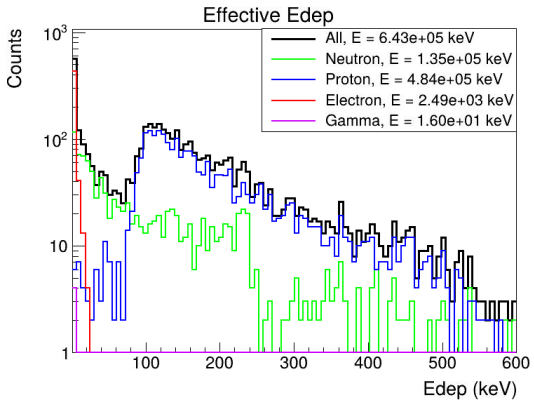

Figure 5.46: Total deposited energy spectrum from neutron flux on the detector, divided per type of interacting particle in the detector sensitive volume. Obtained from Geant4 simulation.

5.5.3 Neutron background suppression

The previous analysis identified high neutron fluxes as the primary source of background noise limiting the spectroscopic performance of the GEM diagnostic. It is essential to optimize the signal-to-noise ratio (SNR) in the $[1, 20]$ keV range to exploit the detector potential. Different strategies could be pursued: increasing the detected SXR signal, diminishing neutron signal or subtracting neutron-induced background to the SXR signal.

The latter approach would involve estimating and subtracting the neutron-induced background through detailed simulations of neutron emission and transport (e.g., using Geant4 together with an accurate CAD model of the experimental setup). However, this method would require a reliable neutronic model of the device, which is currently unavailable and is generally difficult to obtain in fusion experiments. In the absence of such information, the subtraction procedure could introduce significant systematic uncertainties and po-

tentially lead to a misinterpretation of the measured spectrum. Moreover, attempting to distinguish the neutron-induced background directly from the experimental data would also be challenging, for the reasons discussed in the previous section, where the detector response to neutron-induced events was shown to be difficult to separate from that of SXR photons based solely on the measured signals.

A different strategy involves reducing the neutron-induced background by selecting detector materials with lower neutron interaction probabilities. Preliminary simulations exploring alternative materials were performed; however, they did not lead to a significant improvement in the signal-to-noise ratio.

Within the scope of the present work, increasing the detected SXR signal and implementing effective neutron shielding are considered the most practical strategies for improving the SNR of the SXR measurements.

A possible approach to enhance the SXR rate is to put an helium buffer between the Beryllium window and the GEM window, because the absorption coefficient of helium is lower than air (see Figure 5.47) and lower the cut-off absorption energy. A similar approach has been utilized on the GEM diagnostic installed on WEST in [81], and a similar study has been performed for the design of a GEM diagnostic on RFX-mod2 [82] for the same purpose of enhancing the SXR signal. However, since in this application the detector is already operating close to its maximum sustainable count rate, the implementation of an effective neutron shielding to lower the noise is a desirable approach. To investigate suitable shielding geometries, Geant4 simulations were performed using a simplified representation of the set-up. A simplified Geant4 model, compared to the CAD-imported version, was developed for two main reason: the need to reduce computational time with a geometry wit less details, and the need to more clearly identify the dominant components responsible for the background signal. A high-fidelity simulation based on the detailed CAD model would be more accurate, but simultaneously overcomplicated for the purpose of early-stage optimization.

The simulated neutron source is a 2.5MeV neutron beam originating from the tokamak center and directed orthogonally toward the detector surface, as in the previous section. But these simulations are performed with the beam radius of 350 mm, therefore bigger than the flange and of the previous simulations series. The reason is to project more particles on the material surrounding the detector, which are possible sources of background. The objects included in the simulations are listed in Table 5.3 and illustrated in Figure 5.48. A stainless steel cylinder (of radius 2m and height 2m and 3cm thickness) is put around the diagnostic to reflect the presence of surrounding materials, because a CAD model of the tokamak hall is not available at the moment. A Concrete Box ($4 \times 4 \times 2$m) is used to simulate the wall of the tokamak hall 3m behind the detector. The GEM detector is inside the EMI box, and each of its main components (Induction gas, 3 GEM foils, transfer zones, anode etc.) are simulated.

Figure 5.49a reports the corresponding spectrum of deposited energy in the sensitive volume. A second reference simulation was performed using a different neutron-source geometry. This clarification is required because a collimated beam may not faithfully represent the neutron emission of the tokamak plasma, which is multidirectional and ap-

proximately isotropic. Therefore, an additional simulation was run using a point source emitting in a cone of 45 deg in the detector direction of the detector. The corresponding results are given in Figure 5.49b. The comparison shows that the total number of particles depositing energy is different by a factor 2, whereas the distributions of deposited energies and the spatial origins of particle production remain broadly consistent across the two source models. This supports the use of the beam-source approximation for computationally efficient optimization studies. Nonetheless, it is important to acknowledge that the conclusions of this section may be influenced by the simplified nature of the geometry.

Multiple shielding concepts were evaluated and compared based on the number of entering particles and their deposited-energy distribution. The primary shielding materials tested were borated polyethylene (BPE), due to its high hydrogen content and neutron-absorption capability via boron capture, and lead. Any shielding concept must remain compatible with the practical constraints of the system: the added material must not excessively alter the mechanical layout, must remain installable in the tokamak environment, and must preserve the compactness of the diagnostic. These constraints naturally exclude very heavy or bulky shielding solutions. The best scenario, from the simulation outputs, appears to be a Cone layered structure placed at the end of the GEM port, substituting the plastic nose. In this simulation (Figure 5.51a) is composed by 4 couples of alternating layers of borated polyethylene (1cm of thickness) and lead (6mm of thickness), with a length of 25cm, small base radius of 6.5mm and large base radius of 7cm (to enclose the window of the EMIbox in front of the detector window) for approximately 32 kg. Figures 5.51b shows the resulting spectrum and Figure 5.51c the origin of the entering electrons and the parents γ. The shield produces an attenuation of a factor 2, by taking the integrated energy in the range $[1, 20]$keV for the simulation with the shielding (221 keV deposited) and without the shielding (446 keV deposited). These results indicate that a compact, layered cone shield can significantly mitigate neutron-induced background while remaining compatible with the diagnostic mechanical constraints, making it a promising solution for future experimental campaigns.

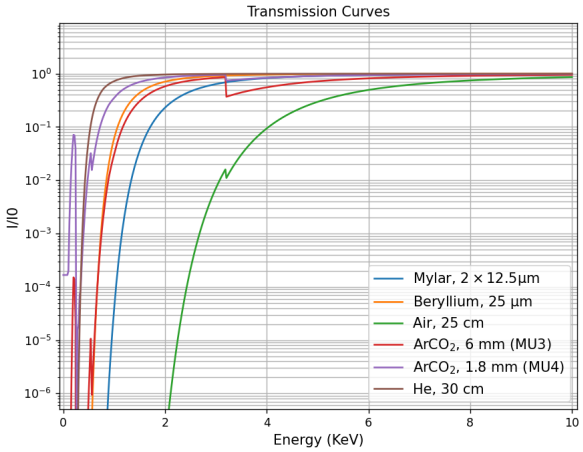

Figure 5.47: SXR Transmission curves for Air and Helium over 30cm length. The other media on the SXR path of the MAST-U installation are also shown for comparison

Surrounding Element	Material	Geant4 Volume	Color
Tokamak Inner Wall	Stainless steel	Tube	White
Tokamak Outer Wall	Stainless steel	Tube	White
Tokamak flange	Stainless steel	Tube	Blue
Tokamak flange base	Stainless steel	Cylinder	Green
GEM port	Stainless steel	Tube	Blue
GEM port ending	Stainless steel	Cylinder	Green
Plastic nose	Plastic (PLA)	Tube	White
GEM EMI box	Aluminum	Multiple boxes	White
Detector structure	FR4	Boxes	N.V.
Wall	Concrete	Box	Yellow
Surrounding Cylinder	Stainless steel	Tube	Blue

Table 5.3: Main components of the simulation for the study of neutron shielding. Materials, simulation volumes, and corresponding color in Figure 5.48. N.V. stands for Not Visible in Figure 5.48.

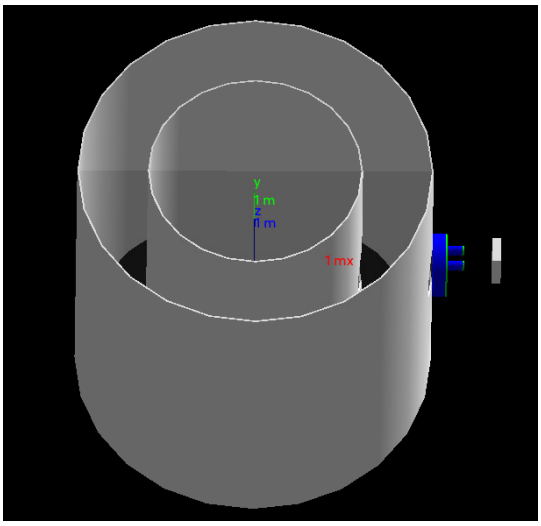

(a) Simplified simulation geometry, without the surrounding cylinder and the wall behind the detector for visualization purpose.

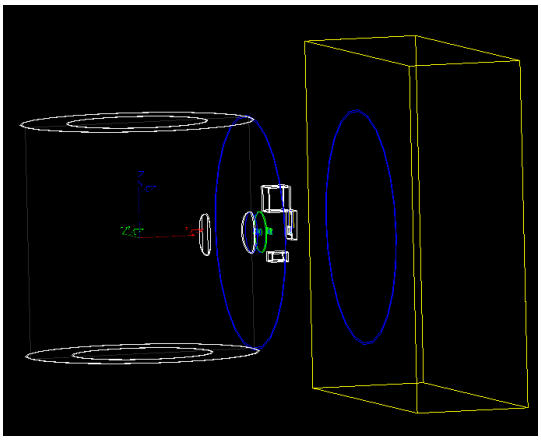

(b) Simulation geometry, complete of wall and surrounding cylinder.

Figure 5.48: Image of the simulation used to design the neutron shielding.

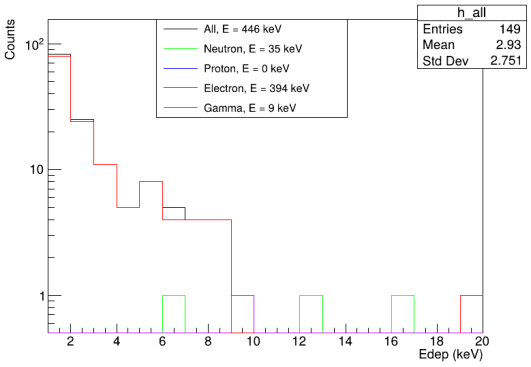

(a) Reference simplified simulation with beam source.

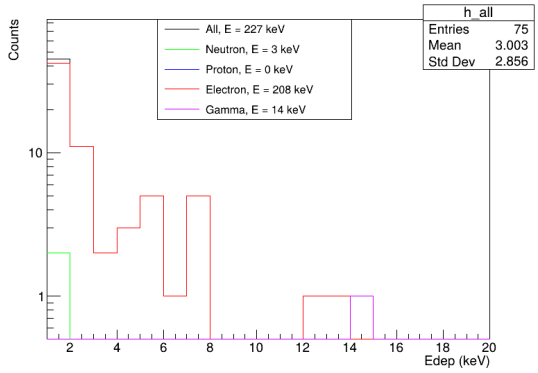

(b) Reference spectrum from an isotropic point source.

Figure 5.49: Spectrum of Energy deposited in the GEM sensitive volume, divided by interacting entering particle.

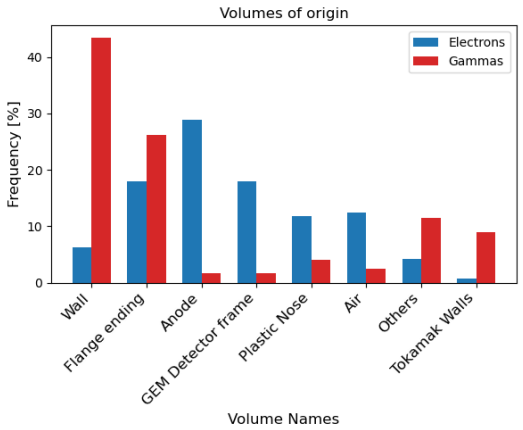

(a) Reference simplified simulation with beam source.

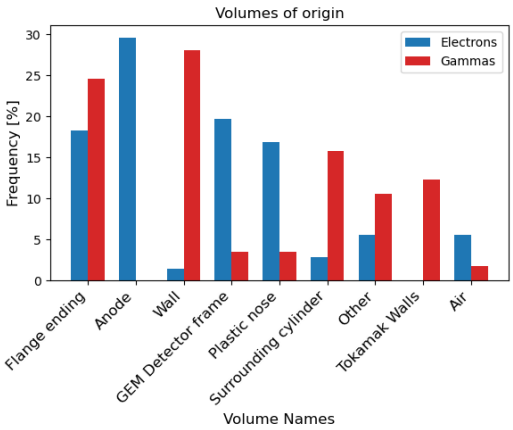

(b) Reference simplified simulation from an isotropic point source. Other

Figure 5.50: List of Mother Volumes of the electrons that deposit energy in the GEM detector and of the γ particles that produce them

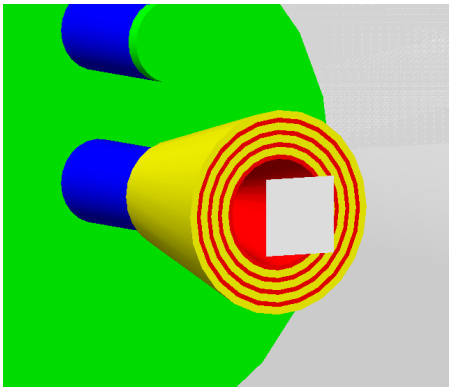

(a) Image of the simulated cone structured shield.

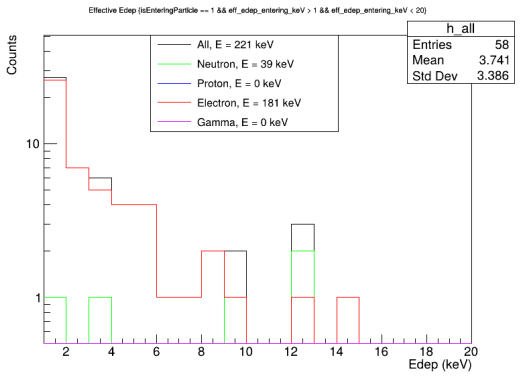

(b) Deposited energy spectrum.

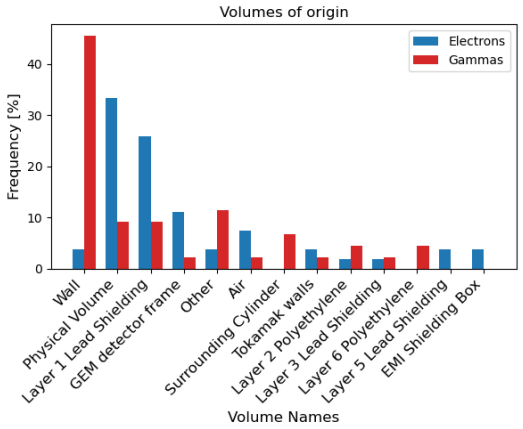

(c) List of Mother Volumes of the electrons that deposit energy in the GEM detector and of the γ particles that produce them

Figure 5.51: Simulation of the cone structured shielding.

Chapter 6

Conclusions and Outlook

This thesis presented the application of two advanced radiation diagnostics for fusion plasmas, with the goal of integrating time, energy and space-resolved measurements into compact systems. The work focused on a GEM-based detector equipped with GEMINI electronics for soft X-ray (SXR) measurements on MAST-U, and on an optimization study for a diamond-based Neutron Camera for SPARC.

Chapter 3 introduced Revolt-U, a geometrical transport code developed as part of this work. It is used to produce synthetic data for both the design phase and data interpretation, and to generate transport matrices for tomographic inversion techniques. Revolt-U computes line-of-sight visibility, including shading effects, using a hit-or-miss Monte Carlo approach, and evaluates SXR absorption along the path as well as detector efficiency based on analytical models and tabulated material data, enabling an estimate of the incident emission spectrum. Revolt-U has been benchmarked against established numerical tools as well as experimental SXR measurements on tokamaks, showing satisfactory agreement. The development of Revolt-U remains ongoing: one possible future upgrade is the inclusion of a GEM detector response model, incorporating primary ionization and charge multiplication to reproduce energy resolution effects.

Chapter 4 presented an optimization study of the SPARC Neutron Camera based on single-crystal diamond detectors. The study shows that reliable ion temperature reconstructions can be achieved using a limited number of strategically arranged lines of sight and detectors. Two minimum-viable configurations have been identified, one suitable for the first DT campaign and one capable of supporting up to the full-power DT scenario. A reconstruction routine for ion temperature in thermal plasmas was developed and tested, confirming the feasibility of neutron-based diagnostics in reactor-relevant conditions. Furthermore, these results establish a foundation for using the Neutron Camera to infer fusion power output on SPARC. To move in this direction, two key steps are required: accurate calibration and characterization of the employed diamond detectors, and comprehensive neutronic simulations of the system.

Chapter 5 described the installation and exploitation of a GEM-based SXR camera on MAST-U. This represents two notable firsts: the first deployment of a GEM diagnostic on a spherical tokamak, and the first installation of a GEM with GEMINI electronics on

a tokamak, enabling coarse spectroscopic measurements. Benchmarking of the detector against the existing diode-based SXR camera showed good agreement in temporal traces and spatial profiles. Moreover, the GEM demonstrated potential for spectroscopic analysis of plasma radiation, yielding encouraging results for electron temperature estimation. A tomographic reconstruction of tangential SXR measurements was also performed, successfully recovering plasma position. Although further improvements in pixel uniformity will be essential to fully exploit the diagnostic for tomographic inversion of MHD-related plasma instabilities.

The investigation of neutron background effects highlighted the need to optimize the detector for improved signal-to-noise ratio and clearer spectral measurements. While high neutron emission levels $\sim 10^9$n/s incident neutron rate on the detector reduce spectroscopic performance, the impact on photon-counting capability is limited and can be mitigated through offline energy-threshold filtering. To further suppress neutron-induced background, a shielding strategy consisting of a layered borated polyethylene and lead cone has been proposed. Future work will expand this study to improve the GEM diagnostic performance in neutron-rich tokamak environments.

Appendix A

GEM Detector Characterization and Calibration

This chapter outlines the procedure used to characterize and calibrate the GEM detectors employed in this work. The goal is to identify the optimal operating conditions for the detectors and to determine, for each GEMINI channel, the conversion function that maps the measured Time-over-Threshold (ToT) to the corresponding energy. Three main elements require dedicated investigation:

- Determining the threshold voltage (THR) used to generate the ToT signals.
- Identifying the operational interval of the total voltage (HV) applied across the GEM foils, which sets the detector gain.
- Extracting the parameters of the function used to convert ToT measurements into energy values.

To study these aspects, two complementary procedures are carried out, namely the Threshold scan (THR scan) and the High Voltage scan (HV scan). In both cases, the detector records a known x-ray fluorescence spectrum while one operational parameter is varied systematically.
The fluorescence spectrum is produced by irradiating a metallic target (Titanium, in our case) with bremsstrahlung x-rays. The resulting spectrum contains a prominent K_α line at 4.5 keV alongside a background component arising from x-ray excitation of surrounding materials.
During the THR scan, the comparator threshold of each pad is swept between 40 and 300 LSB, and the observable is the event rate as a function of threshold. In the HV scan, the voltage applied to the GEM stack is varied between 950 and 1140 V. Two types of information are collected: the event rate at each voltage setting, and the ToT spectra of every pad for each voltage point. These ToT spectra form the basis for the calibration procedure.

A.1 Experimental set-up

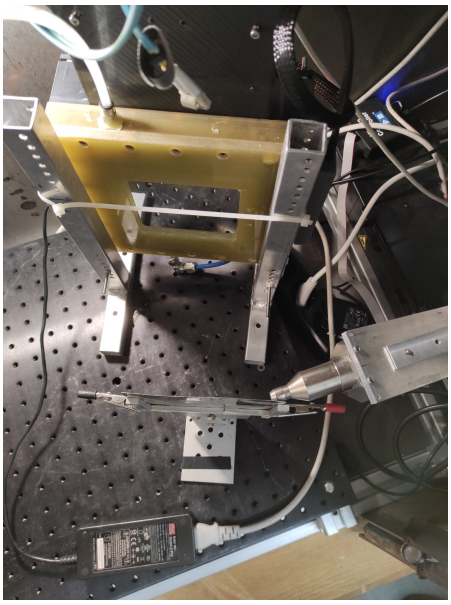

Figure A.1: Set-up, with the detector in position for measurements.

- **Iron enclosure:** The X-ray source and the detector are housed inside an iron shielding box to ensure adequate radiation protection for the laboratory environment.
- **X-ray tube:** The radiation source is a compact X-ray tube in which thermionic electrons are accelerated by a controllable high voltage and impinge on a gold (Au) target. The interaction produces a continuous bremsstrahlung spectrum together with characteristic Au X-ray lines when the electron energy exceeds the corresponding binding energies. The emitted radiation is extracted as a collimated beam with a diameter of about 2 mm. The tube voltage determines the maximum photon energy and spectral shape, while the tube current controls the photon flux and hence the detector counting rate. [83]
- **Metal targets:** The X-ray beam is directed onto metallic samples, which then emit fluorescence isotropically. Three targets are used: Titanium for the THR and HV scans, and Copper and Molybdenum for performance tests. Each material produces a characteristic K_α line at a distinct energy.
- **HV-GEM system:** The potentials applied to the three GEM foils and the cathode are controlled independently through a custom high-voltage module (HVGEM). The anode is held at ground, and each subsequent electrode is biased relative to the previous one. This configuration allows independent tuning of the drift, transfer, and induction fields via remote control.

- **Gas flow system:** The detector gas mixture is remotely regulated and maintained at 70% Argon and 30% CO_2, at atmospheric pressure, with a stable flow rate of 5 l/h.
- **Detector positioning:** The 2D GEM detector is placed at an angle of 45° with respect to the X-ray beam, as shown in the setup figure. This orientation ensures that the detector records only the fluorescence emission from the target material and not the primary X-ray beam.

A.2 THR scan

The energy related information output of the detector is the Time over Threshold (ToT): the time during which the input current on the anode, converted into a voltage signal, is greater than a threshold V_{th}. The THR scan aims to find the suitable V_{th} value: lowering the threshold value results in shifting to higher ToT a fixed energy input detected, and vice versa. An example of THR scan is illustrated in Figure A.2. The signal analyzed is the fluorescence peak of titanium at 4.5 keV, and the meaningful information is the rate of event.
Three regimes can be individuated:

1. If the threshold is set too low, a significant amount of noise, electronic or background radiation, is recorded, leading to an artificially high event rate.
2. Within a suitable range (in this case, 60-150 LSB), the detector rate reaches a plateau: noise is largely suppressed, and soft X-rays are detected with minimal loss. This defines the operational regime of the detector.
3. If the threshold is too high, a fraction of the signal falls below V_{th}, causing the detector to miss events and resulting in a reduced rate.

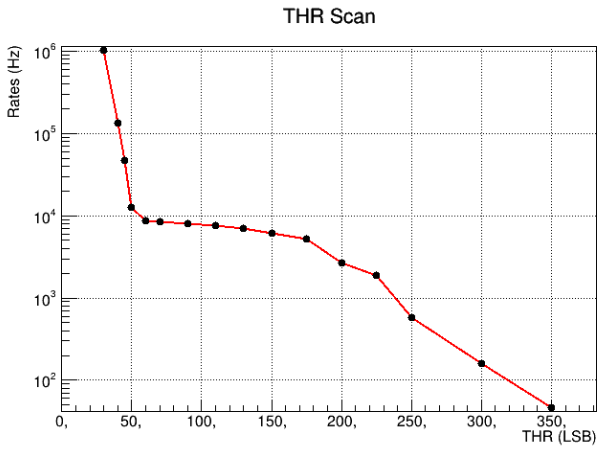

Figure A.2: THR scan produced with titanium fluorescence, and a total HV of 1065 V on the GEMs.

To better understand the three regimes, some spectra produced by the detector are shown in FIgure A.3. The THR scan shows that a threshold of 70 LSB is a conservative value to work with, given the fact that is already in the plateau zone, far from the region where data are lost.

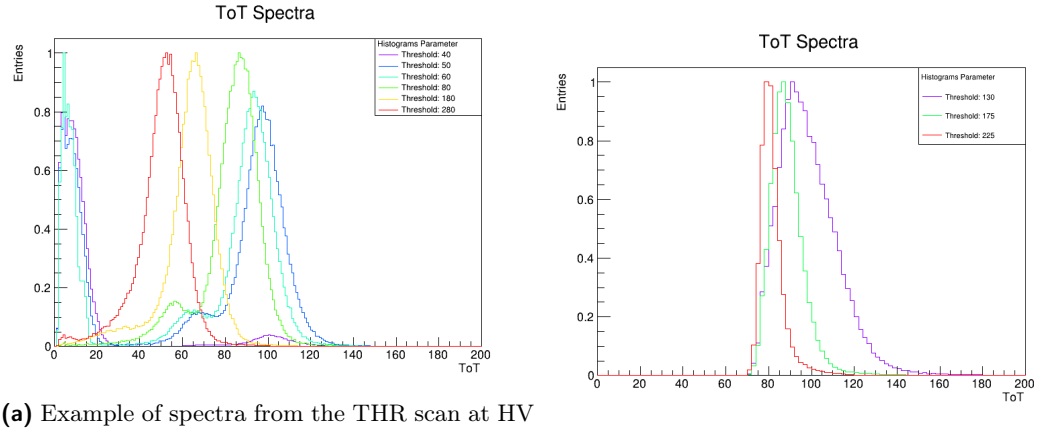

(a) Example of spectra from the THR scan at HV = 1110 V (each spectrum normalized to its maximum bin). The histograms obtained with low thresholds (< 60 LSB) are affected by low ToT present the expected shape (main peak + escape).

(b) Example spectra from the THR scan at HV = 1065 V (each normalized to its maximum bin). As the applied threshold increases, part of the signal noise. As the applied threshold grows the spectra is lost, causing the peak to deviate from its Gaussian shape.

Figure A.3: Example of spectra (integrate over the wole detector) from THR scans.

A.3 HV scan

As already stated, the aim of the HV scan is to define an operational range in term of total Voltage applied to the GEM foils. Moreover it will be used for the calibration as well.
The HV scan consists in taking different measurements of the same signal varying the Voltage applied to the GEM foils. From these, the average rates of events will be found. The results are shown in Figure A.4:

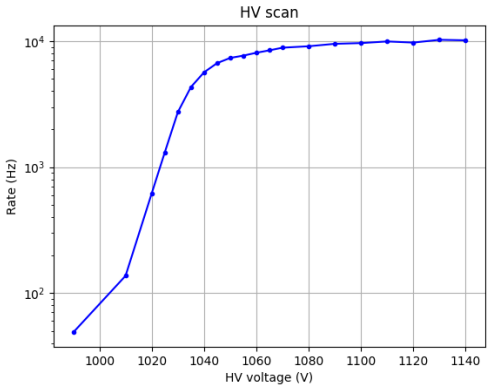

Figure A.4: HV scan with titanium fluorescence. Volts on the *x-axis* indicate the total potential difference applied to the GEMs. The parameters of the x-ray gun are Vx = 10 kV (x-ray voltage) and Ix = 100 μA (x-ray current).

The lower operational limit is given by the beginning of the plateau zone: over a certain value of voltage, the rate of events read by the electronic is steady. This means that all the electrons produced by the photon-gas interaction have reached the anode, which is the condition for not losing information.
The upper operational limit is given by the stability of the GEM foils themselves. If an excessive voltage is applied to a GEM, the detector behavior is not stable: the detector might acquire noise signal, and discharges might start and burn (up to break completely) the detector. This upper limit is not visible from the rate, but during the operation it is found to be 1150 V.

A.4 Calibration

The ToT signal, output of the GEMINI ASIC, has to be translated into a deposited energy signal through a calibration. An intermediate step is to convert the ToT into charge read by the anode, and then convert charge into energy.
This has to be done for every pad separately: even though the pads are produced to behave equally, every GEM + GEMINI system behave slightly differently due to unavoidable production issues.

The calibration is done with the same acquisitions of the HV scan. Varying the voltage of the GEMs, the gain of the detector changes. Therefore a known energy x-ray beam is used as energy point of reference, then the total voltage applied to the GEMs is varied in a range from 1040 V to 1140 V. With this method an empirical relation between energy (as input current signal) and ToT is found. In the voltage range of the plateau found with the HV scan the behavior is of a proportional gaseous detector: the ToT produced by the GEMINI comparator is proportional to the charge. With signals close to the voltage

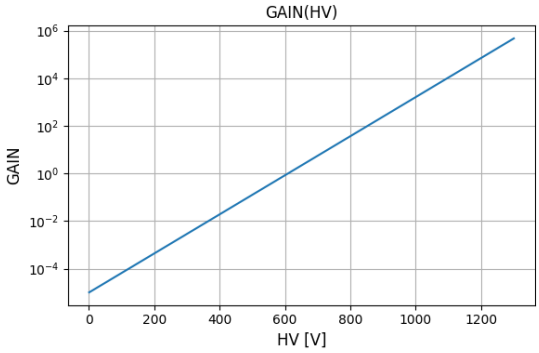

Figure A.5: Relation between the detector Gain and total HV applied on the 3 GEM foils.

threshold the relation deviate from linear, until the function $ToT(q)$ reach a vertical asymptote related to the threshold. The relation is given by Equation A.1.

$$ToT = a + bq - \frac{c}{q - Thr} \tag{A.1}$$

Where the q stands for the input charge, which depends on the total voltage applied. This charge is found analytically with Equation (A.2), because the energy of the K_α line is fixed for a known sample material. The detector gain corresponding to any applied high voltage is known from previous measurements that relate the total potential to the resulting gain, as shown in Figure A.5.

$$q(K_\alpha energy) = Gain \cdot \frac{K_\alpha}{W_i} \cdot 1.6 \cdot 10^{-19} C \tag{A.2}$$

Where W_i is the average energy needed to create and electron-ion pair, which takes into account not only ionization process, but recombination as well, and correspond to 28 eV for the $ArCO_2$ gas mixture used.

Using a known fluorescence target, in our case Titanium, the peak of the K_α line is the point of reference. After the acquisition, for every single pad the ToT spectrum of every single run (acquisition, at a certain Voltage) is fitted to obtain the position of the K_α peak, as in Figure A.6.

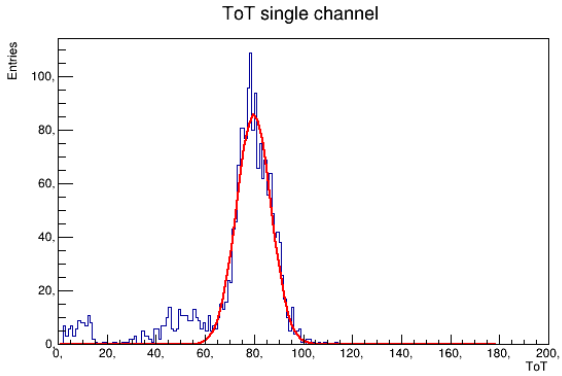

Figure A.6: ToT spectrum of a single pad for the Calibration $V_{GEM} = V_{GEM1}+V_{GEM2}+V_{GEM3} = 1100$.

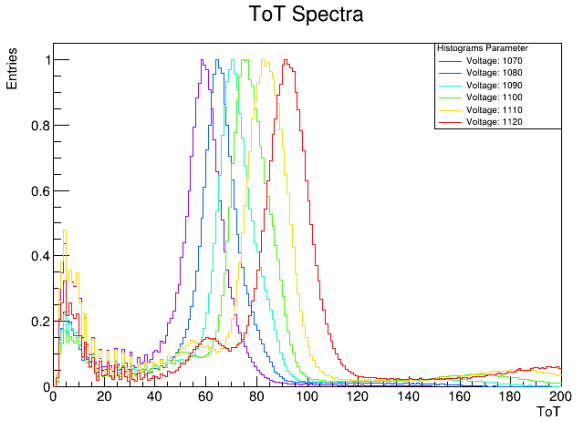

Figure A.7: Normalized ToT spectra of the calibration with the titanium fluorescence.

The shift in the ToT position of the peak is visible plotting the spectra (normalized with reference to the maximum) as shown in Figure A.7. Another remarkable feature is visible: a low ToT noise grows with the gain. This feature will be projected at low energy by the conversion in charge itself given the steepness of the curves at low ToT. Moreover a software filter can be applied manually removing the counts at energy less than 1 keV (energy value under which the information is not interesting for the application of the detector).

Fitting the $ToT(q)$ function A.1 over the points obtained the parameters are found for every pad. An example of the curve is presented A.8:

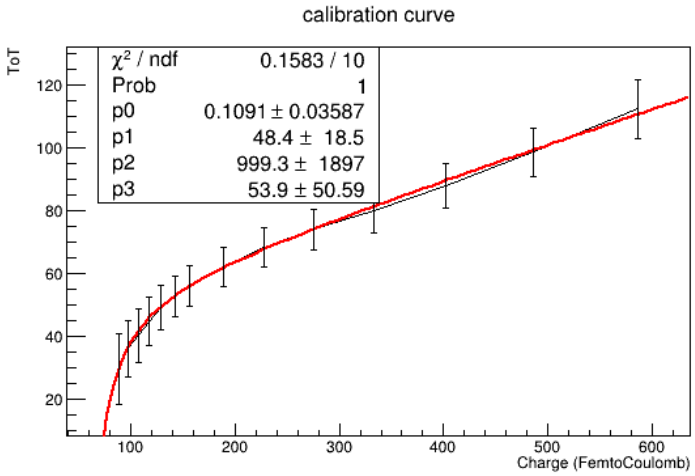

Figure A.8: Example of a calibration Curve from the HV-Scan calibration.

Once the parameters are found the function is inverted in order to obtain a function $q(ToT)$. The function is inverted in the region after the asymptote $q > THR$:

$$q = \frac{-a + b * THR + ToT + \sqrt{4b(ad + c - d * ToT) + (-a + bTHR + ToT)^2}}{2b} \tag{A.3}$$

After the calibration is completed for the configuration of Thr = 70 LSB, the ToT signals can be converted directly into charge information. Subsequently, solving Equation A.2 for the K_α line, that now stands for the energy to be found, the charge information is converted into an energy spectrum.
The formula for the Energy from the charge read by detector is:

$$E(keV) = \frac{q \cdot W_i}{Gain \cdot 1.6 \cdot 10^{-19}}. \tag{A.4}$$

A.5 Calibration testing

The fluorescence spectra from known sources are studied once the calibration is done in order to assess the detector energy resolution. The testing setup is exactly as the one discussed for the calibration, with the only difference that the used targets are Copper and Molybdenum.

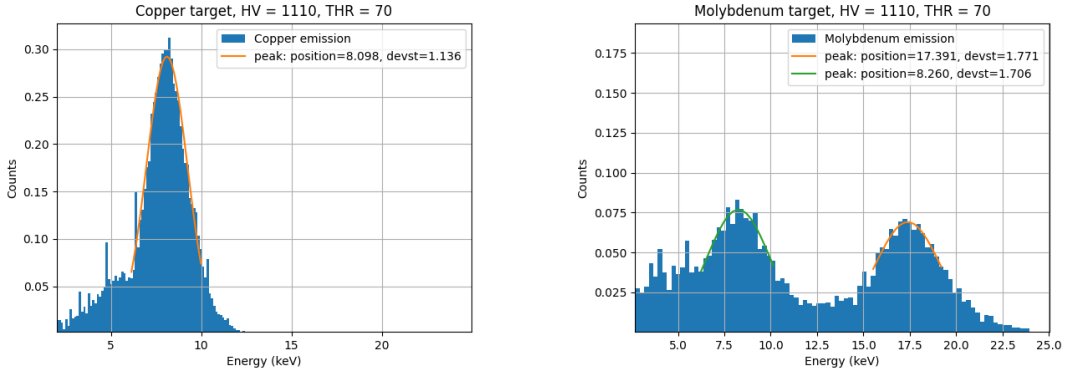

(a) Copper target

(b) Molybdenum target

Figure A.9: Energy spectra of fluorescence signal.

The analysis of the Copper fluorescence spectrum shows a main peak associated with the Cu K_α line, measured at 8.09 ± 1.36 keV. This corresponds to an energy resolution, defined as the ratio between the Full Width at Half Maximum (FWHM) and the peak energy, of about 30%, which is consistent with the expected performance of this detector class. A secondary feature is also visible: the escape peak, which, as expected from the gas mixture properties, appears around $8.2 - 2.95 \approx 5.4$ keV.
The spectrum obtained with the molybdenum target exhibits a background together with two prominent peaks. The first peak, at roughly 17.4 keV, corresponds to the Mo K_α fluorescence line. The second peak, near 8 keV, originates from Copper fluorescence induced in surrounding materials (e.g., detector structural components, readout electronics, or nearby chamber elements). This constitutes an unwanted background, as it overlaps with the useful signal and should ideally be minimized to ensure a clean spectral measurement.
The background arises from multiple mechanisms:

- Fluorescence from iron, due to excitation of the shielding cage.
- Fluorescence from copper components present in or around the detector.
- Bremsstrahlung produced when the primary X-ray beam interacts with the target.

The relative intensity of the copper-background peak is further accentuated by the non-uniform detection efficiency of the GEM system. Since the stopping power of the gas mixture decreases with photon energy, the detector is intrinsically more efficient at lower energies. A software correction can be applied to compensate for this effect, using tabulated attenuation coefficients. The correction consists of multiplying the counts at each energy by:

$$\text{correction}(E) = \frac{1}{\text{efficiency}(E)} = \frac{1}{1 - e^{-\mu(E), l_D}}, \tag{A.5}$$

where $\mu(E)$ is the energy-dependent attenuation coefficient of the working gas and l_D is the drift gap thickness. This correction, illustrated in Figure A.10, significantly reshapes the lower-energy portion of the spectrum: the copper peak is reduced while the molybdenum peak becomes more dominant, yielding a more realistic representation of the true photon distribution.

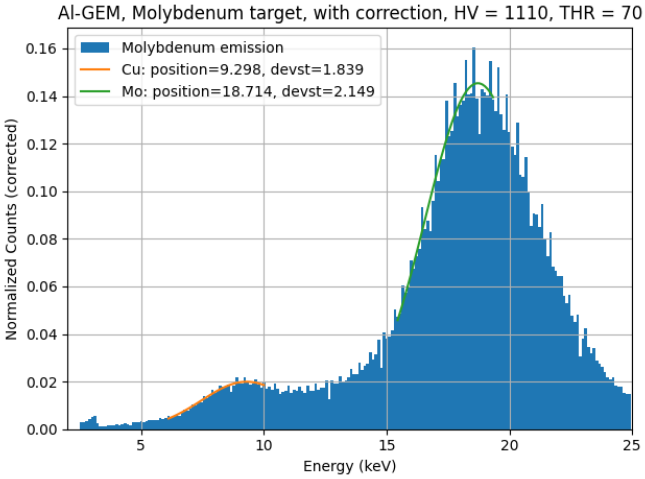

Figure A.10: Energy spectrum of molybdenum fluorescence peak, corrected for the detector efficiency.

List of Publications

- Celora A, Guiotto F, Caruggi F, Cancelli S, Claps G, Cordella F, de Leo V, Garzotti L, Grosso G, Lazzaro E, Pacella D, Putignano O, Rose E, Sarwar R, Scannell R, Tardocchi M, Croci G, Muraro A, MAST-U Team. (2025). Analysis of neutron related background of the SXR GEM diagnostic on MAST-U. *Journal of Instrumentation*, 20(05), C05010. doi:10.1088/1748-0221/20/05/C05010

- Celora A, Caruggi F, Putignano O, Cancelli S, Claps G, et al. (2025). Assessment of a space and energy resolved diagnostic based on GEM technology on MAST-U. *Measurement Science and Technology*, 36(1). doi:10.1088/1361-6501/ad8cfb

- Celora A, Guiotto F, Caruggi F, Croci G, Gorini G, et al. (2024). A multipurpose numerical method for imaging studies and tomographic reconstruction. *Journal of Instrumentation*, 19(03), C03032. doi:10.1088/1748-0221/19/03/C03032

- Guiotto F, Putignano O, Dal Molin A, Croci G, Franz P, Zuin M, Orlandi L, Celora A, Celora, et al. (2026). Development of a GEM based diagnostic for Soft X-ray measurements resolved in space, time, and energy at RFX-mod2. *Plasma Physics and Controlled Fusion*. doi: https://doi.org/10.1088/1361-6587/ae26c6

- Guiotto F, Celora A, Croci G, Putignano O, Caruggi F, Dal Molin A, ... and Muraro A. (2025). REVOLT-Upgrade: a software tool for fast, energy-resolved simulations of Soft X-ray detectors in Nuclear Fusion experiments. *Measurement Science and Technology*.

- Ball JL, Mackie SP, Panontin E, Wang X, Raj P, Gocht R, ... and Tinguely RA. (2025, November). Prototyping activities supporting the design of a spectrometric neutron camera for SPARC. In DPP 2025.

- Caruggi F, Croci G, Cancelli S, Celora A, De Lorenzi A, et al. (2025). Analysis of micro-discharges fine dynamics via X-ray detection on the high voltage Padova test facility experiment. *High Voltage*, 10(4), 1043–1052. doi:10.1049/hve2.70042

- Gatu Johnson M, Schlossberg D, Appelbe B, Ball J, Bitter M, et al. (2024). Learning from each other: Cross-cutting diagnostic development activities between magnetic and inertial confinement fusion (invited). *Review of Scientific Instruments*, 95(9). doi:10.1063/5.0218498

- Caruggi F, Celora A, Cancelli S, Gorini G, Grosso G, et al. (2024). Development of a triple-GEM detector with strip readout and GEMINI chip for X-rays and neutron imaging. *Journal of Instrumentation*, 19(02), C02015. doi:10.1088/1748-0221/19/02/C02015

- Petruzzo M, Celora A, Croci G, Gallo E, Gorini G, et al. (2024). Design studies on electronics and data acquisition of a real-time diamond spectrometer for the SPARC neutron camera. *Review of Scientific Instruments*, 95(11). doi:10.1063/5.0219537

- Guiotto F, Caruggi F, Celora A, Croci G, Pilan N, et al. (2024). Data analysis and tomographic reconstruction via X-ray measurements with a GEM detector at the high-voltage Padova test facility. *IEEE Transactions on Plasma Science*, 52(9), 4450–4461. doi:10.1109/TPS.2024.3406776

- Cancelli S, Caruggi F, Perelli Cippo E, Putignano O, Celora A, et al. (2024). Development of a multi-layer high-efficiency GEM-based neutron detector for spallation sources. *Scientific Reports*, 14(1). doi:10.1038/s41598-024-74958-5

- Caruggi F, Cancelli S, Celora A, Guiotto F, Croci G, et al. (2023). Performance of a triple GEM detector equipped with Al-GEM foils for X-rays detection. *Nuclear Instruments and Methods in Physics Research A*, 1047, 167855. doi:10.1016/j.nima.2022.167855

- Caruggi F, Croci G, De Lorenzi A, Grosso G, Guiotto F, Celora A et al. (2023). Development of a data analysis software for the XR-GEM installed at HVPTF and preliminary results. In *Proceedings of the International Symposium on Discharges and Electrical Insulation in Vacuum (ISDEIV)*, pp. 29–32. doi:10.23919/ISDEIV55268.2023.10199827

Bibliography

[1] Intergovernmental Panel on Climate Change (IPCC). Summary for policymakers. in: Climate change 2023: Synthesis report. contribution of working groups i, ii and iii to the sixth assessment report of the intergovernmental panel on climate change, 2023.

[2] Encyclopædia Britannica, Inc. Nuclear binding energies, n.d. Image. Accessed: 3 March 2026.

[3] Jeffrey P Freidberg. *Plasma physics and fusion energy*. Cambridge university press, 2008.

[4] Jef Ongena. Fusion: A true challenge for an enormous reward. *EPJ Web of Conferences*, 98:05004, 01 2015.

[5] R. HAGEMANN, G. NIEF, and E. ROTH. Absolute isotopic scale for deuterium analysis of natural waters. absolute d/h ratio for smow. *Tellus*, 22(6):712–715, 1970.

[6] Abu-Shawareb et al. Lawson criterion for ignition exceeded in an inertial fusion experiment. *Phys. Rev. Lett.*, 129:075001, Aug 2022.

[7] L A Artsimovitch. Plasma in the tokamak, Jan 1972.

[8] ITER Organization. Image from "searching for the perfect shape". `https://www.iter.org/node/20687/searching-perfect-shape`, 2018. Photograph downloaded and reproduced by the author from the ITER website. The image illustrates toroidal magnetic field lines and magnetic trap concepts in fusion research.

[9] M Keilhacker, A Gibson, C Gormezano, PJ Lomas, PR Thomas, ML Watkins, P Andrew, B Balet, D Borba, CD Challis, et al. High fusion performance from deuterium-tritium plasmas in jet. *Nuclear Fusion*, 39(2):209, 1999.

[10] ITER. What is iter?, 2022.

[11] Y. Wan et al. The china fusion engineering test reactor (cfetr) program. *Nuclear Fusion*, 57(10), 2017.

[12] M. Greenwald et al. The sparc tokamak: A compact, high-field path to fusion energy. *Journal of Plasma Physics*, 86(5), 2020.

[13] H. Zohm. On the size of tokamak fusion power plants. *Philosophical Transactions of the Royal Society A*, 377(2153):20170437, 2019.

[14] Alexander Creely, Martin Greenwald, Sean Ballinger, D. Brunner, J. Canik, Jeffrey Doody, T. Fülöp, Darren Garnier, Robert Granetz, Travis Gray, Caitlin Holland, N. Howard, J. Hughes, James Irby, Viviana Izzo, Gerrit Kramer, Adam Kuang, Brian Labombard, Y. Lin, and Jinxiang Zhu. Overview of the sparc tokamak. *Journal of Plasma Physics*, 86, 09 2020.

[15] Hartwig et al. The sparc toroidal field model coil program. *IEEE Transactions on Applied Superconductivity*, 34(2):1–16, 2024.

[16] A. Sykes, R.J. Akers, and contributors. Mast: Results from a mega-amp spherical tokamak. *Plasma Physics and Controlled Fusion*, 43:A195–A207, 2001.

[17] M. Valovic and contributors. Performance of the super-x divertor in mast. *Nuclear Fusion*, 55(5):053025, 2015.

[18] J.R. Harrison and contributors. Overview of physics results from mast and mast-upgrade. *Nuclear Fusion*, 59(11):112011, 2019.

[19] S. Von Goeler et al. Thermal x-ray spectra and impurities in the st tokamak. *Nuclear Fusion*, 15(2):301, apr 1975.

[20] I. H. Hutchinson. *Principles of Plasma Diagnostics*. Cambridge university press, 2009.

[21] L F Delgado-Aparicio, Dan Stutman, Kevin Lee Tritz, Robert Vero, Michael Finkenthal, G. Suliman, Robert Kaita, R. Majeski, Brentley Stratton, Lane Roquemore, and Charles Tarrio. High-efficiency fast scintillators for "optical" soft x-ray arrays for laboratory plasma diagnostics. *Applied optics*, 46 24:6069–75, 2007.

[22] M. Angelone, M. Pillon, Marco Marinelli, E. Milani, G. Prestopino, C. Verona, G. Verona-Rinati, I. Coffey, A. Murari, and N. Tartoni. Single crystal artificial diamond detectors for vuv and soft x-rays measurements on jet thermonuclear fusion plasma. *Nuclear Instruments and Methods in Physics Research Section A: Accelerators, Spectrometers, Detectors and Associated Equipment*, 623(2):726–730, 2010. 1rs International Conference on Frontiers in Diagnostics Technologies.

[23] Didier Mazon, M Chernyshova, Axel Jardin, Y Peysson, K Król, Philippe Malard, Tomasz Czarski, Andrzej Wojeński, Karol Malinowski, D Colette, et al. First gem measurements at west and perspectives for fast electrons and heavy impurities transport studies in tokamaks. *Journal of Instrumentation*, 17(01):C01073, 2022.

[24] F Cordella, Wonho Choe, G Claps, L Gabellieri, J Jang, Taemin Jeon, SH Lee, E Li, D Pacella, A Romano, et al. Results and performances of x-ray imaging gem cameras on ftu (1-d), kstar (2-d) and progresses of future experimental set up on w7-x and east facilities. *Journal of Instrumentation*, 12(10):C10006, 2017.

[25] Y. Hu, E. Li, C. Ma, and C. Mai. Application of a data-driven tomography method for the gas electron multiplier (gem) based x-ray camera on east. *Nuclear Instruments and Methods in Physics Research Section A: Accelerators, Spectrometers, Detectors and Associated Equipment*, 1073:170281, 2025.

[26] M. Angelone, D. Lattanzi, M. Pillon, M. Marinelli, E. Milani, A. Tucciarone, G. Verona-Rinati, S. Popovichev, R.M. Montereali, M.A. Vincenti, and A. Murari. Development of single crystal diamond neutron detectors and test at jet tokamak. *Nuclear Instruments and Methods in Physics Research Section A: Accelerators, Spectrometers, Detectors and Associated Equipment*, 595(3):616–622, 2008.

[27] D. Rigamonti, A. Dal Molin, A. Muraro, M. Rebai, L. Giacomelli, G. Gorini, M. Nocente, E. Perelli Cippo, S. Conroy, G. Ericsson, J. Eriksson, V. Kiptily, Z. Ghani, Ž. Štancar, M. Tardocchi, and JET Contributors. The single crystal diamond-based diagnostic suite of the jet tokamak for 14 mev neutron counting and spectroscopy measurements in dt plasmas. *Nuclear Fusion*, 64(1):016016, nov 2023.

[28] J Bielecki and A. Kurowski. Neutron diagnostics for tokamak plasma: From a plasma diagnostician perspective. *Journal of Fusion Energy*, 38:386–393, aug 2019.

[29] M. Gatu Johnson, L. Giacomelli, A. Hjalmarsson, J. Källne, M. Weiszflog, E. Andersson Sundén, S. Conroy, G. Ericsson, C. Hellesen, E. Ronchi, H. Sjöstrand, G. Gorini, M. Tardocchi, A. Combo, N. Cruz, J. Sousa, and S. Popovichev. The 2.5-mev neutron time-of-flight spectrometer tofor for experiments at jet. *Nuclear Instruments and Methods in Physics Research Section A: Accelerators, Spectrometers, Detectors and Associated Equipment*, 591(2):417–430, 2008.

[30] Jan Källne and Harald Enge. Magnetic proton recoil spectrometer for fusion plasma neutrons. *Nuclear Instruments and Methods in Physics Research Section A: Accelerators, Spectrometers, Detectors and Associated Equipment*, 311(3):595–602, 1992.

[31] A. Zimbal, M. Reginatto, H. Schuhmacher, L. Bertalot, B. Esposito, F. Poli, J.M. Adams, S. Popovichev, V. Kiptily, and A. Murari. Compact ne213 neutron spectrometer with high energy resolution for fusion applications. *Review of Scientific Instruments*, 75(10 II):3553 – 3555, 2004. Cited by: 66.

[32] M Rebai, A Milocco, L Giacomelli, E Perelli Cippo, M Tardocchi, A Fazzi, A Pietropaolo, and G Gorini. Response of a single-crystal diamond detector to fast neutrons. *Journal of Instrumentation*, 8(10):P10007, oct 2013.

[33] J. H. Hubbell, H. A. Gimm, and I. O/verbo/. Pair, triplet, and total atomic cross sections (and mass attenuation coefficients) for 1 mev-100 gev photons in elements z=1 to 100. *Journal of Physical and Chemical Reference Data*, 9(4):1023–1148, 10 1980.

[34] Glenn F Knoll. *Radiation detection and measurement*. John Wiley & Sons, 2010.

[35] Fabio Sauli and A. Sharma. Micro-pattern gaseous detectors. *Annual Review of Nuclear and Particle Science*, 49, 12 1999.

[36] Fabio Sauli. Principles of operation of multiwire proportional and drift chambers. *Geneva, Switzerland*, 1977.

[37] Fabio Sauli. The gas electron multiplier (gem): Operating principles and applications. *Nuclear Instruments and Methods in Physics Research, Section A: Accelerators, Spectrometers, Detectors and Associated Equipment*, 805:2–24, 1 2016.

[38] R. Veenhof et al. Garfield++ – simulation toolkit for gaseous detectors. `https://garfieldpp.web.cern.ch/garfieldpp/`, 2017. Version as of [access date].

[39] Federico Caruggi et al. Performance of a triple gem detector equipped with al-gem foils for x-rays detection. *Nuclear Instruments and Methods in Physics Research Section A: Accelerators, Spectrometers, Detectors and Associated Equipment*, 1047:167855, 2023.

[40] Alessandro Pezzotta, G Corradi, G Croci, Marcello De Matteis, Fabrizio Murtas, Giuseppe Gorini, and Andrea Baschirotto. Gemini: A triple-gem detector readout mixed-signal asic in 180nm cmos. In *2015 IEEE International Symposium on Circuits and Systems (ISCAS)*, pages 1718–1721. IEEE, 2015.

[41] F. Caruggi, A. Celora, S. Cancelli, G. Gorini, G. Grosso, F. Guiotto, A. Muraro, E. Perelli Cippo, M. Petruzzo, O. Putignano, M. Tardocchi, L.S. Giarratana, and G. Croci. Development of a triple-gem detector with strip readout and gemini chip for x rays and neutron imaging. *Journal of Instrumentation*, 19(02):C02015, feb 2024.

[42] Seiichiro Matsumoto, Yoichiro Sato, Mutsukazu Kamo, and Nobuo Setaka. Vapor deposition of diamond particles from methane. *Japanese Journal of Applied Physics*, 21(4A):L183, apr 1982.

[43] Carlo Cazzaniga, E. Sundén, F. Binda, Gabriele Croci, Göran Ericsson, Luca Giacomelli, Giuseppe Gorini, E. Griesmayer, Gonçalo Grosso, G. Kaveney, Massimo Nocente, E.Perelli Cippo, M. Rebai, Duncan Syme, M. Tardocchi, and JET-EFDA Contributors. Single crystal diamond detector measurements of deuterium-deuterium and deuterium-tritium neutrons in joint european torus fusion plasmas. *Review of Scientific Instruments*, 85:043506–043506, 04 2014.

[44] E. Griesmayer and Bernd Dehning. Diamonds for beam instrumentation. *Physics Procedia*, 37:1997–2004, 12 2012.

[45] A.V. Alevra and D.J. Thomas. Neutron spectrometry in mixed fields: Multisphere spectrometers. *Radiation protection dosimetry*, 107:37–72, 02 2003.

[46] M. Tardocchi, G. Gorini, H. Henriksson, and J. Källne. Ion temperature and plasma rotation profile effects in the neutron emission spectrum. *Review of Scientific Instruments*, 75(3):661–668, 03 2004.

[47] A Celora, F Guiotto, F Caruggi, G Croci, G Gorini, G Grosso, Z Hu, E Lazzaro, G Marcer, M Nocente, et al. A multipurpose numerical method for imaging studies and tomographic reconstruction. *Journal of Instrumentation*, 19(03):C03032, 2024.

[48] Federico Guiotto, Agostino Celora, Gabriele Croci, Oscar Putignano, Federico Caruggi, Andrea Dal Molin, Giovanni Grosso, Paolo Franz, Matteo Zuin, Massimo Nocente, et al. Revolt-upgrade: a software tool for fast, energy-resolved simulations of soft x-ray detectors in nuclear fusion experiments. *Measurement Science and Technology*, 2025.

[49] Geant4 simulation toolkit. `https://geant4.web.cern.ch/`. Accessed: 3 September 2024.

[50] T. Goorley, M. James, Thomas Booth, F. Brown, J. Bull, Lawrence Cox, J. Durkee, J. Elson, Michael Fensin, R. Forster, J. Hendricks, H. Hughes, Russell Johns, B. Kiedrowski, Roger Martz, S. Mashnik, Gregg Mckinney, D. Pelowitz, R. Prael, and T. Zukaitis. Initial mcnp6 release overview. mcnp6 version 0.1. *Nuclear technology*, 180:298–315, 12 2012.

[51] A Jardin, D Mazon, Martin O'Mullane, J Mlynar, V Loffelmann, M Imrisek, M Chernyshova, T Czarski, G Kasprowicz, A Wojenski, et al. Tomographic capabilities of the new gem based sxr diagnostic of west. *Journal of Instrumentation*, 11(07):C07006, 2016.

[52] Huoxiang Qu, Liqun Hu, F Cordella, G Claps, D Pacella, Liqin Xu, and Erzhong Li. Application of the tikhonov tomography method for the gas electron multiplier (gem) system on experimental advanced superconducting tokamak. *Review of Scientific Instruments*, 90(9), 2019.

[53] L.L. Lao, H. St. John, R.D. Stambaugh, A.G. Kellman, and W. Pfeiffer. Reconstruction of current profile parameters and plasma shapes in tokamaks. *Nuclear Fusion*, 25(11):1611, nov 1985.

[54] Satoshi Ohdachi. Tangential sx imaging for visualization of fluctuations in toroidal plasmas. *Plasma and Fusion Research*, 2:S1016–S1016, 2007.

[55] Andrey Nikolayevich Tikhonov. Solutions of ill posed problems. 1977.

[56] A. Wingen, M.W. Shafer, E.A. Unterberg, J.C. Hill, and D.L. Hillis. Regularization of soft-x-ray imaging in the diii-d tokamak. *Journal of Computational Physics*, 289:83–95, 2015.

[57] Matt Newville and collaborators. Xraydb: X-ray reference data in sqlite; python interface. `https://github.com/xraypy/XrayDB`, 2025. version 4.5.8.

[58] I.B. Smirnov. Modeling of ionization produced by fast charged particles in gases. *Nuclear Instruments and Methods in Physics Research Section A: Accelerators, Spectrometers, Detectors and Associated Equipment*, 554(1):474–493, 2005.

[59] A. Amoroso, R. Baldini Ferroli, I. Balossino, M. Bertani, D. Bettoni, F. Bianchi, A. Bortone, A. Calcaterra, S. Cerioni, W. Cheng, G. Cibinetto, A. Cotta Ramusino, G. Cotto, F. Cossio, M. Da Rocha Rolo, F. De Mori, M. Destefanis, J. Dong, F. Evangelisti, R. Farinelli, L. Fava, G. Felici, I. Garzia, M. Gatta, G. Giraudo, S. Gramigna, M. Greco, L. Lavezzi, M. Maggiora, R. Malaguti, A. Mangoni, S. Marcello, M. Melchiorri, G. Mezzadri, E. Pace, S. Pacetti, P. Patteri, J. Pellegrino, A. Rivetti, M. Scodeggio, S. Sosio, and S. Spataro. Parsifal: A toolkit for triple-gem parametrized simulation. *Computer Physics Communications*, 295:109000, 2024.

[60] P. Raj, J. L. Ball, J. Carmichael, J. A. Frenje, R. Gocht, G. Gorini, I. Holmes, M. Gatu Johnson, R. Kennedy, S. Mackie, M. Nocente, E. Panontin, M. Petruzzo, M. Rebai, M. Reinke, J. Rice, D. Rigamonti, M. Dalla Rosa, A. A. Saltos, M. Tardocchi, R. A. Tinguely, and X. Wang. Overview of the neutron diagnostic systems for the sparc tokamak. *Review of Scientific Instruments*, 95(10):103507, 10 2024.

[61] M. Tardocchi, M. Rebai, D. Rigamonti, R. A. Tinguely, F. Caruggi, G. Croci, A. Dal Molin, Z. Ghani, L. Giacomelli, M. Girolami, G. Grosso, M. Kushoro, G. Marcer, M. Mastellone, A. Muraro, M. Nocente, E. Perelli Cippo, M. Petruzzo, O. Putignano, J. Scionti, V. Serpente, D. M. Trucchi, S. Mackie, A. A. Saltos, E. De Marchi, M. Parisi, A. Trotta, E. de la Luna, J. Garcia, Y. Kazakov, M. Maslov, Z. Stancar, G. Gorini, and JET contributors. A high-resolution neutron spectroscopic camera for the sparc tokamak based on the jet european torus deuterium-tritium experience. *Review of Scientific Instruments*, 93(11):113512, 11 2022.

[62] J. L. Ball, E. Panontin, S. Mackie, R. A. Tinguely, and P. Raj. Evaluating deuterated-xylene for use as a fusion neutron spectrometer. *Review of Scientific Instruments*, 95(12):123514, 12 2024.

[63] J. Havl and Jakub Urban. A magnetic equilibrium reconstruction in tokamak. 01 2007.

[64] H.-S. Bosch and G.M. Hale. Improved formulas for fusion cross-sections and thermal reactivities. *Nuclear Fusion*, 32(4):611, apr 1992.

[65] M. Petruzzo, A. Celora, G. Croci, E. Gallo, G. Gorini, G. Grosso, M. Nocente, M. Parisi, O. Putignano, P. Raj, D. Rigamonti, M. Rebai, M. Reinke, F. Scioscioli, M. Tardocchi, and L. Tedoldi. Design studies on electronics and data acquisition of a real time diamond spectrometer for the sparc neutron camera. *Review of Scientific Instruments*, 95(11):113505, 11 2024.

[66] A Pietropaolo, F Andreoli, M Angelone, U Besi Vetrella, S Fiore, S Loreti, G Pagano, R Pilotti, and M Pillon. The frascati neutron generator: A multipurpose facility for

physics and engineering. In *Journal of Physics: Conference Series*, volume 1021, page 012004. IOP Publishing, 2018.

[67] Agostino Celora et al. Assessment of a space and energy resolved diagnostic based on gem technology on mast-u. *Measurement Science and Technology*, 2024.

[68] VF Shevchenko, YF Baranov, T Bigelow, JB Caughman, S Diem, C Dukes, P Finburg, J Hawes, C Gurl, J Griffiths, et al. Long pulse ebw start-up experiments in mast. 87:02007, 2015.

[69] G. Corradi, F. Murtas, and D. Tagnani. A novel high-voltage system for a triple gem detector. *Nuclear Instruments and Methods in Physics Research Section A: Accelerators, Spectrometers, Detectors and Associated Equipment*, 572(1):96–97, 2007. Frontier Detectors for Frontier Physics.

[70] Naoki Mizuguchi, Takaya Hayashi, and Tetsuya Sato. Dynamics of spherical tokamak plasma on the internal reconnection event. *Physics of Plasmas*, 7(3):940–949, 2000.

[71] A. Weller, A. D. Cheetham, A. W. Edwards, R. D. Gill, A. Gondhalekar, R. S. Granetz, J. Snipes, and J. A. Wesson. Persistent density perturbations at rational-q surfaces following pellet injection in the joint european torus. *Phys. Rev. Lett.*, 59:2303–2306, Nov 1987.

[72] G Turri, RJ Buttery, SC Cowley, CG Gimblett, RJ Hastie, and I Lehane. Magnetic reconnections in mast. In *31st EPS Conference on Plasma Phys. London*, volume 28, 2004.

[73] IT Chapman. Controlling sawtooth oscillations in tokamak plasmas. *Plasma Physics and Controlled Fusion*, 53(1):013001, 2010.

[74] P Helander, L-G Eriksson, RJ Akers, C Byrom, CG Gimblett, and MR Tournianski. Ion acceleration during reconnection in mast. *Physical review letters*, 89(23):235002, 2002.

[75] P Ollus, S Allan, J R Harrison, A R Jackson, T Kurki-Suonio, K G McClements, C A Michael, D Moulton, B S Patel, M Robson, A Snicker, J Varje, C Vincent, and the MAST-U Team. Validating the simulation of beam-ion charge exchange in mast upgrade. *Plasma Physics and Controlled Fusion*, 66(2):025009, dec 2023.

[76] Erzhong Li, Hailin Zhao, X Feng, Chen Fei, T Shi, Y Zhang, and A Liu. Investigation of electron dynamics prior to plasma thermal quench by a gas electron multiplier (gem) camera. *Plasma Physics and Controlled Fusion*, 67, 04 2025.

[77] B Esposito, D Marocco, R Villari, F Murtas, and R Rodionov. Characterization of a gem-based fast neutron detector. *Nuclear Instruments and Methods in Physics Research Section A: Accelerators, Spectrometers, Detectors and Associated Equipment*, 741:196–204, 2014.

[78] C Vincent, S Allan, G Naylor, R Stephen, S Bray, A Thornton, and A Kirk. Fission chamber data acquisition system for neutron flux measurements on the mega-amp spherical tokamak upgrade. *Review of Scientific Instruments*, 93(9), 2022.

[79] A. Celora, F. Guiotto, F. Caruggi, S. Cancelli, G. Claps, F. Cordella, V. de Leo, L. Garzotti, G. Grosso, E. Lazzaro, D. Pacella, O. Putignano, E. Rose, R. Sarwar, R. Scannell, M. Tardocchi, G. Croci, A. Muraro, and the MAST-U. team. Analysis of neutron related background of the sxr gem diagnostic on mast-u. *Journal of Instrumentation*, 20(05):C05010, may 2025.

[80] A. Jardin, J. Bielecki, W. Dąbrowski, K. Drozdowicz, D. Dworak, V. Gerenton, D. Guibert, R. Kantor, K. Król, A. Kulińska, A. Kurowski, B. Łach, D. Mazon, Y. Savoye-Peysson, M. Scholz, J. Walkowiak, U. Wiącek, U. Woźnicka, and WEST team. Energy-resolved x-ray and neutron diagnostics in tokamaks: Prospect for plasma parameters determination. *Physics of Plasmas*, 31(8):082514, 08 2024.

[81] D Mazon, A Jardin, C Coston, F Faisse, M Chernyshova, T Czarski, G Kasprowicz, and A Wojenski. Gem detectors for west and potential application for heavy impurity transport studies. *Journal of Instrumentation*, 11(08):C08006, 2016.

[82] F. Guiotto, O. Putignano, A. Dal Molin, G. Croci, P. Franz, M. Zuin, L. Orlandi, A. Celora, F. Caruggi, G. Grosso, E. Perelli Cippo, M. Tardocchi, P. Bettini, and A. Muraro. Development of a gem based diagnostic for soft x-ray measurements resolved in space, time, and energy at rfx-mod2. *Plasma Physics and Controlled Fusion (PPCF)*, 2026. To be published.

[83] Amptek Inc. Mini-x2 x-ray tube. `https://www.amptek.com/internal-products/obsolete-products/mini-x2-x-ray-tube`, n.d. Accessed: 15 Dec 2025.